Stony Brook University

A Study of Higher-Order Mode Damping in the Superconducting Energy Recovery LINAC at Brookhaven National Laboratory

A Dissertation Presented

by

Lee Reginald Hammons III

to

The Graduate School

in Partial Fulfillment of the Requirements

for the Degree of

Doctor of Philosophy

in

Physics

Stony Brook University

December 2011

Stony Brook University
The Graduate School

Lee Hammons

We, the dissertation committee for the above candidate for the
Doctor of Philosophy degree, hereby recommend
acceptance of this dissertation.

Dr. Vladimir Litvinenko (Advisor)

Senior Phyisicist, Deputy Head, Accelerator R & D Division / Head, eRHIC Group,
Brookhaven National Laboratory
Brookhaven Professor / Co-Director, Center for Accelerator Science and Education,
State University of New York at Stony Brook

Dr. Peter Stephens - Chairperson of Defense

Professor,
State University of New York at Stony Brook

Dr. Thomas K. Hemmick

Co-Director, Center for Accelerator Science and Education / Distinguished Teaching Professor,
State University of New York at Stony Brook

Dr. George F. Sterman

Distinguished Professor,
State University of New York at Stony Brook

Mr. James Rose

NSLS-II RF Group Leader, Accelerator Systems Division,
Brookhaven National Laboratory

This dissertation is accepted by the Graduate School

Lawrence Martin

Dean of the Graduate School

Abstract of the Dissertation

A Study of Higher-Order Mode Damping in the Superconducting Energy Recovery LINAC at Brookhaven National Laboratory

by

Lee Reginald Hammons III

Doctor of Philosophy

in

Physics

Stony Brook University

2011

An energy recovery LINAC (ERL) is being constructed at Brookhaven National Laboratory that will involve a superconducting LINAC along with a superconducting electron gun, all operating at 703.75 MHz. The ERL will serve as a testbed for the concepts and technologies required to implement future upgrades in the Relativistic Heavy Ion Collider (RHIC). Because of the high current and high charge requirements of the ERL, effective higher-order mode (HOM) damping is an essential component of the ERL research and development program. This thesis focuses on three areas of HOM characterization and damping development: damping of HOMs in the five-cell LINAC, use of the electron gun fundamental power couplers (FPCs) to damp HOMs, and the development of a ceramic/ferrite damper for the electron gun.

The five-cell LINAC uses an HOM load lined with ferrite and attached to the beampipe on either side of the cavity. These studies characterized the frequency-dependent nature of the ferrite absorbing material and derived a set of "portable" ferrite parameters that simplified simula-

tion work. Using these “portable” parameters, it was determined that the ferrite absorber is effective in damping the HOMs of the five-cell cavity over a range of frequencies.

In addition, higher-order mode damping in the electron gun was studied using the fundamental power couplers. The gun cavity is a superconducting half-cell structure designed to accelerate electrons to an energy of 2.5 MeV and features dual fundamental power couplers. The HOMs of the gun cavity were studied along with the damping capabilities of the FPCs. Simulation studies determined that the FPCs couple strongly to many of the HOMs studied. However, the transition between the coaxial FPCs and the waveguide that feeds power to the FPCs is a "doorknob" type transition, and it was found that this component shows the best transmission qualities between 1 and 2 GHz, thus limiting the damping capabilities of the FPCs to this bandwidth. It remains to be seen how the FPCs will perform under actual conditions.

Finally, the development of a ceramic/ferrite damper was described for the electron gun. The damper features a lossless alumina ceramic break surrounded by a ferrite load and was designed to isolate the vacuum chamber from the ferrite tiles. Various studies were conducted using simulation and prototype designs, and it was determined that the ceramic/ferrite load can be effective in damping higher-order modes of the gun cavity. Analytical calculations along with simulation show that the ceramic tends to alter the field distribution of higher-order modes and change the damping qualities depending on the frequency. The effectiveness of the damping for a given mode depends on a variety of factors including the thickness of the ceramic, the spacing between the ceramic and ferrite layers, and the diameter of the inner ceramic surface.

To my family, my friends, and my co-workers.

Thank you for all of your support.

Table of Contents

List of Figures

List of Tables

Chapter 1

Introduction and Background

1.1. Introduction

This thesis addresses work done to understand the higher-order mode spectra of the superconducting RF cavities used in the energy recovery LINAC being constructed at Brookhaven National Laboratory (BNL) as well as the design of structures for higher-order mode (HOM) damping. In particular, this study has addressed three specific topics: the higher order modes found in the five-cell electron LINAC that is used in the Energy Recovery LINAC, the design of a ferrite HOM damper surrounding a ceramic break for use with the electron gun cavity used as the injector for the ERL, and the use of the fundamental power couplers (FPCs) as HOM dampers for the electron gun.

The development of the ERL is the first step on road toward the development of several upgrades in the Relativistic Heavy Ion Collider (RHIC), including the development of an electron-ion collider (eRHIC) [1] as well-planned experiments in coherent electron cooling [2]. The physics and technical requirements of these programs all involve electron ERLs. To this end the Brookhaven ERL is being developed to provide a testbed facility for the technologies and accelerating structures necessary to implement these projects. HOM damping is crucial to these projects because of the high-current, high-brightness, and high-charge requirements.

In order to understand the physics aims of the RHIC program and the role of the ERL within this program, a brief overview of the RHIC project will be presented. In addition, an overview of the ERL project and its goals will be discussed.

1.2. The Relativistic Heavy Ion Collider

The Relativistic Heavy Ion Collider (RHIC) is a collider located at Brookhaven National Laboratory designed to study quantum chromodynamics (QCD) using beams of heavy nuclei at ultrarelativistic energies as high as 100 GeV per nucleon for heavy ions and 250 GeV for protons. The results from RHIC have revealed wholly new and unexpected phenomena at the subnuclear level where the quarks and gluons define the relevant degrees of freedom.

The theory of QCD was developed in the 1970's to explain the confinement of quarks in hadrons. The phenomenon of confinement ensures that QCD is well-behaved at large distances, and this aspect of the theory makes QCD unique among the components of the Standard Model in that it is not singular at short distances, and thus, appears to be the only self-consistent non-trivial quantum field theory. One early realization based on the QCD was that at sufficiently large energy density ("temperature"), the forces that confine quarks in nucleons can be overcome by color-screening effects resulting in the transition to a new state of matter called the quark-gluon plasma (QGP). The bulk dynamical properties of this matter are determined by the quarks and gluons in themselves, rather than those of the composite hadrons. Indeed, these are the same temperatures and densities that are believed to have prevailed in the first few microseconds after the Big Bang. The suggestion that this phase transition is a fundamental feature of nature that might occur in the hot, dense nuclear matter created in heavy-ion collisions triggered a series of experiments in the United States and Europe that culminated in the RHIC program.

Early measurements at RHIC identified a new form of thermalized matter formed in gold-gold collisions at energy densities more than 100 times that of cold atomic nuclei. This matter shows surprising properties including unexpectedly short thermalization times (< 1 fm/c), energy density at least 15 times greater than that required for color deconfinement, and enormous collective motion with ideal hydrodynamic properties – a "perfect liquid" with virtually no viscosity, i.e., a near-zero viscosity to entropy ratio – lower than any previously observed fluid and perhaps close to a universal lower bound.

Furthermore, a consensus has emerged that the new matter that has been produced in collisions at RHIC is consistent with models that incorporate quark and gluon degrees of freedom directly rather than ordinary color neutral hadrons, i.e., a strongly coupled quark-gluon plasma

rather than the parton gas that was predicted by perturbative QCD prior to the existence of RHIC data. In addition, the RHIC has found rather low hadron production and suppression of high-transverse-momentum particles in forward scattering, i.e., jet quenching, consistent with gluon saturation in the colliding nuclei playing an important role at RHIC energies.

In RHIC, the process begins with gold nuclei injected into each of two rings that intersect at six interaction points. At present, two of these interaction points are equipped with an array of integrated detectors that form the STAR and PHENIX experiments. These intersection points are where the nuclear collisions take place in the accelerator, and the process of QGP formation nominally begins with an initial, intense heating of the nuclear volume due to the collision of the two nuclear and the formation of a high-temperature system of quarks, antiquarks, and gluons. It is suspected that in this collision event, the gluon density may reach a saturated value, described as a Color Glass Condensate.

As the two nuclei collide, intense color fields of the two nuclei interact to produce a dense, unthermalized state of quarks, anti-quarks, and gluons that that immediately begins to expand and cool. High-energy quarks and gluons are sometimes formed that will produce jets of hadrons that propagate through the dense matter of the collision, and pairs of heavy quarks are formed in this initial stage. These jets are of particular interest because, imprinted in their production is a record of this early stage of the collision and they form hard-colored, internal probes. Most interestingly, the number of hadrons that form these jets with high transverse momenta are found to be suppressed in central Au+Au collisions by a factor of 4-5 relative to the experimental p+p baseline, in contrast to direct photons which escape from the collision without further interaction and whose production rates and spectra agree well with expectations based on perturbative QCD [3]. This phenomenon is referred to as jet quenching, and, while the details of the quenching are not completely quantitatively understood, it would seem that the observed quenching is the result of a slowing down, or quenching, of the most energetic quarks as they propagate through a dense QGP [4]. Indeed, the rate of this energy loss is likely to be enormous, and points to a strongly interacting medium.

As the collision proceeds, the hot, dense matter initially formed quickly thermalizes and reaches equilibrium, expanding and cooling through the very strong collective interactions mentioned above. This medium forms what appears to be an ideal hydrodynamic fluid with zero vis-

cosity. This contrasts strongly with intuitive pre-RHIC expectations that the QGP would exhibit perturbative, gas-like behavior similar to electromagnetic plasmas.

Another important aspect of the RHIC experimental program is to develop a deeper understanding of the spin structure of the proton. This includes the direct measurements of the gluon and flavor-separated quark and antiquark contributions to the proton's spin, and studies of the transverse spin and transverse motion of the quarks and gluons in a transversely polarized proton [3]. The RHIC also provides an important opportunity to use deep inelastic scattering techniques involving an electron-ion collider, and, therefore, an electron-ion collider addition to the RHIC program is currently being pursued called eRHIC. These machines will be briefly described later in this chapter.

The RHIC ring actually consists of two rings each arrayed with superconducting magnets. Each ring is about 2.4 miles long. The main components of the magnet system are 288 arc-size dipoles and 108 insertion dipoles along with 276 arc- and 216 insertion-quadrupoles. In addition to dipoles and quadrupoles there are a variety of smaller magnets including trim quadrupoles, sextupoles, and corrector magnets. The magnets are cooled to a temperature of < 4.6 K by circulating supercritically-cooled helium supplied by a refrigerator [4].

1.3. Luminosity, Emittance, and Beam Size

Key to understanding the physics of a collider such as RHIC and the beam in a collider is an understanding of the luminosity and the beam size. These concepts constitute important figures of merit for a collider, and, in this section, these concepts are explained to provide the background necessary to fully understand the aims and impact of the ERL program and eRHIC.

1.3.1. Luminosity

The event rate, R, within the collider is proportional to the interaction cross section σ_{int}. The factor of proportionality is called the luminosity, $\mathcal{L}$, such that

$$R = \mathcal{L}\,\sigma_{int}. \tag{1.1}$$

If two bunches containing n_1 and n_2 particles collide with frequency *f*, then the luminosity is approximately

$$\mathcal{L} = f \frac{n_1 n_2}{4\pi\sigma_x\sigma_y}. \quad 1.2$$

Where σ_x and σ_y characterize the Gaussian transverse beam profiles in the horizontal and vertical dimensions. Though the distribution of beam particles may start out far from Gaussian, by the time the beam reaches high energy, Gaussian distribution is a good approximation due to the central limit theorem of probability and the diminished impact of space charge [5].

Luminosity is often expressed in units of $cm^{-2}s^{-1}$. While the number of particles and the beam profiles may change over the course of time, the luminosity for a collider is generally expressed as an integrated luminosity achieved over some period of time. Integrated luminosity is usually quoted as the inverse of the standard measures of cross section such as femtobarns.

1.3.2. Emittance and Beam Size

The beam size can be expressed in terms of two quantities: the transverse emittance, ϵ, and the lattice function, β. The transverse emittance is the area in a phase space occupied by the distribution of particles associated with either of the two transverse degrees of freedom, *x* and *y*. These coordinates are the position of a given particle with respect to some ideal design trajectory. The conjugate coordinates are the transverse momenta, which at constant energy are proportional to the angles of particle motion with respect to the design trajectory, *x'* and *y'*. Then, the beam size in the *x*-coordinate is given by:

$$\sigma_x = \sqrt{\epsilon_x\beta_x} \quad 1.3$$

Similarly, in the *y*-coordinate:

$$\sigma_y = \sqrt{\epsilon_y\beta_y}. \quad 1.4$$

To achieve high luminosity, the key is to make high population bunches of low emittance to collide at high frequency at locations where the beam optics provide as low values of the lattice function as possible.

1.4. Overview and Aims of the ERL Project

The physics needs and technical requirements for several future accelerator projects at the RHIC all involve electron ERLs. These include the development of an experimental 703 MHz ERL [6]; the study of superconducting cavities of a polarized electron-ion collider (eRHIC) [1]; and steps toward planned experiments in coherent electron cooling [2]. Understanding of the higher-order modes of the radio-frequency RF cavities of these accelerators and development of effective HOM absorbers are crucial to the development of these projects because of the high-current, high-brightness, and high-charge requirements.

Towards these ends, a research and development ERL facility is being constructed at BNL. This facility aims to demonstrate operation with an average beam current in the range of 500 mA, combined with very-high-efficiency energy recovery. The ERL R&D program also provides for the exploration of a future electron-hadron/heavy-ion collider, eRHIC. The design of the eRHIC involves the construction of a 30 GeV electron accelerator in a local area inside and near the RHIC tunnel. Electrons will be produced by a polarized electron source and accelerated in energy recovery LINACs. Collisions of the electron beam with 100 GeV/u heavy ions or with 250 GeV polarized protons will be arranged in one of the existing interaction regions of RHIC.

The ERL facility is comprised of a five-cell superconducting LINAC, plus a ½-cell superconducting, photoinjector RF electron gun, both operating at 703.75 MHz [7]. The ERL facility will address expanding the capabilities of ERLs and feature a highly flexible lattice covering a vast operational parameter space. The facility is designed to serve as a test bed for the technologies and concepts necessary for future projects including the eRHIC. Two basic modes of operation are envisioned for the facility: a high-current mode with an average current of 0.5 A, and a high-bunch-charge mode with an average beam current of 0.05 A. Key parameters for the project are shown in Table 1.1. At present, the superconducting five-cell cavity string has been installed, and several cooldowns to test five-cell cavity operation have been performed.

Table 1.1 - ERL Parameters

Parameter	High Current	High Charge
Gun energy [MeV]	2.5	3.0
ERL energy (1-2 passes) [MeV]	20-40	20-40
Avg. beam current [A]	1	0.1
Charge/bunch [nC]	0.7	5
Norm. emittance [mm mrad]	1.4	4.8-5.3
Bunch length [cm]	1.0	3.0

The eRHIC program will employ multiple five-cell superconducting cavities of the type being developed for the ERL facility to accelerate electrons to 30 GeV for collision with 250 GeV protons in RHIC. The ERL project would serve as the first stage toward the realization of eRHIC, a future electron-ion collider at BNL with both higher luminosity and energy reach.

The ERL project is currently under construction at the Collider-Accelerator Department at BNL and is based on a high-current (0.5 A) superconducting 2.5 MeV RF electron gun as well as a single-mode superconducting 5-cell RF LINAC along with a return loop of approximately 20 meters with a very flexible lattice. The project is aimed at addressing many outstanding questions relevant for high-current, high-brightness operation in energy-recovery LINACs. As such, the project will serve as a testbed for future RHIC projects.

This document will describe the work done to characterize the higher-order modes in the RF cavities of the ERL including the electron gun and the five-cell LINAC cavity as well as the development of higher-order mode absorbers for these cavities. We shall begin by explaining the basic operating principles of the energy recovery LINAC as well as higher-order modes along with the relevant parameters that describe the interaction of these modes with particle beams in accelerators.

1.5. The Energy Recovery LINAC

The first references to “energy recovery” appear to be attributable to M. Tigner who, in 1965, explored the possibility of using an energy-recovery LINAC as a means of performing “clash-

ing" beam-on-beam particle physics experiments [8]. The basic idea behind energy recovery is a simple one: energy that it used to accelerate electrons on one pass can be recovered on a subsequent pass of the accelerated electrons within an RF cavity and used to accelerate another group of electrons. The beam-currents that can be accelerated in such an arrangement can be similar to that of a storage ring but can also achieve the superior beam quality that often characterizes traditional LINACs. Thus, the advantage of an energy-recovery LINAC is that it provides both high current and high beam quality that can be employed in a variety of settings such as free-electron lasers, electron cooling devices, or, as in the case of the Brookhaven application, a high-energy electron-ion collider.

To understand how such a device functions, it is useful to consider the historical context of the development of such devices. In general, two basic types of accelerators are used in high-energy and particle physics research. The first type is the linear accelerator or LINAC type. Here there may be single-pass or recirculating-type LINACs. One of the best examples of the single-pass type is the Stanford Linear Accelerator Center (SLAC). In a linear accelerator, the beam has a specific beginning in the injector and a specific end in the beam dump. The beam propagates along straight line from the injector to the beam dump. The beam is accelerated as it advances through the accelerator in RF cavities that impart energy to the electrons through electromagnetic interaction of the form $\mathbf{E} \cdot \mathbf{v}$, the electromagnetic field in the cavity being chosen so that the electric field in the cavity, $\mathbf{E}$, is substantially collinear with and along the electron velocity vector $\mathbf{v}$ as the electon moves through the cavity [9].

Principal features of such a device are that the electron resides only for very short periods in the accelerator relative to the radiation driving emittance growth processes; furthermore, the beam current can be easily controlled by the nature of the injector. Also, the beam quality, particularly, the emittance, is primarily determined by the injector. Finally, the emittance can be manipulated using an array of well-known, standard RF and electron-beam optical techniques. The linear geometry simplifies many aspects of the layout and operation of such machines.

The second class of machines is of the synchrotron-type storage ring. In basic terms, the energy in a storage ring is supplied to the beam through RF cavities which subtend a small portion of the ring. The electrons trajectories are bent along the equilibrium orbit of the device, usually a roughly circular orbit that electrons will traverse many times. After the electrons are

injected into the machine, the particles rapidly settle into an equilibrium state where synchrotron losses may be copious depending on the energy due to the transverse acceleration of the circular orbit. Because of this radiative loss, it is necessary to continually resupply the electrons with energy. As the electrons reach their equilibrium state, the electrons become naturally bunched and move toward the stable-phase point of the accelerating gradient, and, as mentioned, the stable equilibrium orbit about the accelerator. The lifetime of such a beam inside the accelerator is determined by a variety of beam interactions including energy losses associated with radiative effects such as synchrotron radiation and quantum excitations as well as intrabeam or Touschek scattering. These effects tend to degrade the beam quality in such machines and a variety of techniques have been developed to combat this degradation. On the other hand, the currents that can be achieved are quite high, and lifetimes for many hours can be achieved inside the storage ring.

In an energy recovery machine, the energy that is expended in accelerating a beam of particles is recovered at the end of the process and recycled into the acceleration of new beam particles. The particles from which the energy is recovered are then steered into a dump. This energy recovery is accomplished in the RF cavities – by properly choosing the arrival time of the beam particles, the same cavities are used both to accelerate and decelerate the beam. In the simplest recycling scheme, a beam of electrons is injected into the LINAC and timed to accelerate through the LINAC on the first pass. The recirculation path is then chosen to be precisely an integer plus ½ of the RF wavelength. Thus, on the second pass through the LINAC, the beam is actually decelerated since the phase of the RF is exactly 180° out of phase from the accelerating field that first propelled the beam particles. Thereby, energy is transferred directly via the RF field from the decelerating beam to the accelerating beam.

Key to this process is that these RF power systems do not need to provide the energy to accelerate the first-pass beam. The draw on RF power may be almost completely independent of the beam current via this process. Furthermore, the beam-dump design is much simpler because the beam is being dumped at much lower energy, and may, under certain conditions, reduce the activation of the dump [9].

The efficiency of the process can be characterized by the "RF to beam multiplication factor" [9], defined as $\kappa \equiv P_{beam}/P_{RF}$, the ratio of the beam power at the point of use to the

power supplied to the RF cavities accelerating the beam. For an electron beam of average current I_b injected into an ERL at injection energy E_{inj} and accelerated to a final energy E_f in the limit of perfect energy recovery, the multiplication factor is equal to

$$\kappa = \frac{P_{beam}}{P_{RF}} \cong \frac{I_b E_f}{I_b E_{inj} + P_{rf,linac}}, \quad 1.5$$

where the required RF power consists of two terms: $I_b E_{inj}$, the power required to accelerate the beam current I_b in the injector, which is not energy recovered, and $P_{rf,linac}$, the RF power required to establish the electromagnetic fields in the ERL cavities, which is no longer dependent on the beam current because the positive and negative current are balanced in the ERL. Note that the multiplication factor increases with average beam current, and asymptotically approaches a value that is equal to the ratio of final to injected beam energy, E_f/E_{inj}. The higher the beam current, the higher is the overall system efficiency.

The concept of the multiplication factor is useful in that it can be applied to both normal and superconducting cavities and distinguishes the different cavity types from each other. The multiplication factor for both types can be very large and the recovery factors for both types of systems can be very similar. Ultimately, the superconducting cavity gains in that the wall losses in the superconducting cavity are very small relative to the normal conducting cavity. In normal conducting system, the losses to the wall of the cavity are the main load on the system. Indeed, for superconducting structures, the $P_{rf,linac}$ term is about 1000 times better for superconducting cavities than for normal-conducting cavity, and this is reflected directly in the overall multiplication factors of the best ERLs: the best normal-conducting systems have multiplication factors of order 0.1 or less, whereas superconducting ERL proposals ten to reach several hundred.

1.6. Applications of ERLs at Brookhaven National Laboratory

ERLs have been useful in a variety of applications and are envisioned to play a central role at Brookhaven for use in the eRHIC program. The eRHIC program shall consist of a high-current, high-charge electron beam (also highly polarized) colliding with a hadron beam. Here, the use

of an energy recovery LINAC is a distinct advantage because the electron beam is discarded following energy recovery, significantly decreasing the disruption of the electron beam quality due to the collision with the hadron beam and increasing the potential luminosity of the collisions. This, in turn, makes such a collider an highly potent tool for answering some of the basic open questions that currently lie at the heart of nuclear physics [10]:

- What is the structure of the proton and neutron in terms of their quark and gluon constituents?
- How do quarks and gluons evolve into hadrons?
- What is the quark-gluon origin of nuclear binding?
- How do the quarks and gluons manifest themselves in the properties of atomic nuclei?

A key challenge in the implementation of the eRHIC program is the delivery of a high-charge, high-current electron beam. The ERL program is specifically intended to study these challenges and devise methods and devices to overcome them. For the purposes of this study, it is important to note that the acceleration of high-charge and high-average-current beams in SRF structures such as those to be employed in the ERL is closely related to the problems associated with higher-order modes. Dipole type HOMs lead to multi-bunch, multi-pass beam breakup (BBU) instabilities in ERLs. Furthermore, the large power generated by the HOMs must be safely removed from the cavities. Good damping of all modes is essential both for a high-current threshold of the BBU instability and for the operation of the cryogenic SRF cavities. Therefore, it is imperative to the success of the project that good SRF designs that minimize the evolution of higher-order modes be used and that effective higher-order mode dampers are in place in the ERL.

Chapter 2

Higher-Order Modes in Cavities and Implications for Beam Dynamics

2.1. Introduction

Radio frequency superconducting cavities are an important feature of many future accelerator projects around the world. Such cavities have been used for many years in various projects for low- and medium-energy nuclear physics research as well as high-energy physics research projects at a variety of laboratories and universities [11]. Among the many kinds of projects that depend on superconducting RF structures are energy recovery LINACs, X-FELs, electron coolers, and electron-ion colliders with high average current and brightness with ultra short bunches. One of the major challenges for these projects is the need to accelerate high-current beams. Such beams dissipate large amounts of energy, making CW operation prohibitive.

At Brookhaven National Laboratory, several future accelerator projects are being developed for the Relativistic Heavy Ion Collider as described in Chapter 1. In this paper, we will focus on the nature of higher order modes in the electron gun and the five-cell cavity of the ERL project. Because these are superconducting cavities, understanding the nature of these modes is of critical importance. The presence of HOMs in these structure can have a profound and far-reaching impact on power dissipation and beam stability, degrading the quality of beam in the ERL or disrupting the beam altogether in the worst cases. The power of a given HOM mode is given by

$$P_{HOM} = kQ_bI \qquad 2.1$$

where k is the loss factor, Q_b is the charge per bunch, and I is the beam current. The beam itself has the potential to excite these modes, and, if the modes have sufficiently high Q-values, they may interact with subsequent electrons that pass through the cavity imparting various forces on the beam. Therefore, it is important to characterize these modes properly and, if necessary, mitigate their impact. Characterization generally includes determining the mode configuration (monopole, dipole, etc.), the Q-value, and both the geometrical (R/Q) and total shunt impedance of the modes. Mitigation means reducing either the Q-factor of the mode (damping) or the shunt impedance or both, therefore reducing the total shunt impedance to level such that the potential for the beam to excite these modes is minimized. These various quantities will be discussed in more detail below, and this chapter shall provide the background ideas necessary for understanding the work that follows.

2.2. Modes and Fields in Resonant Cavities

In this section, fundamental concepts of fields in cavities are outlined in order to gain an understanding of how higher-order modes arise and how they are to be understood. In this manner, we gain an understanding of the formalism for characterizing these fields and begin to understand the field configurations of these modes.

2.2.1. Formalism of TM and TE Modes

A resonant RF cavity such as that used for accelerating charged particles can be understood as a waveguide that has closed boundaries. All of the considerations for such a waveguide apply with small exceptions because of the addition of beamholes or ports to one or more sides of the structure. Consider a cylinder whose longitudinal axis is the z-axis. We shall assume that the walls of the structure are perfectly conducting and consider the electromagnetic fields in the vicinity of the wall. According to Maxwell's equations, because of the perfect conductor, both **E** and **H** vanish at the surface, however the presence of the surface charges and currents allows for the existence of a normal component of **E** as well as a tangential component of **H**, but the tangential component of **E** and the normal component of **B** must be continuous across the surface. Then,

$$\hat{n} \times \mathbf{E} = 0, \qquad \hat{n} \cdot \mathbf{H} = 0 \tag{2.2}$$

where $\hat{n}$ is the unit vector normal to the surface of the conductor. The fields propagating inside the waveguide take the form:

$$\begin{aligned} \mathbf{E}(\mathbf{x}, t) &= \mathbf{E}(\rho, \phi) e^{i(kz - \omega t)} \\ \mathbf{H}(\mathbf{x}, t) &= \mathbf{H}(\rho, \phi) e^{i(kz - \omega t)} \end{aligned} \tag{2.3}$$

where k is the wavenumber and ω is the angular frequency. In this form, then, Maxwell's equations combine to give the wave equation:

$$\left(\nabla^2 - \frac{1}{c^2} \frac{\partial^2}{\partial t^2} \right) \begin{Bmatrix} \mathbf{E} \\ \mathbf{H} \end{Bmatrix} = 0 \tag{2.4}$$

This then forms a compact set of equations that is usually separated into field components parallel to and transverse to the z axis. We may then solve for the **E** and **H** fields by solving the eigenvalue equation 2.4 subject to the boundary values given in 2.2 using the expressions given in 2.3. We find that the solutions form an orthogonal set with eigenvalues $\gamma^2 = \omega^2/c^2 - k^2$.

In a waveguide, there occur two basic types of field configuration whose existence can be seen from considering 2.4 satisfied by the longitudinal components, E_z and B_z as well as the boundary condition 2.2. Given our considerations of the boundary, it becomes clear that, at the surface,

$$E_z|_S = 0 \tag{2.5}$$

Furthermore, it can be inferred that

$$\left. \frac{\partial B_z}{\partial n} \right|_S = 0 \tag{2.6}$$

where $\partial/\partial n$ is the normal derivative at a point on the surface. For a given frequency ω, only certain values of wave number k can occur, typical of a waveguide. Conversely, for a given value of k, only certain values of ω values may occur. This is the situation typical of a resonant cavity. The key feature of these phenomena, as Jackson observes, is that "since the boundary conditions on E_z and B_z are different, the eigenvalues of the two fields will, in general, be different, and thus, the fields divide naturally into two types: transverse magnetic (TM) waves where

$B_z = 0$ everywhere and $E_z|_S = 0$ and transverse electric (TE) waves where $E_z = 0$ everywhere and $\partial B_z/\partial n\,|_S = 0$. These waves constitute a complete set of fields to describe any resonant mode within a waveguide or a cavity." [13] For TM modes, a longitudinal component of **E** exists whereas **H** is transverse everywhere with respect to the *z* axis. For TE modes, a longitudinal component of **H** exists and **E** is transverse everywhere. In both cases, the transverse magnetic and electric fields are related by

$$\mathbf{H}_\perp = \pm\frac{\hat{z}\times\mathbf{E}_\perp}{\mathrm{Z}} \tag{2.7}$$

where

$$Z = \frac{k}{\epsilon_0\omega} \tag{2.8}$$

is the wave impedance for TM modes and

$$Z = \frac{\mu_0\omega}{k} \tag{2.9}$$

for TE modes. The positive case applies to waves traveling in the $+\hat{z}$ direction, while the negative case refers to backward traveling waves. The transverse components can be derived from the longitudinal components by

$$\mathbf{E}_\perp = \pm\frac{ik}{\gamma^2}\nabla_\perp E_z \quad \text{(TM modes)} \tag{2.10}$$

$$\mathbf{H}_\perp = \pm\frac{ik}{\gamma^2}\nabla_\perp H_z \quad \text{(TE modes)} \tag{2.11}$$

where E_z and H_z satisfy 2.4.

These are the expressions for waveguides. However, if we wish to apply our expressions to cavities, it is necessary to add conducting surfaces at $z = 0$ and $z = d$. This creates nodes at either end of the structure and standing waves in the cavity are thus formed. Of course, the boundary conditions in 2.1 still apply, and we can combine forward and backward traveling waves to do this explicitly. One finds that

$$E_z(\mathbf{x},t) = \psi(\rho,\phi)\cos\left(\frac{p\pi z}{d}\right)e^{i\omega t},\ \ p = 0,1,2\ldots \quad \text{(TM modes)} \tag{2.12}$$

$$H_z(\mathbf{x},t) = \psi(\rho,\phi)\sin\left(\frac{p\pi z}{d}\right)e^{i\omega t},\ \ p = 0,1,2\ldots \quad \text{(TE modes)} \tag{2.13}$$

with $k = p\pi/d$. When these equations are then substituted into 2.4, then the fields $\psi(\rho,\phi)$ are solutions of the eigenvalues equation

$$\left(\nabla_\perp^2 + \gamma_j^2\right)\psi(\rho,\phi) = 0, \tag{2.14}$$

where

$$\gamma_j^2 = \left(\frac{\omega_j}{c}\right)^2 - \left(\frac{p\pi}{d}\right)^2 \tag{2.15}$$

is the *j*th eigenvalue.

The transverse field components can, once again, be derived by considering equations 2.9 and 2.10 along with 2.11 and 2.12 separately [13]. Then, for TM modes

$$\mathbf{E}_\perp = \ -\frac{p\pi}{d\gamma_j^2}\sin\left(\frac{p\pi z}{d}\right)\nabla_\perp\psi(\rho,\phi) \tag{2.16}$$

$$\mathbf{H}_\perp = \frac{i\omega_j}{\eta c\gamma_j^2}\cos\left(\frac{p\pi z}{d}\right)\hat{z}\times\nabla_\perp\psi(\rho,\phi) \tag{2.17}$$

and for the TE modes

$$\mathbf{E}_\perp = -\frac{i\eta\omega_j}{c\gamma_j^2}\sin\left(\frac{p\pi z}{d}\right)\hat{z}\times\nabla_\perp\psi(\rho,\phi) \tag{2.18}$$

$$\mathbf{H}_\perp = \ \ \frac{p\pi}{d\gamma_j^2}\cos\left(\frac{p\pi z}{d}\right)\nabla_\perp\psi(\rho,\phi) \tag{2.19}$$

where

$$\eta = \sqrt{\frac{\mu_0}{\epsilon_0}} \tag{2.20}$$

is the impedance of free space [11].

2.2.2. The Pillbox Cavity

The pillbox cavity is the prototypical example of a cylindrical resonator in which a circular waveguide is closed by conducting walls at either end. The conditions of 2.2 apply and reflections at the conducting walls at each of the boundaries along the *z*-axis create standing waves that we may write as:

$$\text{TM modes:} \quad E = E_0 \cos\left(\frac{q\pi z}{d}\right) e^{i\omega t}, \quad p = 0, 1, 2 \ldots \tag{2.21}$$

$$\text{TE modes:} \quad B = B_0 \sin\left(\frac{q\pi z}{d}\right) e^{i\omega t}, \quad p = 1, 2, 3 \ldots \tag{2.22}$$

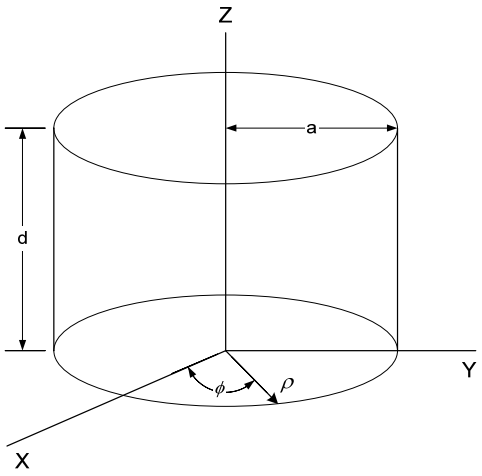

Figure 2.1: Circular pillbox cavity.

The solutions to the eigenvalues equation with cylindrical symmetry are Bessel functions. We can conveniently summarize the solutions via the wavefunctions [14] for the TM and TE modes. For the TM mode,

$$\psi_{mnq}^{TM} = J_n\left(\frac{x_{mn}\rho}{d}\right)\begin{Bmatrix}\sin n\phi \\ \cos n\phi\end{Bmatrix}\cos\left(\frac{q\pi}{d}z\right) \tag{2.23}$$

where $m = 0, 1, 2, \ldots$; $n = 1, 2, 3, \ldots$; and $q = 0, 1, 2, \ldots$ The fields are then given by

$$\begin{aligned} E_\rho &= \frac{1}{j\omega\epsilon}\frac{\partial^2\psi}{\partial\rho\,\partial z} & H_\rho &= \frac{1}{\rho}\frac{\partial\psi}{\partial\phi} \\ E_\phi &= \frac{1}{j\omega\epsilon\rho}\frac{\partial^2\psi}{\partial\phi\,\partial z} & H_\phi &= -\frac{\partial\psi}{\partial\rho} \\ E_z &= \frac{1}{j\omega\epsilon}\left(\frac{\partial^2}{\partial z^2} + k^2\right)\psi & H_z &= 0. \end{aligned} \tag{2.24}$$

For TE modes, the wavefunction is given by

$$\psi_{mnq}^{TM} = J_n\left(\frac{x'_{mn}\rho}{d}\right)\begin{Bmatrix}\sin n\phi\\ \cos n\phi\end{Bmatrix}\sin\left(\frac{q\pi}{d}z\right). \tag{2.25}$$

Then, the fields are given by

$$\begin{aligned} E_\rho &= -\frac{1}{\rho}\frac{\partial\psi}{\partial\phi} & H_\rho &= \frac{1}{j\omega\mu}\frac{\partial^2\psi}{\partial\rho\,\partial z}\\ E_\phi &= \frac{\partial\psi}{\partial\rho} & H_\phi &= \frac{1}{j\omega\mu\rho}\frac{\partial^2\psi}{\partial\phi\,\partial z}\\ E_z &= 0 & H_z &= \frac{1}{j\omega\mu}\left(\frac{\partial^2}{\partial z^2}+k^2\right)\psi \end{aligned} \tag{2.26}$$

These modes are classified as TM_{mnq} or TE_{mnq}, where *mn* and *q* are integers and describe the azimuthal, radial, and longitudinal nodes of each modes. In other words, the indices *m*, *n*, and *q* describe the number of changes of sign in each direction for a given mode. The resonant frequencies of these modes are given by:

$$\text{TM mode:}\quad \omega_{mnq} = \frac{1}{\sqrt{\mu_0\epsilon_0}}\sqrt{\left(\frac{q_{mn}}{r}\right)^2+\left(\frac{q\pi}{d}\right)^2} \tag{2.27}$$

$$\text{TE mode:}\quad \omega_{mnq} = \frac{1}{\sqrt{\mu_0\epsilon_0}}\sqrt{\left(\frac{q'_{mn}}{d}\right)^2+\left(\frac{q\pi}{d}\right)^2} \tag{2.28}$$

where q_{mn} and q'_{mn} are the *n*th zero of the Bessel function and its derivative, and *r* is the radius the cavity.

Particles in a cavity normally require an electric field along the axis of the cavity in order to accelerate. The TM modes have a longitudinal field along the z-axis, and the lowest accelerating mode of the type TM_{010} has the form:

$$E_z = E_0 J_0\left(\frac{\omega_{010}r}{c}\right)\cos(\omega_0 t) \tag{2.29}$$

$$H_\phi = -\frac{1}{\mu_0 c}E_0 J_0\left(\frac{\omega_{010}r}{c}\right)\sin(\omega_0 t) \tag{2.30}$$

where

$$\omega_{010} = \frac{2.405c}{R} \tag{2.31}$$

and R is the radius of the cavity. Note that this frequency is independent of the cavity length. Such modes are called *monopole* modes because of the field distribution. Monopole modes are the basic accelerating modes of a cavity since they have an electric field on the axis of the cavity. Modes of the type TM_{1nq} have a net deflecting field on axis and are called *dipole* modes, and they can be problematic in a cavity because they can disrupt beams through their application of transverse forces on a beam.

Because a cavity is not a pure pillbox, but rather has beamholes in order to allow the passage of beam through the cavity, the eigenmodes of such a structure are perturbed, and the field distributions are somewhat different than the case of a pure pillbox cavity. For such cases, computer codes are often used to calculate the modes such as CST Microwave Studio [15] and others.

2.2.3. Accelerating Voltage in Cavities

An important feature to understand in RF cavities is the voltage in the cavity. This voltage provides the energy that accelerates particles in the cavity and will be the basis of concepts that are important to understanding higher-order modes in cavities.

We shall assume a relativistic electron with velocity c. For a charge entering a cavity at time $t = 0$ and leaving at a time $t = d/c = T_{cav}$, the charge sees a time-varying electric field during a transit time

$$T_{cav} = \frac{d}{c} = \frac{\pi}{\omega_0} \tag{2.32}$$

where ω_0 is the angular frequency of the accelerating mode. The accelerating voltage is given by

$$V_{acc} = \left| \frac{1}{e} \times \text{maximum energy gain during transit} \right|. \tag{2.33}$$

The voltage is given by the line integral E_z as seen by the electron (E_{el}) such that

$$V_c = \left| \int_0^d E_{el}\, dz \right|. \tag{2.34}$$

Since

$$E_{el} = E_z(\rho = 0, z) e^{i\omega_0 z/c + i\varphi}, \tag{2.35}$$

where φ is some arbitrary phase, we find

$$V_c = \left| \int_0^d E_z(\rho = 0, z) e^{i\omega_0 z/c} dz \right|. \tag{2.36}$$

For the pillbox cavity operating in the TM_{010} mode, we have

$$V_c = E_0 \left| \int_0^d e^{i\omega_0 z/c}\, dz \right| = \frac{dE_0 \sin\left(\frac{\omega_0 d}{2c}\right)}{\frac{\omega_0 d}{2c}}. \tag{2.37}$$

The electric field that the electron sees during the transit through the cavity is given by

$$E_{acc} = \frac{V_c}{d}. \tag{2.38}$$

2.2.4. Power Dissipation and Quality Factors

Our considerations of cavity characteristics and fields in a resonant RF cavity up to now have assumed that the walls of such structures were perfectly conducting, in which case, one would expect no power to be dissipated. In such cases, currents flow within a thin surface layer of the wall. However, this is not the case for real cavities and even superconducting cavities have thin surface currents that dissipate power at RF frequencies. These losses are an important feature of superconducting structures and also turn out to be very important in higher-order mode damping. The losses can be described by a surface resistance R_s defined as the power dissipated per unit area (dP_c/ds):

$$\frac{dP_c}{ds} = \frac{1}{2} R_s |\mathbf{H}|^2 \tag{2.39}$$

where **H** is the local magnetic field. Thus, dissipative losses in the region of say, a HOM damper, are characterized by the surface resistance of the damper as well as the magnetic field in the region of the wall of the damper.

Another important parameter in determining the character of an RF cavity as well as the extent of power dissipation within a cavity is the quality factor, Q_0, which is related to the power dissipation and defined as

$$Q_0 = \frac{\omega_0 U}{P_c} \tag{2.40}$$

where U is the stored energy and P_c is the power dissipated in the cavity walls. The Q_0 represents the amount of power dissipated per RF cycle in the cavity. The time-averaged energy in the electric field equals that in the magnetic field and thus the total energy is given by

$$U = \frac{1}{2}\mu_0 \int_V |\mathbf{H}|^2 \, dv = \frac{1}{2}\,\epsilon_0 \int_V |\mathbf{E}|^2 \, dv \tag{2.41}$$

where the integral is taken over the volume of the cavity. From 2.40, we may write the dissipated power over the interior surface of the cavity:

$$P_c = \frac{1}{2} R_s \int_S |\mathbf{H}|^2 \, ds. \tag{2.42}$$

Then, Q_0 can be written as:

$$Q_0 = \frac{\omega_0 \mu_0 \int_V |\mathbf{H}|^2 \, dv}{R_s \int_S |\mathbf{H}|^2 \, ds} \tag{2.43}$$

2.2.5. Shunt Impedance

In addition to characterizing the losses in a cavity through the surface resistance, we may also characterize losses via the shunt impedance R_a:

$$R_a = \frac{V_c^2}{P_c} \quad \text{(accelerator definition)} \tag{2.44}$$

in units of Ohms per cell. An even more meaningful quantity arises from the relation of the shunt impedance to the quality factor, sometimes termed the geometrical shunt impedance because it is independent of the size of the cavity:

$$\frac{R_a}{Q_0} = \frac{V_c^2}{\omega_0 U} \tag{2.45}$$

The quantity is a measure of the efficiency of the accelerating voltage for a given stored energy. Another way of thinking of this quantity that is useful for the study of higher order modes is as a measure of how strongly a given mode is excited by a given voltage. Note that multiplying the geometrical shunt impedance by Q_0 just recovers the shunt impedance. Thus, when one speaks of damping of a given mode, one means that either the Q-value of the mode or the geometrical shunt impedance or both is reduced, thereby reducing the total shunt impedance to a level such that the potential for the beam to excite these modes is minimized.

2.2.6. Higher-Order Mode Excitation

Until this point, the basic parameters of RF cavities have been discussed. In this section, the nature of higher-order modes is considered along with the consequences these modes may have on particle beams. The presence of higher-order modes can have destabilizing effects on particles that pass through a cavity since these charge-induced fields provide a retarding force. Furthermore, these modes may also affect subsequent bunches that pass through a cavity. In superconducting cavities, the higher-order modes may also increase the cryogenic losses due to additional power dissipation in the cavity walls. This can be very serious, since, even for modes that deposit small amounts of energy, this energy must be dissipated in the helium bath in which a niobium superconducting cavity resides. Unless the modes are damped sufficiently, additional refrigeration may be necessary and the resources necessary to provide the refrigeration may be expensive. For these reasons, eliminating or damping higher-order modes, particularly in superconducting cavities is of critical importance.

As we have seen, higher-order modes can be characterized by their shunt impedances R_a/Q_0 and a quality factor Q. The expressions for monopole and dipole modes are given by

$$\left(\frac{R}{Q}\right)_n = \begin{cases} \dfrac{\left|\int_0^d E_z e^{i\omega_n z/c} c\, dz\right|^2}{\omega_n U_n} & : \text{ monopole } [\Omega] \\ \dfrac{\left|\int_0^d E_z\,(\rho = a) e^{i\omega_n z/c} c\, dz\right|^2}{(k_n a)^2 \omega_n U_n} & : \text{ dipole } [\Omega] \end{cases} \qquad 2.46$$

where $k_n = \omega_n / c$ is the wave number of the mode with a frequency ω_n and stored energy U_n. R_a/Q_0 can be calculated in a variety of ways, but for this study, CST Microwave Studio was used to calculate the value of R/Q for monopole and dipole modes.

2.3. Ferrites as Absorbers of Higher-Order Modes

For much of this project, ferrites shall be employed as absorbers of the microwave radiation contained in higher-order modes. Ferrites are ceramic materials that are used in a wide variety of microwave applications. For our purposes, the most important feature of the ferrite used in this study is its microwave absorption. The mechanisms that are principally responsible for this loss include domain wall motion, domain rotation, and electrical resistivity. In a sample in which no magnetic field is applied, the ferrite shows no net magnetization because the magnetic domains have random orientation. The existence of domains in a ferromagnetic sample follows as a consequence of the process which minimizes the free energy in the ferrite. When a magnetic field is applied, the domains whose magnetization is aligned with the field grow in size while others shrink.

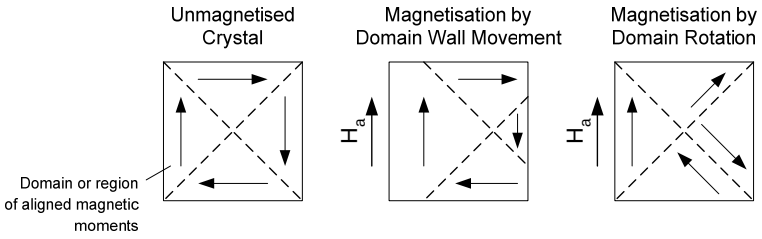

Figure 2.2 - Idealized domain patterns showing the fundamental magnetization processes [16].

When a time-varying magnetic field is applied, the motion of the domain walls produces movement of the domains and domain rotation, as shown in Figure 2.2, and thereby, dissipation

at low frequencies. At higher frequencies, the domain walls are no longer able to respond to the field, but the direction of the dipole moment inside individual domains rotates under the influence of the applied field, also leading to energy dissipation. In addition, the electrical resistivity of the ferrite also produces Ohmic dissipation. For the ferrite used in this study, the DC resistivity is about 0.25 Ω.

Ferromagnetic materials that have values of permeability μ, that are much large than the vacuum permeability, μ_0. It is often the case that such materials have are frequency-dependent, nonlinear response to the application of magnetic fields. Indeed, the permeability of a ferrite material is a complex parameter consisting of a real and imaginary component. The real component is reactive and imaginary component is resistive and contributes to energy losses in these materials. In general, these components are referred to as μ' (the real component) and μ'' (the imaginary component). For a ferrite material,

$$\mu(\omega) = \mu'(\omega) - j\mu''(\omega). \tag{2.47}$$

2.4. Energy Loss in Ferrites

In this section, we consider the expressions for energy and power in dielectric media and indicate how the complex permittivity and permeability express power dissipation in such media. Rather than deriving these expressions, we simply list them as a point of reference for understanding how ferrite interacts with electric and magnetic fields.

In source-free regions, the complex field equations are given by

$$-\nabla \times \mathbf{E} = \hat{z}(\omega)\mathbf{H} \tag{2.48}$$

and

$$\nabla \times \mathbf{H} = \hat{y}(\omega)\mathbf{E} \tag{2.49}$$

where

$$\hat{y}(\omega) = j\omega\epsilon_0 \tag{2.50}$$

and

$$\hat{z}(\omega) = j\omega\mu_0. \tag{2.51}$$

Here, ϵ_0 and μ_0 are the permittivity and permeability of free space. In the case of dielectrics, $\hat{y}(\omega) = j\omega\hat{\epsilon}$ where

$$\hat{\epsilon}(\omega) = \epsilon'(\omega) - j\epsilon''(\omega) = |\epsilon(\omega)|e^{-j\delta(\omega)} \tag{2.52}$$

where ϵ', ϵ'', and δ are real quantities. Now, ϵ'' is called the dielectric loss factor, and δ is called the dielectric loss angle. Based on this, we also define a commonly used quantity:

$$\tan\delta(\omega) = \epsilon''(\omega)/\epsilon'(\omega) \tag{2.53}$$

called the dielectric loss tangent. With these quantities, we can define the time-averaged energy:

$$W_e(\omega) = \frac{1}{2}\iiint \epsilon'(\omega)|E|^2\, d\tau \tag{2.54}$$

and power:

$$P_d(\omega) = \iiint \omega\epsilon''(\omega)|E|^2\, d\tau. \tag{2.55}$$

Thus, ϵ' contributes to stored energy and $\omega\epsilon''$ contributes to power dissipation. Quite often, measured values of $\epsilon(\omega)$ are usually expressed in terms of ϵ' and $\tan\delta$, or in terms of ϵ' and ϵ''.

A "perfect dielectric" would be one for which $\epsilon'' = 0$. Only the vacuum is a perfect dielectric. A "good dielectric" is defined to be one for which ϵ' remains almost constant at all frequency and for which ϵ'' is very small.

Similarly, for ferromagnetic matter such as ferrite,

$$\mu(\omega) = \mu'(\omega) - j\mu''(\omega) = |\mu(\omega)|e^{-j\delta_m(\omega)} \tag{2.56}$$

where $\mu',\ \mu''$, and δ_m are real quantities. Here, μ'' is called the magnetic loss factor, and δ_m is called the magnetic loss angle. As before we also define the magnetic loss tangent:

$$\tan\delta_m(\omega) = \epsilon''(\omega)/\epsilon'(\omega) \tag{2.57}$$

Then, the time-averaged energy and power are given by:

$$W_m(\omega) = \frac{1}{2}\iiint \mu'(\omega)|H|^2 \, d\tau \tag{2.58}$$

$$P_d(\omega) = \iiint \omega\mu''(\omega)|H|^2 \, d\tau \tag{2.59}$$

Thus, μ' contributes to the stored energy and μ'' to power dissipation. Measured values of $\hat{\mu}(\omega)$ are usually expressed in terms of μ' and $\tan\delta_m$ are, or in terms of μ' and μ'' [14].

The total power dissipation is the sum of the dielectric and magnetic losses in the material. Furthermore, ferrite ceramics, such as those used in this study, have unusually high dielectric constants. As a result, these materials are, in general, extremely lossy. It is also interesting to note that these materials tend to be quite nonlinear with respect to $\hat{\mu}$ as we shall explore later in this study. This property is often exploited in certain RF applications such as circulators and isolators because the materials can be easily magnetized. In this case, $\hat{\mu}$ assumes the form of an asymmetrical tensor, and magnetized ferrite can be used to build "nonreciprocal" devices. In this study, we shall not use these asymmetrical properties, and we assume that the ferrites are not magnetized.

Chapter 3

Higher-Order Modes in the Five-Cell LINAC Cavity

3.1. Introduction

The ERL test facility is based on a niobium superconducting 703.75 MHz five-cell cavity capable of accelerating electrons to 20 MeV in either a high-current mode with 0.5 A/0.7 nC per bunch at ~703 MHz, or in the high-charge mode with 5 nC at 10 MHz. Achieving these goals depends on damping of higher-order modes in the cavity. An imperative of the design of the five-cell cavity was to provide for damping of HOMs and to avoid trapping HOMs in the cavity [7]. The design incorporates techniques developed at Cornell and KEK-B for ferrite absorbers, leading to a cavity design with relatively large apertures allowing propagation of HOMs to the external absorbers. However, the exclusive use of ferrite absorbers for a multicell cavity and the space-constrained replacement of tapered end sections by step-transitions have distinguished the Brookhaven ERL project from others.

The five-cell cavity was designed by BNL, the niobium structures and cryomodules were fabricated by AES on Long Island [17], the ferrite absorbers were fabricated according to a Cornell design by ACCEL in Germany [18], and the cavity was processed at the Thomas Jefferson National Accelerator Facility [19]. The design of the cavity along with the beampipe transition and the coaxial FPC are shown in Figure 3.1. The ERL string assembled in its helium vessel with the thermal isolation sections and the ferrite absorber is shown in Figure 3.2.

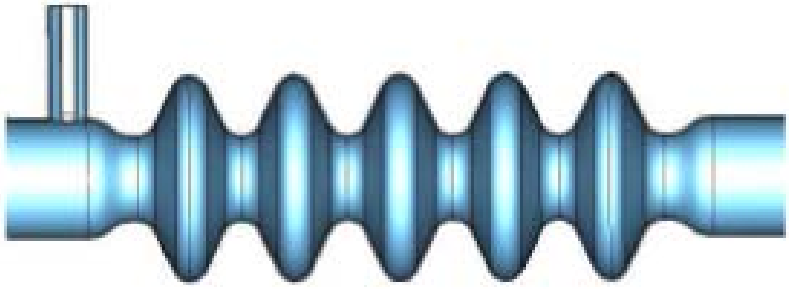

Figure 3.1: Graphic of the final design of the five-cell cavity, beam pipe transition and the coaxial FPC.

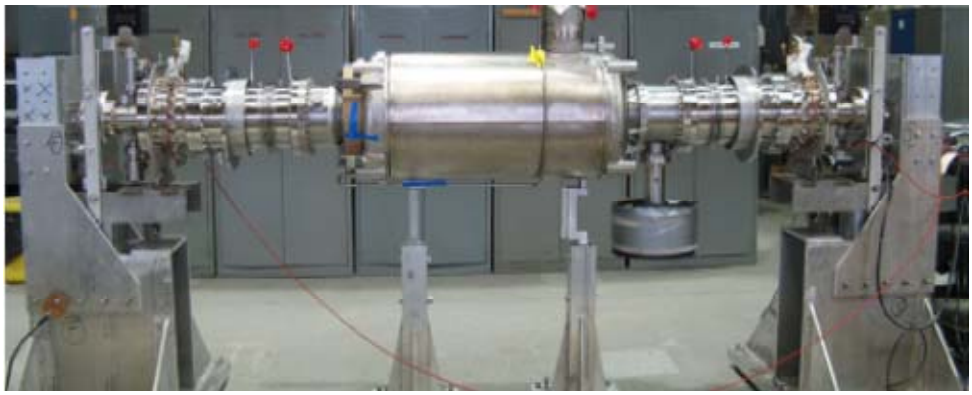

Figure 3.2: The ERL cavity string.

The work described in this thesis focused on both experimental characterization of higher-order modes in the cavity and computation of the lower-frequency monopole and dipole modes of the cavity with particular emphasis on working out the *R/Q* and shunt impedance of the modes and computation of the eigenmodes and forward-scattering coefficient (S_{21}) of the cavity aimed at determining a working model for the effect of ferrite absorbers on the higher-order modes of the cavity. Computation of the eigenmodes was done using the CST Microwave Studio application [15] and a model was constructed in the application based on AES fabrication drawings. For initial measurements, a prototype five-cell copper cavity as shown in Figure 3.3 was used to establish a reference. When the ERL cavity string was completed, measurements were carried out on this structure both during warm and cold-testing as shall be described below.

In addition to determination of *R/Q* and shunt impedance, the research and development efforts also resulted in a set of ferrite material parameters that were "portable" in the sense that they parameterized the material response of the ferrite at various frequencies and could subsequently be used in Microwave Studio stimulation.

Figure 3.3: The five-cell copper cavity with prototype ferrite HOM absorber.

In the sections that follow, these efforts and the techniques developed shall be described in detail along with the results.

3.2. Design of the Cavity

The basic objective in the design of the five-cell LINAC cavity was to provide for damping of HOMs in the cavity and the prevention of trapped modes in the cavity [9, [12]. Along with this consideration, the operating modes of the ERL greatly affected the design of the five-cell LINAC cavity including the overall shape of the cavity, the diameter of the apertures on either end, and the operating frequency of the cavity. The cavity was designed to operate at 703.75 MHz, the frequency of the 25^{th} harmonic of the bunch repetition frequency in RHIC with 360 bunches. This lower frequency allows for larger apertures on either end, resulting in a significant reduction of both longitudinal and transverse wakefields, reducing the HOM power depo-

sited by the beam and raising the threshold current for the onset of multibunch instabilities. Furthermore, cavity wall losses were minimized by maximizing the *R/Q* of the accelerating mode. The *R/Q* is roughly inversely proportional to the apertures of the cavity and decreases with large aperture, so attention was paid to increasing the aperture of the beamtubes to the maximum extent possible. As noted above, this also allows for HOMs to be easily extracted through the beampipes in a multicell structure. In addition, large cell-to-cell coupling was an important consideration in order to avoid trapping HOMs in the cavity. Five cells for the cavity was chosen in order to optimize effective damping while maintaining a reasonable accelerating gradient.

Therefore, the present ERL cavity was fabricated with a 41.874 cm equator, a 17.023 cm iris diameter, and a cell length of 21.331 cm at room temperature for cold operation at 703.75 MHz. The end cell is adjusted for field flatness and the cavity is connected to the HOM absorber by nominally 24 cm diameter beam tubes. A summary of the various parameters of the five-cell cavity is shown in Table 3.1.

Table 3.1 - Cavity Characteristics

Diameter [cm]	17
Frequency [MHz]	703.75
G (Ω)	225
R/Q (Ω)	807
Q @ 2K	4.5×10^{10}
E_p/E_a	1.97
H_p/E_a (mT/MV/m)	5.78
Cell-to-cell coupling	3%

3.3. Design of the Ferrite HOM Load

Ferrite material was chosen to damp HOMs in the five-cell cavity because of its proven capacity to effectively absorb microwave energy [12]. Several such materials are available, and C-48 ferrite was ultimately chosen. A ferrite layer on a section of the beam pipe is intended to act as a broadband HOM absorber, and these absorbers have proven to be successful on other storage rings including CESR and KEK-B [20]. The design for the structure used in the ERL is de-

rived from a Cornell design [21-23]. The absorbers have been tested up to 15 kW and, as this document will show, this is a viable option for high-power beams.

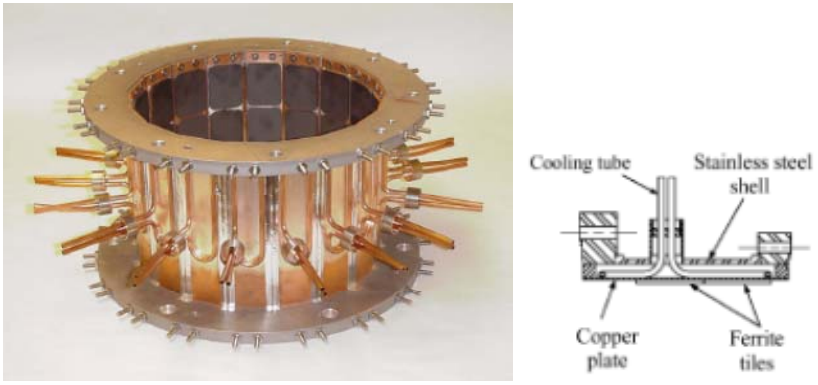

Figure 3.4: The HOM ferrite absorber prototype. The ferrite tiles are attached in copper plates provided with water cooling pipes. These plates are mounted on a stainless steel waveguide that is UHV-compatible and assembled in a clean room.

The HOM absorber for the superconducting ERL cavity is comprised of a cylindrical spool with ferrite tiles soldered to 10W3 Elkonite plates that line the inner wall of the structure, similar to a prototype model shown in Figure 3.4. The absorber consists of 18 such plates in a spool of diameter 25 cm, each plate with two tiles of ~24 cm dimensions. The production unit was designed and built to withstand ~10 kW HOM load [22]. In normal operation of the ERL cavity, the absorber is at room temperature but can be water-cooled through the tubes soldered to the plates [19]. The absorbing material used for the ferrite tiles is C-48 made by Countis Industries. The room temperature properties of the material were characterized for the Canadian Light Source by Microwave Properties North (MPN) [24].

3.4. Study of Ferrite-Damped Higher-Order Modes in the Prototype Cavity

Much of the effort described in this thesis focused on both the experimental and computational study of damping for the dominant lower-frequency modes, both dipole and monopole, in the five-cell cavity by the ferrite absorber. Many of the higher-order modes of the cavity had already been characterized during the design of the cavity [12]. However, this thesis focuses on

the effect of the ferrite on the damping of these higher-order modes. Measurements were completed on several different cavities: a prototype copper five-cell cavity which preceded the final design and fabrication of the niobium five-cell cavity. Determination of the HOM damping was largely accomplished by comparison of forward scattering measurements (S_{21}) using an Agilent ENA5071C network analyzer with simulations using the CST Microwave Studio (MWS) program [15]. The simulation model was created using detailed fabrication drawings from AES [17].

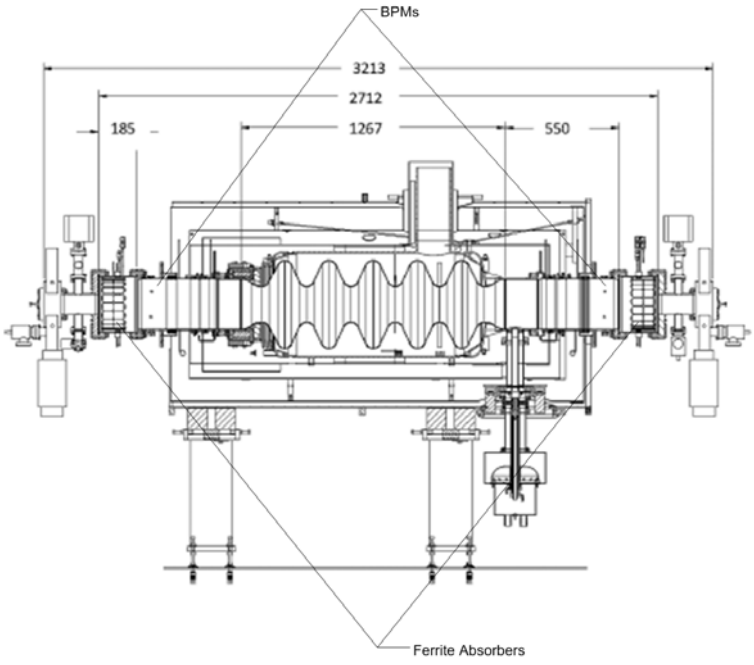

Figure 3.5: The principal dimensions of the ERL string (dimensions are in mm) [25].

In order to establish a reference for damping comparisons, measurements of the copper cavity with a single prototype absorber were performed. These measurements were completed using a variety of techniques including scattering measurements and field sampling to establish the field profiles of the various modes as shall be discussed below. Following these measurements, additional work was completed to obtain quantitative *R/Q* and shunt impedance values for the ERL cavity with all of the attachments assembled. A unique and necessary feature of this effort was to determine the ferrite properties in a form that was "portable" in the sense that a set of material parameters could be specified that would comport with the simplified representation of the ferrite absorber design that was built into the simulation.

The completion of the design and fabrication of the niobium five-cell cavity, along with its installation into the ERL cavity string, presented an opportunity to collect additional data through direct testing on the actual cavity to be used in the ERL. The ERL string is different from the prototype structure in that there are two ferrite absorbers located on either side of the cavity along with step-transitions to the beamtube. In addition, the cavity has asymmetric lengths on either side of the cavity, changing the distance between the five-cells and the higher-order mode absorber on either side.

3.4.1. Measurement of Bare Cavity

Measurement of the bare copper cavity was made to determine the frequencies and Q-values of the lowest order monopole and dipole modes allow for comparison with simulation studies. For these measurements, the cavity was excited by an input probe centered on a shorting plate on one side of the cavity. The output signal was taken from a probe centered axially on a shorting plate on the opposite end. An additional output probe was inserted in an RF pickup port located on the side of the cavity. Measurements were conducted with both the probe inserted in the pickup port as well as in the shorting plate. Signal levels were maximized by adjusting the input probe to achieve critical coupling for the fundamental cavity resonance at 703 MHz. S_{21} measurements were conducted using an Agilent ENA5071C network analyzer from one end to the other in the cavity as well as from one end to the pickup probe. In order to maintain the electrical length and node positions of the standing wave stimulated by the analyzer, a length of beam tube equal to the length of the ferrite absorber was added to the cavity.

3.4.2. Simulation and Measurement of Cavity without Ferrite Damper

A Microwave Studio model of the bare ERL cavity was prepared without the absorber based on detailed AES fabrication drawings. Eigenmodes of the model were calculated using the Jacobi-Davison method (JDM) within various frequency ranges as listed in the tables that follow. The simulation model frequency calculations were compared to the fundamental monopole modes that were measured in the prototype copper cavity. The measurement and simulation results appear below in Table 3.2. As the results show, good agreement was observed at all frequencies. There are some discrepancies between the simulation and measurement likely due to small dif-

ferences between the geometry of the model as built and the simulation. As for the Q-values, all measured values are greater than 10,000 but are below the calculated simulation values given a conductivity, $\sigma = 5.8 \times 10^7 \Omega^{-1}\mathrm{m}^{-1}$, due to joint losses. Similar studies were conducted for the dipole modes of the cavity, and these appear in Table 3.3.

In addition to this work, detailed studies of the dipole modes starting at ~1.6 GHz was also conducted in order to characterize these modes and compare them to simulation results. This effort took on particular importance when compared to the measurement of the in-situ niobium cavity as shall be seen later in this document. This set of modes represents the 4th dipole pass-band for the structure, and the band is important for study because the beampipe cutoff value for TM_{11} dipole modes is 1.52 GHz. Thus, these modes are easily studied by the network analyzer techniques described above. The aim of the measurements was to understand the field distribution of the modes by probing the modes at the end of the cavity and on the periphery of the structure. A rotating cylinder was placed on a calibrated, adjustable turntable and S_{21} measurements of amplitude and phase were measured every 45 degrees in order to map out the field distribution of the modes under study. The apparatus for the measurement is shown in Figure 3.6. These modes were then compared to those calculated via the simulation model. Measurements at 1.636 GHz and 1.659 GHz are shown in Figure 3.7 and Figure 3.8. Note that these measurements clearly show how the field and the phase are distributed azimuthally, point to a dipole distribution, in full agreement with the dipole field distributions given in simulation results.

Table 3.2 - ERL Cavity Monopole Modes [19]

f_{Data} [MHz]	f_{MWS} [MHz]	R/Q_{MWS} [Ω]	Q_{Cu}
683.8	683.3	0.00	21 600
688.9	688.3	0.05	22 200
695.6	694.7	0.00	23 000
700.9	699.9	0.20	23 700
703.0	702.0	397.76	22 100

Table 3.3 - Dipole Passbands in the Copper Cavity [19]

f_{Data} [MHz]	f_{MWS} [MHz]	Q_{Cu}	R/Q_{MWS} [Ω]
808.8	806.5	27,900	0.06
825.3	823.2	28,500	0.76
847.3	846.5	28,800	4.30
867.1	870.7	28,400	43.91
879.2	889.3	27,100	74.35
888.0	896.4	27,300	13.76
924.3	957.5	37,100	0.01
965.0	962.6	37,400	0.62
974.9	969.4	37,400	13.14
988.1	979.1	42,000	6.5
1001.3	993.3	50,400	0.1

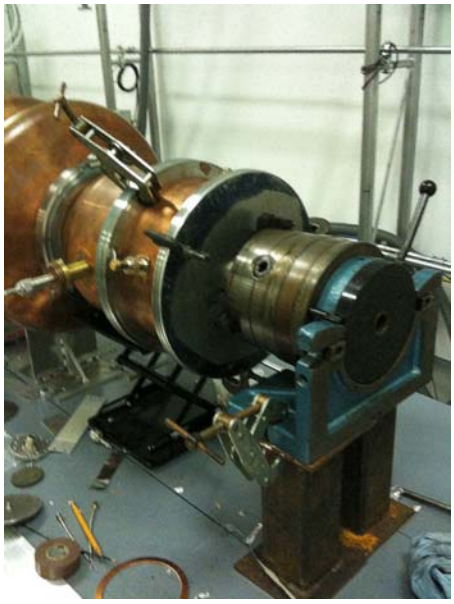

Figure 3.6: The turntable apparatus for measuring field profiles. At the right side of the photo, the turntable allows a probe inserted into the side of a rotating cylinder to be precisely placed at the desired azimuthal angle. The rotating probe is visible left of the center of the picture and a probe is inserted in the pickup port at the extreme left of the photo.

Table 3.4 - Table of Dipole Modes in 4th Passband

f_{Data} [GHz]	f_{MWS} [GHz]	$Q_{Cu\ (MWS)}$
1.636	1.624	61 815
1.660	1.650	57 631
1.689	1.684	55 510
1.699	1.694	56 459
1.705	1.699	57 901
1.718	1.711	78 409
1.729	1.721	60 484
1.733	1.722	70 055
1.734	1.725	64 624
1.772	1.765	60 784

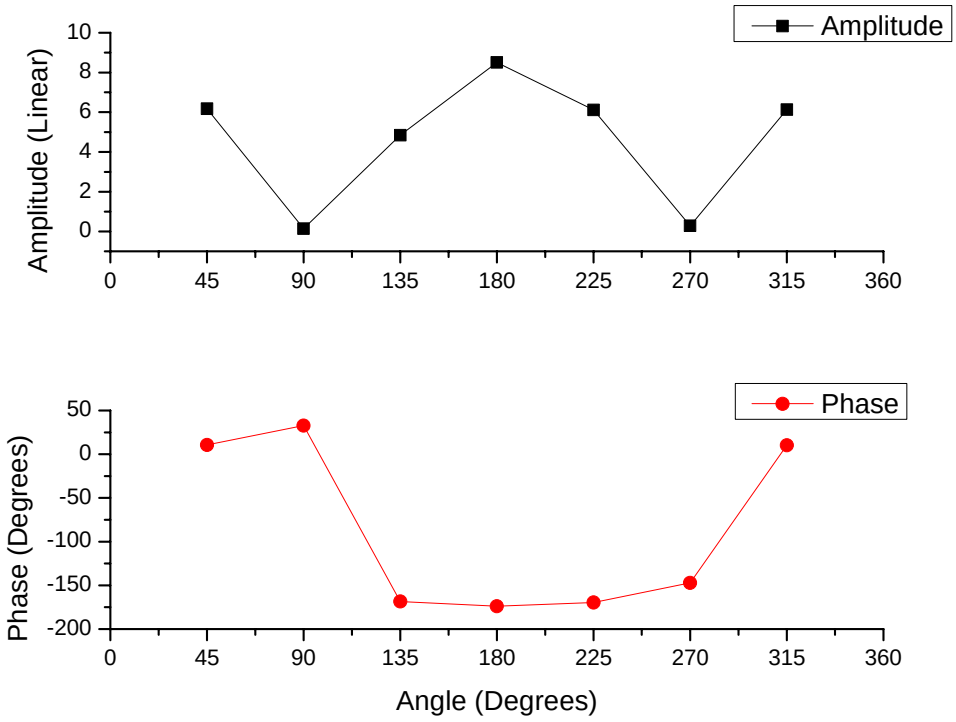

Figure 3.7: S_{21} amplitude and phase measurements of dipole mode at 1.636 GHz.

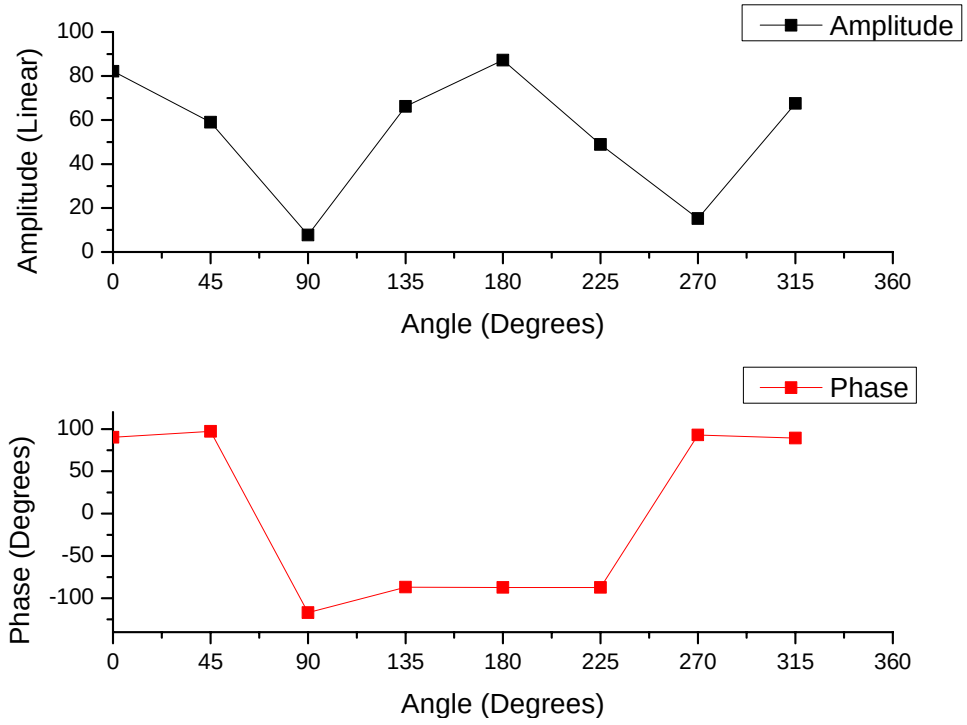

Figure 3.8: S_{21} amplitude and phase measurements of dipole mode at 1.659 GHz.

3.4.3. Simulation and Measurement of Cavity with Ferrite Damper

After the properties of the bare cavity were established, subsequent study focused on determining the damping of HOMs in the cavity with the ferrite damper attached. S_{21} measurements of the cavity were once again conducted, and the results were compared with the bare cavity. As Figure 3.9 shows, the damping ranges from approximately 10 to 20 dB on average below the reference signal. Note that the TM_{01} fundamental mode at 703 MHz is unaffected by the presence of the damper due to the monopole cutoff frequency at 956 MHz. Modes that are below the cutoff value of the beamtube do not interact with the ferrite damper due to the attenuation of modes below the cutoff frequency and thus are undamped by the ferrite. It is also interesting to note that there is rather strong damping by the absorber (black) and rather weak signal on the axis of dipole modes (red). Thus, the studies with the copper cavity confirm the strong damping effect of HOMs by the ferrite absorber.

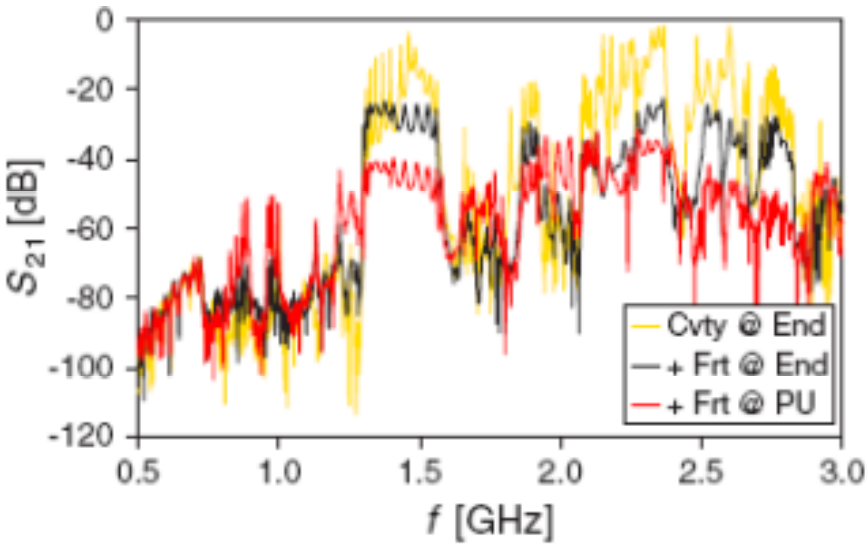

Figure 3.9: S_{21} in copper cavity without (yellow) and with (black and red) the ferrite absorber. [19]

To conduct the measurements, the signal level is maximized by adjusting the input probe to achieve critical coupling for the fundamental cavity resonance at 703 MHz. In order to maintain the electrical length and node positions of the standing waves, the ferrite absorber is replaced by a beam tube of equal length for the state without ferrite.

3.4.3.1. Modeling the Ferrite Absorber

The absorber and its Microwave Studio model were constructed as an assembly of many small ferrite tiles with gaps interspersed between the tiles and exposed metallic strips. The room-temperature properties of the ferrite were measured by Mouris and Hutcheon (MH) at the Canadian Light Source (CLS) [24]. The MH data for complex microwave permeability and permittivity data of the C-48 ferrite was obtained from measurements of small pellets, 3.5 mm in diameter and 3.175 mm thick at frequencies from 915 to 2800 MHz, covering the same frequency range as this study. Because the modeling of the absorber is computationally intensive given the complex, frequency-dependent material properties of the ferrite and the relative geometrical complexity of the absorber, a critical intermediate objective of initial R&D efforts with regard to the absorber was to find a set of "portable" absorber properties that could be applied to a geometrically simplified Microwave Studio model whose properties could then be calculated within the application and would be consistent with the actual behavior of the absorber and the cavity-

absorber system. Portability was obtained in the form of a ferrite cylinder with equivalent permeability and permittivity. The difference between the two models is illustrated in Figure 3.10.

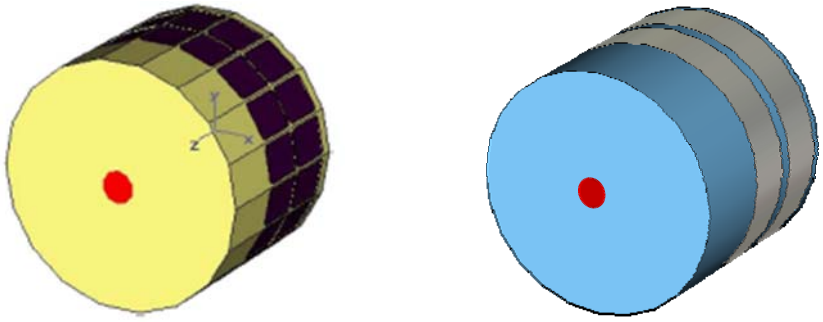

Figure 3.10: Microwave Studio models showing the actual RF space with tile ferrite bricks and the simplified structure used in the simulation models with "portable" ferrite parameters. Red dots in the models indicate the location of the probes to stimulate the cavity.

Many iterations of the basic model were required in order to achieve a set of portable parameters. The basic approach taken was to consider the absorber as a pillbox cavity with probes located along the axis of the cavity. An S_{21} measurement of the absorber was completed using the network analyzer, and the result was compared with the results of Microwave Studio simulation. The measured S_{21} coefficients for the absorber and a reference cavity with the same geometry covering the frequency range from 0.8 to 2.8 GHz are shown for various combinations of real and imaginary components of permeability in and Figure 3.11 and Figure 3.13. The basic strategy was to find a reasonable starting point and then vary either the real or imaginary part of the permeability at a single frequency. The Debye model, as described below, then provided the interpolation of the permeability throughout the frequency range of interest. The plots also show clear TM_{01n} resonances in the reference structure at 0.92 and 1.22 GHz. In addition, TM_{02n} resonances are visible at 2.12, 2.28, 2.67 GHz, whereas the other visible resonances are attributed to dipole modes. The TM_{010} and TM_{020} resonances are fully damped in the absorber and substantially damped at TM_{011} and TM_{021}.

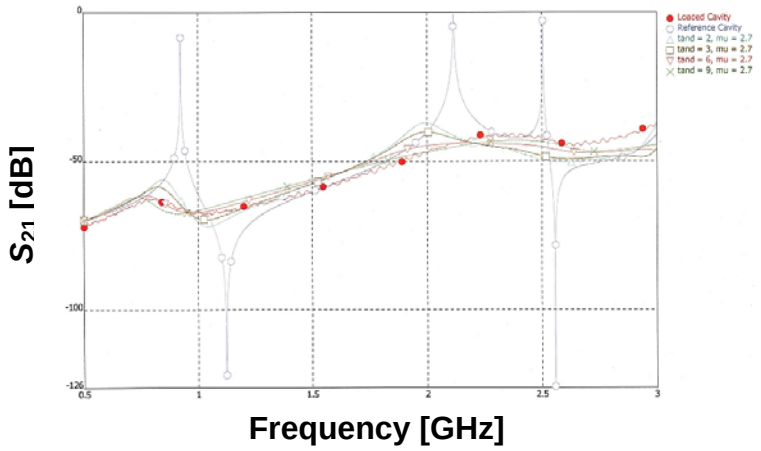

Figure 3.11: Plot of various simulation runs for a model with a solid ferrite sheet in which tan δ is varied while μ' of the ferrite is held constant. The plot compares the S_{21} measurement and simulation data. Agreement between the measurement and simulation data is closer at low frequency than at high frequency.

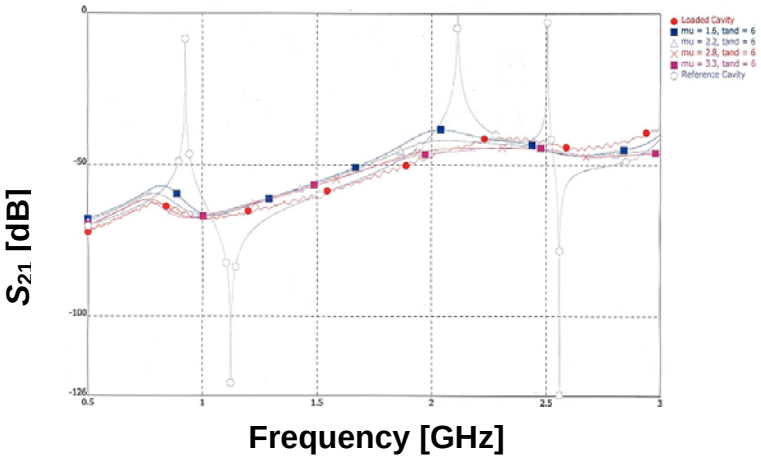

Figure 3.12: Plot of various simulation runs for a model with a solid ferrite sheet in which the $\mu'$of the ferrite in the simulation was changed while holding the tan δ constant. The plot compares the S_{21} measurement and simulation data including measurements for the absorber and the reference structures. Once again, agreement at low frequency is more easily achieved than at high frequency.

The absorber data was compared with simulation results from a model with fully tiled ferrites (tld), as shown in Figure 3.10, and one with the ferrite represented by a 3.15 mm thick cylindrical tube of 10 cm length (sld). The ferrite parameters, $\mu = \mu' - j\mu''$, are entered into the MWS frequency domain solver program in the form of a Debye 1st order model with constant tangent

delta, given by the real part, μ' and the $\tan\delta = \mu''/\mu'$ defined at a specific frequency. This frequency dependence of $\mu = \mu'(1 - \tan\delta)$ is obtained in the program from the expression:

$$\mu = \mu_\infty + \frac{\mu_0 - \mu_\infty}{1 + j\omega\tau} \tag{3.1}$$

together with the constraint that

$$\frac{d\tan\delta}{df} = 0 \tag{3.2}$$

at the defining frequency. Of course, changing the material definition frequency while maintaining the material parameters at this frequency constant changes the μ and $\tan\delta$ values at other frequencies. For the ferrite permittivity only the real part of the Mouris and Hutcheon value of $\epsilon \approx 13(1 - j0.04)$ was used.

Comparing the S_{21} data measured in the absorber prototype against simulations with variable μ' and $\tan\delta$ yielded the approximate value of $\mu \approx 4(1 - j2.5)$ defined at 1 GHz for Microwave Studio, or, alternatively $\mu_0 \approx 55.93,\ \mu_\infty \approx 2.074$, and $\tau \approx 5.193$ ns for Eq. (3.1) over the frequency range from 0.8 to 1.6 GHz. This was deemed to be sufficient for the semiquantitative accuracy required for the HOM study in the ERL cavity.

3.4.3.2. Comparison with Measurement of Ferrite Properties

Based on the methods described above, portable ferrite parameters were found leading to a value of $\mu \approx 4(1 - j2.5)$, defined at 1 GHz. This value was subsequently applied over the frequency range from 0.8 to 1.6 GHz. This portable approximation appears to agree well with the measurements conducted by Mouris and Hutcheon, and the results are compared in Figure 3.13. Differences between the two may be attributable to different measurement geometries, and it is possible that additional model iterations might produce better matches, but the agreement was deemed sufficient for subsequent efforts.

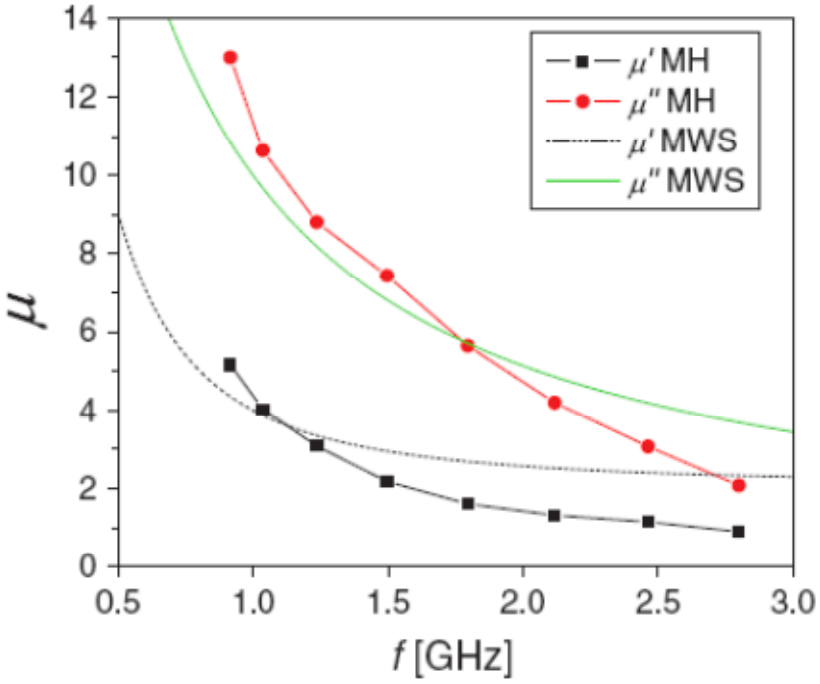

Figure 3.13: Comparison of ferrite permeability $\mu \approx 4(1 - j2.5)$ used in the Microwave Studio stimulations with Mouris and Hutcheon results. [19]

3.4.3.3. Validation of Portable Ferrite Parameters with Prototype Cavity

Testing of the portable ferrite model was performed by simulating the dipole modes in the five-cell copper prototype cavity and comparing these results to measurement. The S_{21} curves were measured in the prototype cavity with either the ferrite absorber or a copper tube of equal length attached to the cavity. The results of measurement with and without the absorber are shown in Figure 3.15. Validation of the portable ferrite parameters was obtained by considering the frequencies and quality factors of the dipole resonances in the prototype cavity. The measured and eigenvalue simulated results for the six TE_{11n} and the five TM_{11n} resonances are listed in Table 3.5. It is notable that the resonance frequencies in the mid-range of the table are changed by the presence of the absorber. Furthermore, one of the additional resonances, found in the simulation, appears to be located at the ferrite in the beam tube and has low Q and very low R/Q values.

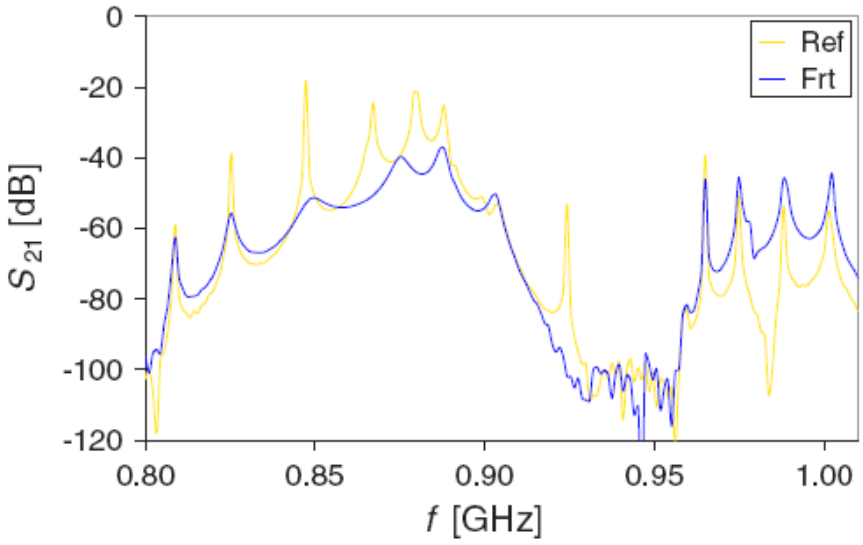

Figure 3.14: HOM dipole modes in the five-cell copper cavity with the absorber (Frt) and without (Ref) [19].

Table 3.5 - Simulation of Copper Cavity with Tiled and Solid Absorber [19]

f_{Data} [MHz]	f_{tld} [MHz]	f_{sld} [MHz]	Q_{Data}	Q_{tld}	Q_{sld}	R/Q_{Cu} [Ω]	R/Q_{tld} [Ω]	R/Q_{sld} [Ω]	R_{tld} [Ω]	R_{sld} [Ω]
--	--	802.3	--	--	1969	--	--	0.09	--	--
808.8	808.4	820.3	1780	416	591	1.04	1.06	0.88	1887	1566
825.3	833.9	845.2	415	151	234	2.99	3.43	4.57	1423	1897
848.9	847.7	872.4	120	17	21	27.4	0.075	0.05	9	6
875.7	861.8	875.6	162	174	128	59.6	33.9	24.97	5492	4045
887.0	879.0	891.7	332	1,599	1,077	38.2	38.4	31.12	12 749	10 332
903.1	903.3	916.4	290	41.6	33	13.9	13.8	10.7	4002	3103
959.5	950.0	960.4	22 300	36 200	66 330	0.033	0.011	0.006	245	134
965.0	954.7	965.1	6670	7189	11 070	1.39	1.21	1.52	8071	10 138
974.9	962.1	971.8	2000	2766	4402	10.1	8.65	10.29	17 300	20 580
988.1	973.1	981.3	1064	1398	1978	3.43	3.38	3.40	3596	3618
1000.2	986.1	993.1	1512	1922	2701	1.06	1.09	1.17	1648	1769

The first three columns in compare the measured frequencies (Data) with simulated values for the tiled (tld) and solid ring (sld) models showing good quantitative agreement. The *Q*-values show qualitative agreement between data and simulation; the tiled and solid model results are within a factor of 2, but do not favor either model. Except for one or two resonances, the *R/Q* values are in reasonable agreement. In these cases, *R/Q* data becomes important in making a

final identification of these modes. From the data, it was concluded that the tiled structure can, in fact, be successfully modeled by a solid ring, using the empirically derived portable ferrite parameters without significant loss of accuracy.

3.4.3.4. Measurement of the Effect of a Step Transition after the Absorber

The ERL cavity string incorporates a somewhat unusual feature in its design in that the transition from the cavity and absorber to the beampipe adjacent to the absorber is characterized by an abrupt change in diameter from 24 cm to 10 cm. Previous modeling and design efforts had suggested that this transition might enhance the HOM damping of the absorber by enhancing the magnetic field in the location of the absorber. To test this notion, studies were carried out in which the absorber was attached to the prototype cavity, and the assembly was measured in both an open and shorted configuration, with a shorting plate covering the opening of the absorber. The shorted configuration was taken to represent the step condition whereas the open configuration was taken to represent a tapered transition. Table 3.6 shows the measured frequency and *Q*-value (cavity) as well as the MWS simulation calculations for the shorted (short) and open models. In this case, a waveguide termination was introduced into the model, representing an ideal, perfectly terminated port with no reflections at all frequencies.

The data appear to show that the step transition is beneficial for several of the HOMs. The *Q*-values for many of these modes show greater damping over that of the open configuration, confirming that there is, for certain modes, an apparent enhancement. It is also interesting to note that for these modes, the *R/Q* is lower overall. This data, coupled with the space-saving advantage of the step transition over a taper appears to justify the design choice.

Table 3.6 – Measured and Simulated Results for the Shorted and Open Prototype Cavity [19]

f_{cavity}^{short} [MHz]	f_{cavity}^{open} [MHz]	Q_{cavity}^{open}	Q_{cavity}^{short}	Q_{MWS}^{short}	Q_{MWS}^{short}	R/Q^{short} [Ω]	R/Q^{open} [Ω]
808.8	808.8	1780	670	591	263	0.9	0.6
825.3	826.4	415	490	234	203	4.6	6.5
848.9	849.5	120	300	21	--	0.1	--
875.7	873.7	162	211	128	326	25.0	44.6
887.0	886.9	332	275	1077	1849	31.1	38.8
903.1	901.2	290	730	33	73	10.7	15.1
959.5	959.5	22 300	12 160	66 330	72 224	0.0	0.0
965.0	965.0	6670	2815	11 070	10 171	1.5	1.3
974.9	974.9	2000	890	4402	3694	10.3	10.9
988.1	988.1	1064	586	1978	1263	3.4	3.8
1000.2	1001.3	1512	1033	2701	1271	1.2	1.2

3.4.3.5. Measurement and Identification of Dipole Modes

Data was also collected from measurement below 1 GHz, and several dipole modes could be identified and compared to simulation results. For these measurements, the prototype cavity was used, and ferrite absorbers were attached to either side of the cavity to more fully match the actual arrangement of the ERL cavity string. Then, two simulation runs were conducted in which the ferrite was removed from the simulation (no absorber) and then added with the portable material parameters discussed above ($\mu = 4(1 - j2.5)$ defined at 1 GHz). This is identified as Frt in Table 3.7. The data shows that the effect of the ferrite is rather small, with less than ~0.5% change in frequency, but slightly higher *R/Q* values.

The data also show that the damping of the *Q*-values is about 2 orders of magnitude larger for the TE_{11}-like modes in the 800 MHz range, but appears to be significantly lower for some TM_{11}-like modes in the 900 MHz range. *R/Q* values from the simulation with and without the absorber are largely determined by the cavity geometry and are therefore, in good numerical agreement. The data in Table 3.7 shows a comparison of measurement to simulation data and

suggests that the dipole modes are effectively damped by the ferrite absorber even when a step transition is included.

Table 3.7 – Dipole Resonances in the ERL Cavity [19]

$f_{no\ absorber}$ [MHz]	f_{Frt} [MHz]	f_{Data} [MHz]	$R/Q_{no\ absorber}$ [Ω]	R/Q_{Frt} [Ω]	Q_{Frt}	Q_{Data}	R_{Frt} [Ω]	R_{Data} [Ω]
805.1	803.4	--	0.04	0.13	588	--	76	--
810.2	808.4	807.80	0.37	1.12	150	900	168	1008
817.9	816.1	--	1.18	0.73	136	--	99	--
829.2	827.0	825.18	0.32	0.22	265	370	59	81
851.6	849.5	848.99	13.75	11.84	493	130	5839	1539
874.6	872.6	--	55.08	49.33	379	--	18 697	--
890.2	888.1	--	43.02	42.01	163	--	6847	--
897.1	895.0	--	21.19	22.78	201	--	4578	--
929.0	926.2	--	10.12	6.66	104	--	693	--
943.8	940.7	--	5.80	8.58	79	--	678	--
957.6	956.1	958.34	0.05	0.04	40 370	9500	1571	380
963.7	962.2	964.76	2.64	2.65	6410	3350	16 977	8878
975.4	973.7	977.15	7.89	8.07	2132	830	17 210	6698
991.8	989.8	995.46	2.41	2.39	1644	205	3925	490

3.4.4. Measurement of the Niobium Cavity and ERL String

Following the measurement of the prototype copper cavity, the niobium cavity to be used in the Energy Recovery LINAC became available for testing along with the vacuum string assembly with ferrite dampers. As seen in Figure 3.5, the two sets of beams position monitors (BPM), located at each side of the cavity vacuum string, are intended for centering the beam during operation. At the same time, the capacitive BPM buttons are available to collect the HOM cavity data, and, in fact, provided the strongest signals in the fully assembled and installed cavity. Each of the BPMs has three pickup probes spread evenly around the circumference, 120-degrees apart (referred to in what follows as 2-, 6-, and 10-o'clock BPM probes). Also available in the cavity string is a pickup probe (PU) that, because of its proximity to the cavity, serves primarily as a monitor of the fundamental field. This probe also has a rather high external Q ($\sim 3 \times 10^{11}$), but, nonetheless also provides HOM signals. The setup also allowed limited access to the fundamental power coupler (FPC).

Measurements of HOM frequencies and Q-values were conducted using an Agilent E5701C network analyzer. S_{21} measurements between the BPMs using various combinations of the BPMs located on either side of the cavity. Many measurements were conducted between the BPMs located on the bottom of either side, referred to as the "6 o'clock" position. An important concern of measurements was to determine trapped modes within the beam tubes. As has been discussed previously, the presence of the step transition was a concern because it may also allow for the introduction of additional resonances that may interact with the beam. To study these beam tube resonances, the two probes located 2- and 10-o'clock were also used for measurement. As before, mode identification and calculation of shunt impedances was determined using simulation results from Microwave Studio and by correlation with room-temperature copper prototype results.

3.4.4.1. Measurement of the Normal-Conducting ERL Cavity

The HOM spectrum for the frequency range from 0.7 GHz up to 3 GHz is shown in Figure 3.15. Several dipole passbands are clearly evident in the sample at 800 MHz, 1 GHz, 1.25 GHz, and 1.65 GHz. In this measurement, the resonances appear as peaks in the BPM-to-BPM measurement from one side of the cavity to the other side. Resonance peaks, including the fundamental peak below 800 MHz, are not visible in the measurement due to the cutoff of the beampipe. It is interesting to compare this S_{21} "through" measurement to a measurement of resonances at one side of the cavity using two of the three BPMs available on each side. A comparison of the two measurements is shown in Figure 3.16. In the "local" measurement, i.e., the measurement of BPMs on one side of the cavity ("BPM 6-6"), the resonances that, in the "through" measurement ("BPM 2-10") appeared as peaks, now appear as "dips" in the signal due to energy pulled out of the signal and stored in the cavity. The five proper cavity resonances, are clearly visible in both figures, although in Figure 3.16, the $4\pi/5$ and the π modes are spread out and overlap due to the strong damping of these modes. Local measurement resolves these peaks somewhat, allowing them to be clearly discernable, and represents the transmission signal for the capacitive coupling between the BPM probes, which is nominally flat but is reduced at a resonance due to the power pulled into the cavity. Mode identification is conducted by establishing correlations between data and Microwave Studio simulations as well as copper prototype mea-

surements. However, this becomes increasingly difficult as frequency increases due to the proliferation of modes.

As mentioned above, resonances of the beam tube are also evident in measurement. This is an additional consideration that complicates mode identification, and in some cases reaches into the large radius end-cell but not into the rest of the cavity. An example of such a beam tube mode is observed at 1.6 GHz as shown in Figure 3.17. Notice that this is a dipole mode localized in the beamtube but also extending into the first cell of the cavity. This mode is adjacent to the fourth dipole passband.

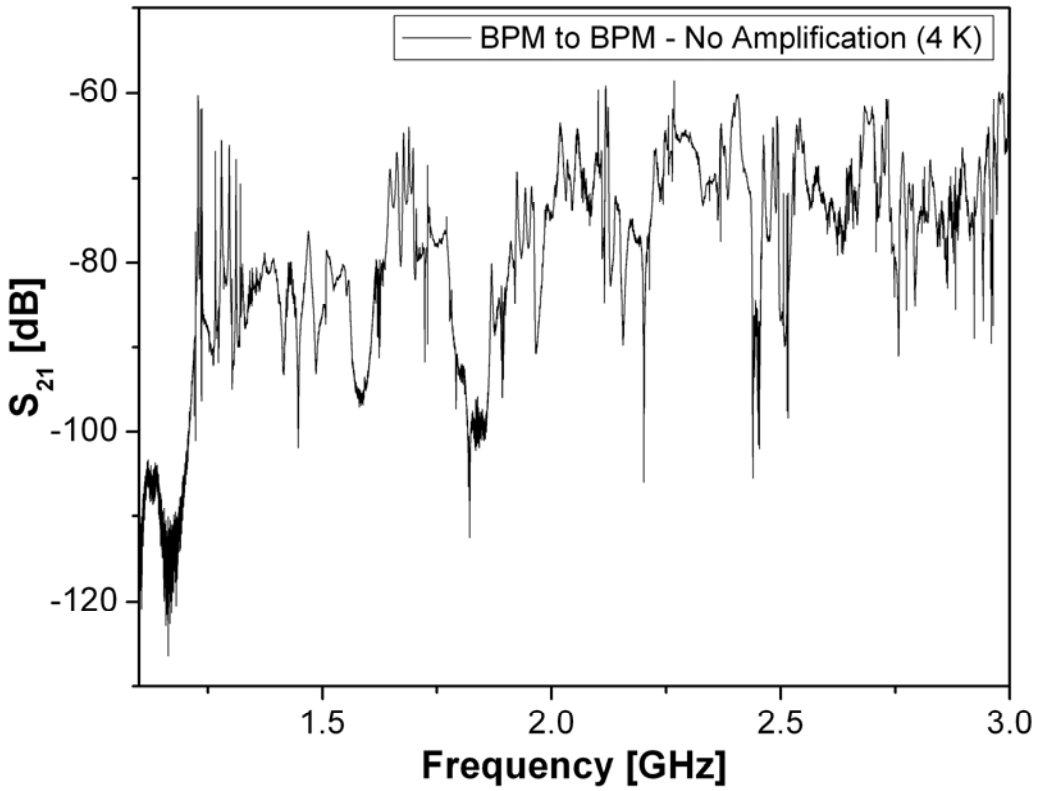

Figure 3.15: S_{21} transmission measurement of the ERL five-cell cavity from 0.7 GHz to 3 GHz using BPM pickups in the cavity string.

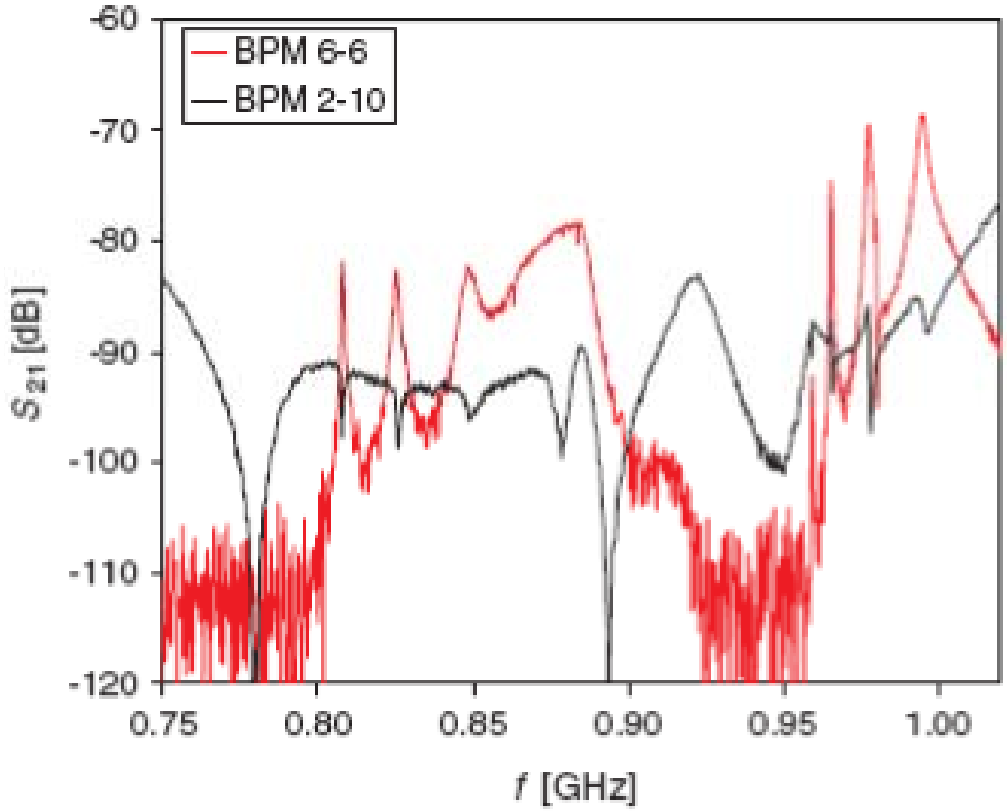

Figure 3.16: HOM spectra of the five-cell cavity at room temeperature in the frequency range of the first dipole passband. The red curve shows the transmission through the cavity (BPM 6-6), while the black curve shows transmission between two probes in the upstream tube (BPM 2-10). The notch at the far left of the plot is a beampipe mode rather than a cavity mode. [25]

3.4.4.2. Measurement of the Superconducting ERL Cavity

Measurement of HOMs was also conducted at superconducting temperature, both at 2K and 4K. The results show that most modes are also effectively damped in the superconducting case as they were in the normal-conducting case. As shown in Figure 3.18, a comparison of the normal-conducting case and the superconducting case shows only a small increase in *Q*-values. Of all the modes, a mode of particular concern in the mode at 957 MHz, that is relatively uncoupled to the ferrite absorbers and has a rather large *Q*-value (~50,000). Figure 3.19 shows the spectrum of this mode at 4K, 2K and room temperature. Because of the smaller losses, the quasi-trapped mode that appears at the far left of the plot shows a significantly stronger transmitted signal at 2K in comparison to the neighboring damped resonance. It is also interesting to note the clean split in frequencies for the dipole mode at 960 MHz.

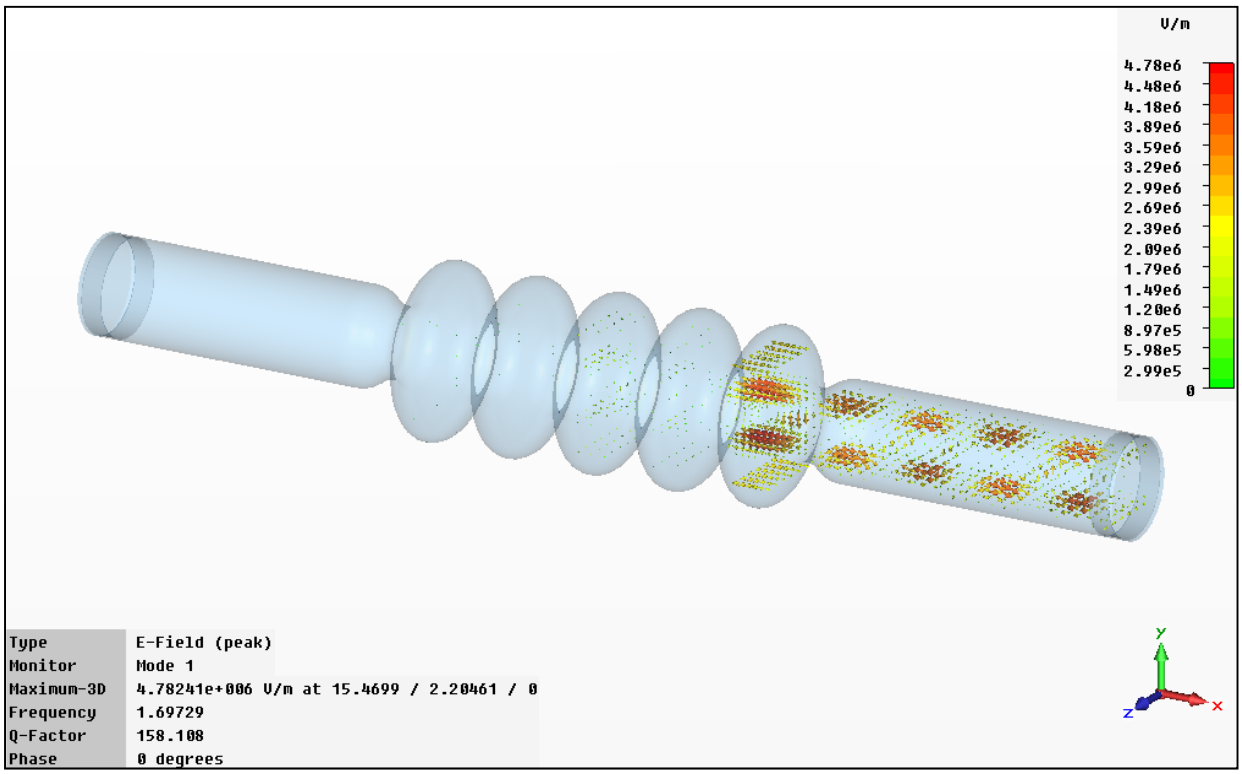

Figure 3.17: A beampipe mode at 1.70 GHz in the five-cell cavity. Notice how the mode extends into the first cell of the cavity.

Simulation and measurement were also compared, and the results are summarized in Table 3.8. Resonance frequencies are labeled f_{data} and were measured using a network analyzer between the bottom BPMs for "through" measurements (f_{6-6}) or "locally" in the upstream BPM (f_{2-12}). As the table shows, there are some differences in simulated and measured frequencies are likely due to weak coupling of some modes, mechanical changes in the cavity because of the cooldown as well as small changes in material properties (e.g., conductivity) that are not accounted for in the model, and some broadening of rotated HOMs. In addition, the 3D model is fairly basic, lacking details of the FPC port as well as the BPM probe structures.

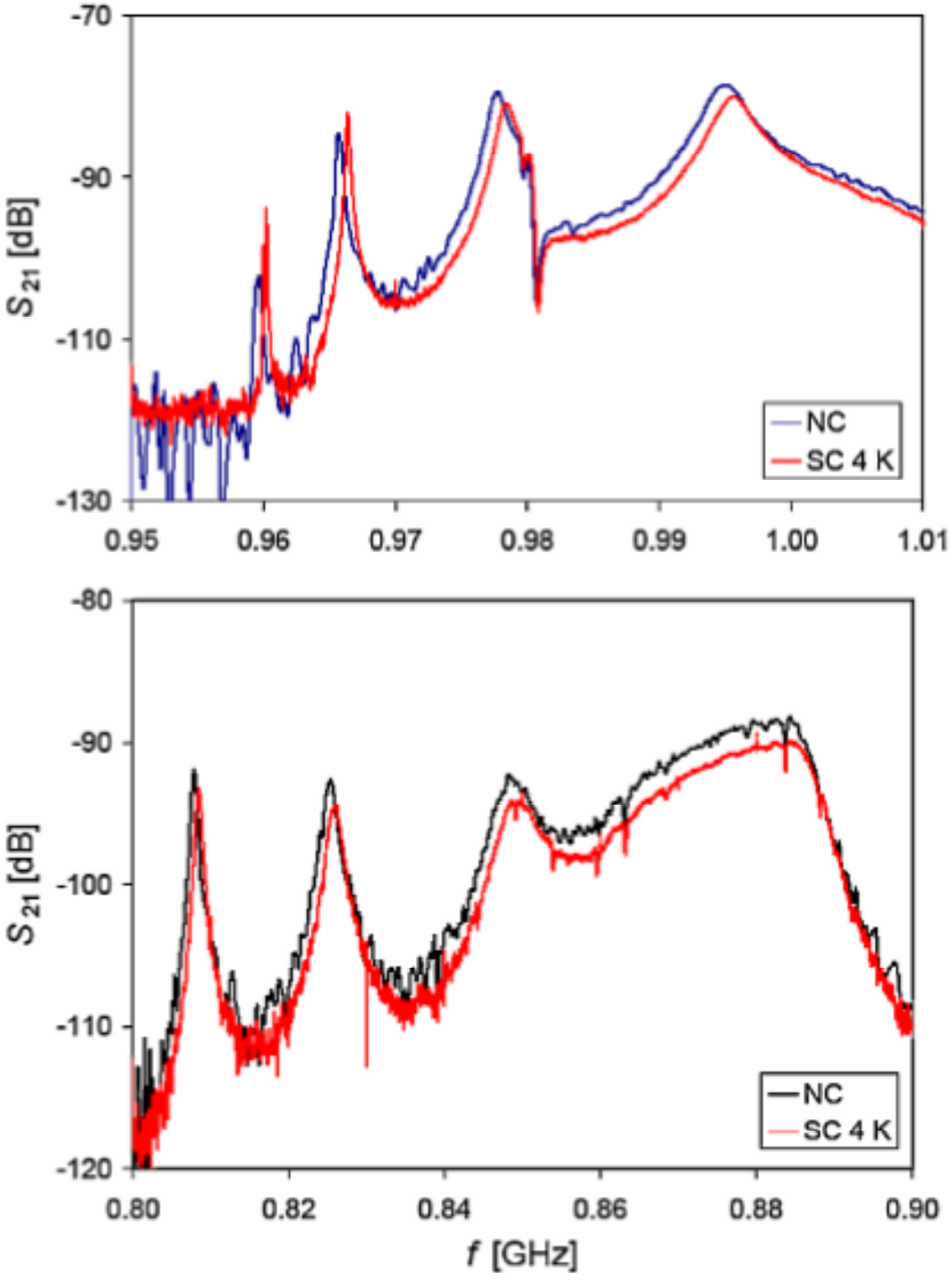

Figure 3.18: Spectra of higher-order modes in the ERL five-cell cavity in the normal conducting (NC) and in the superconducting state (at 4K). [25]

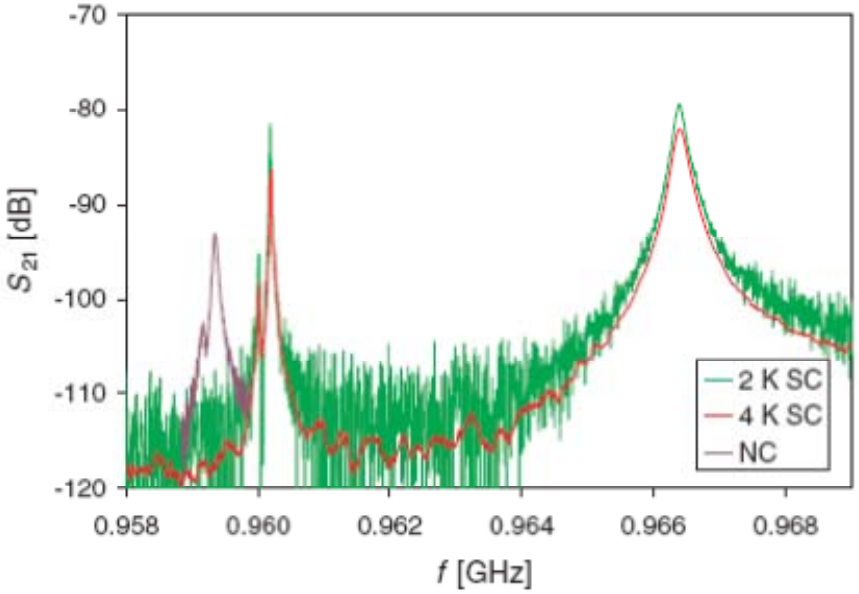

Figure 3.19: Comparison of the resonance curves of the quasi-trapped mode (left) with the neighboring damped mode (right). The direct Q measurements at left are 9,500, 44,200, and 47,800 for NC, 4K, and 2K. Also seen is the frequency shift in the resonance peak at the far left of the plot due to the cooldown. [25]

Table 3.8 - Dipole Modes in R&D ERL Cavity

Q_{WGT} and Q_{FRT} are simulated with a waveguide and ferrite dampers.

Data				Simulations					
f_{2-12} [MHz]	f_{6-6} [MHz]	Q_{NC}	Q_{SC}	f [MHz]	$R/Q_{1\,cm} \times 10^3$ [Ω]	R/Q [Ω]	Q_{WGT} [Ω]	Q_{FRT} [Ω]	R_{SH} [Ω]
770	--	--	--	752	3.2	0.13	174	382	49
780	--	--	--	755	3.6	0.14	18	322	46
808	808.4	900	874	806	1.4	0.05	611	586	28
826	825.9	370	386	825	20.8	0.70	174	335	233
850	849.6	130	141	852	432.1	13.6	89	605	8225
878	--	--	--	875	1777.8	52.9	18	433	22 921
894	--	--	--	890	1593.3	45.6	15	176	8020
959	960.2	9500	47 800	958	2.0	0.1	2820	44 391	2216
966	966.4	3350	4720	964	103.9	2.6	927	6683	17
978	978.3	630	730	976	317.6	7.6	379	2288	17 392
998	995.6	205	326	993	98.9	2.3	9	1735	3969
--	--	--	--	1026	4.0	0.1	9	67	6

3.5. Conclusions

The results of the measurements on the five-cell cavity in various measurement configurations confirm the effectiveness of the absorbers on HOM damping. The action of the absorbers appears to be well-predicted by modeling efforts at least for the modes within the bandwidth under study. The data also appears to confirm the effectiveness of the design choices that were made for the absorber including the somewhat unusual choice of a step transition.

Furthermore, the data also confirm the modeling efforts and, in particular, the use of a "portable" set of ferrite parameters, used to simplify modeling efforts. As noted, the agreement between measurement and calculation is good over a range of frequencies and mode types, with small differences arising likely due to differences in geometry between the model and the actual cavity and the nature of the splitting assumptions inherent in the modeling approach itself. In turn, the differences in geometry occur because some of the more intricate features of the actual cavity were left out of the model. Nonetheless, the results indicate the Microwave Studio models, using the portable parameter approach, provides the ability to fairly precisely calculate frequency and shunt impedance data despite the challenges that the lossy, frequency-dependent character of the ferrite absorbing material poses.

Chapter 4

Damping Higher-Order Modes in the Electron Gun Using the Fundamental Power Couplers

4.1. Design of the Gun Cavity

The gun cavity for the ERL is a superconducting half-cell structure that is designed to operate in two modes: a high-current mode and a high-charge mode. The high-current mode of operation envisions an average current of 500 mA with a bunch charge of 1.4 nC at a repetition frequency of 703.75 MHz. Electrons in this mode are accelerated to an energy of 2.5 MeV. In the high-charge modes of operation, the gun is designed to operate with an average beam current of 50 mA and a bunch charge of 5 nC. The repetition rate for this mode is 9.4 MHz. A table summarizing these parameters along with other design features appears in Table 1.1.

From the initial concept for the gun, a number of iterations followed until a final geometry was settled upon that provided the necessary longitudinal focusing and emittance at the exit of the gun. Ultimately, the design included a gun cavity with a diameter of 37.9 cm at the equator and a beampipe diameter of 10 cm. A schematic of the gun appears in Figure 4.1. A critical component of the gun is the design of the fundamental power couplers (FPCs). Because the gun is required to generate a 2.5 MeV beam with a relatively high average current, the required RF power is ≥ 1 MW, and, therefore, requires rather strong coupling to the fundamental with a Q_{ext} of $\sim 4 - 5 \times 10^4$. Several options for the FPCs were considered, and, finally, a coaxial coupler

with a “pringle” shaped tip was determined to be an effective choice. This tip, which was originally designed for the Cornell ERL injector, features a contour radius conformal with the beampipe radius and, in operation, maximizes coupling while minimizing wakefield effects. For the gun, a dual-coupler design is employed which minimizes the destabilizing effects of non-zero fields on axis, particularly at low energy, and also halves the power required in each coupler. Figure 4.2 shows the elements of the gun. In Figure 4.3, a schematic of the fundamental power coupler is shown. A variety of design considerations for the FPC were studied including penetration depth and shape of the “pringle” tip, among others [7].

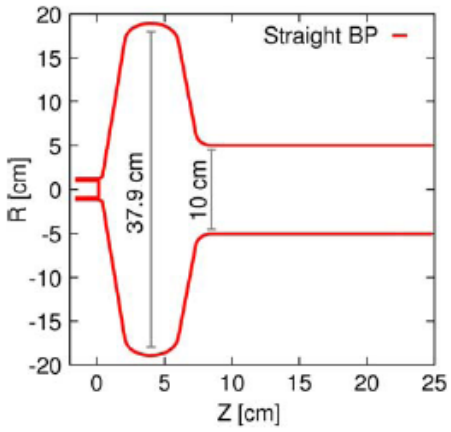

Figure 4.1: Schematic of gun cavity and beampipe. The placement of the FPCs is not shown in this figure.

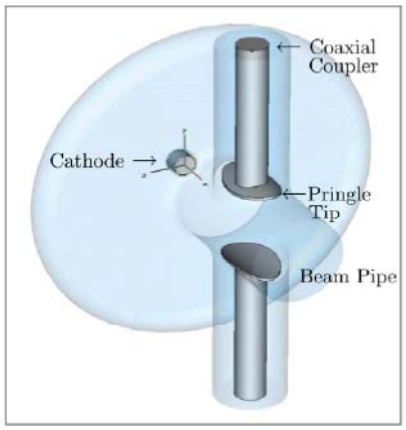

Figure 4.2: Schematic of the cavity showing the fundamental power couplers.

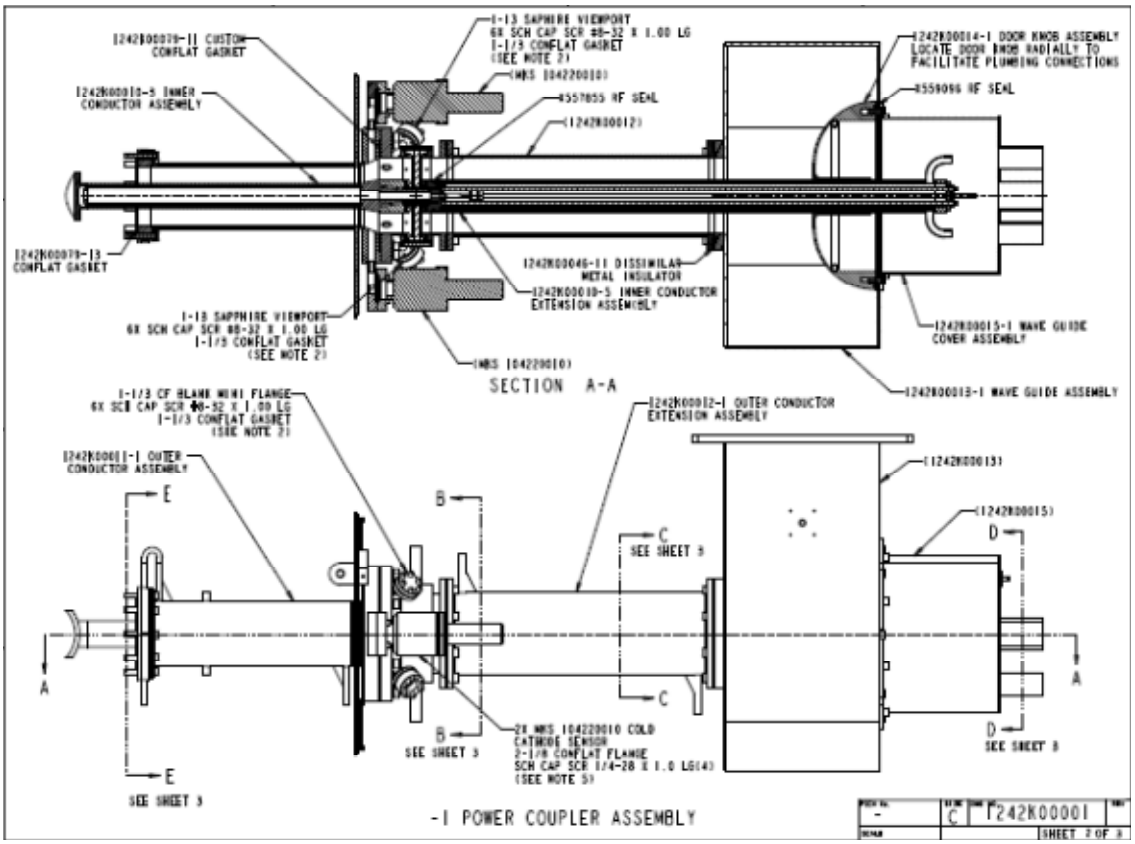

Figure 4.3: Schematic of the fundamental power coupler and doorknob transition.

4.2. Higher-Order Modes in the Gun Cavity

From the very beginning, the gun cavity was designed to minimize higher-order modes and to allow all but the lowest frequency modes to propagate out of the cavity. Nonetheless, high-current along with high-bunch charge operation will dissipate a large amount of HOM power.

The loss factor for the gun has been calculated to be ~0.7 V/pC (see equation 2.1), and the total HOM power dissipated is approximately 0.5 kW for a 500 mA beam current and a 1.4 nC bunch charge [7]. This power must be dissipated outside of the cryogenic environment, and, to this end, a ferrite beampipe absorber shall be placed downstream of the gun in the warm section of the accelerator. The design for this absorber is discussed in the next chapter. An important feature of this absorber is that it can only absorb modes that are above the 2.2 GHz cutoff frequency of the beampipe. This leads to a range of modes that can potentially be uncoupled or trapped within the cavity.

Since modes below the cutoff frequency do not propagate down the beampipe, they are impervious to the power dissipation afforded by a beampipe absorber. Nonetheless, we seek a solution for damping these modes as well. The fundamental power couplers (FPCs) offer a possibility here and they are in close proximity to the cavity, and therefore, it is likely that they may offer a solution for damping of the modes below the beampipe cutoff frequency. This study endeavored to determine the feasibility of damping using the fundamental power couplers and understand the design details that might be important in considering this avenue for damping.

The FPCs are inserted into the FPC ports on the cavity as shown in Figure 4.2, and a transition from coaxial probe to waveguide via a doorknob transition as shown in Figure 4.3 connects the FPCs to a 1 MW klystron which provides power to the system. A circulator is included in the system to provide protection from power reflections from the gun, and reflected energy is directed to a water-cooled absorber.

For effective HOM damping, the FPCs must couple to the higher-order modes of interest and, in this arrangement, direct those modes away from the gun, through the circulator, and to the energy absorber. The question posed by this study was: Do the FPCs provide any damping of the HOMs in the cavity? Subsequent sections will set out to answer this question through simulation and measurement.

4.3. Simulation Studies

To explore the spectrum of HOMs in the gun cavity, a series of simulations was conducted using the Microwave Studio software application. The models used for the simulation are based on a model constructed by R. Calaga for the design of the gun cavity [12], and a schematic showing the basic dimensions of the models is given in Figure 4.4.

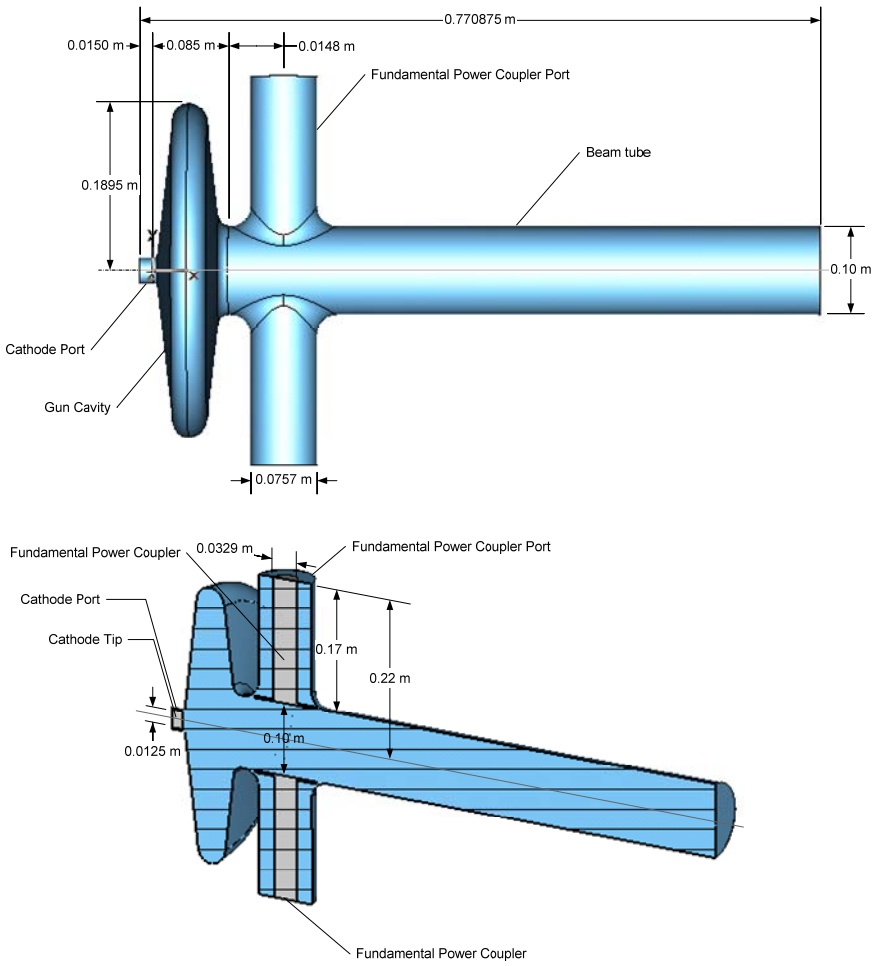

Figure 4.4: Schematics of models used for this study including dimensions.

The aim of the modeling efforts was twofold: first, to determine the higher-order modes of the gun cavity, and particularly to determine the monopole and dipole modes of the cavity since these modes are likely to have the most destabilizing effects on the beam. Monopole modes in the cavity lead to energy loss in the beam while dipole modes lead to transverse forces that can deflect the beam from the optimum trajectory through the cavity and subsequent beampipe. The second was to separately determine the effects of the FPCs and the beamline ferrite absorber on the higher-order modes of the cavity. Thus, a variety of model configurations were simulated that addressed the modes of the bare cavity along with the mode spectrum when the couplers were added as well as the ferrite absorber.

For the bare cavity, only the beampipe was included in the calculation. No couplers were present. The length of the beampipe was determined by the space between the cavity iris and the planned position of the ferrite absorber in the actual accelerator. A schematic showing the placement of the ferrite absorber is shown in Figure 4.5. The end of the beampipe was simulated as a 'waveguide' port – a kind of port in Microwave Studio that amounts to a perfectly terminated boundary without reflection. Electromagnetic waves incident on a waveguide port are perfectly absorbed at all frequencies without reflection.

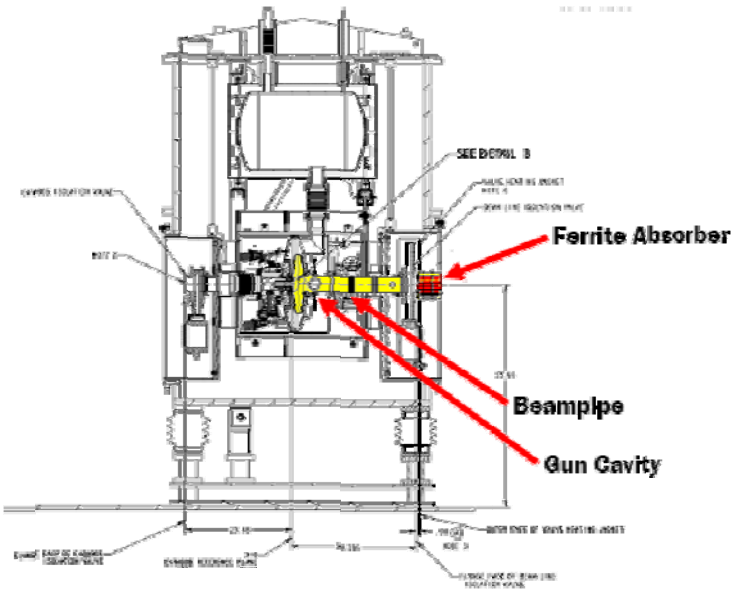

Figure 4.5: Schematic of gun inside of cryomodule with ferrite absorber attached.

To determine the modal frequencies of the cavity along with the Q-values, the eigenmode solver of the Microwave Studio application using the Jacobi-Davidson method (JDM) was employed within a frequency range from 600 MHz to 3 GHz. This range of frequencies was selected because it encompasses a set of modes likely to present some of the most destabilizing effects on the beam. For the model of the cavity and the beampipe, 357,600 mesh points were used in the simulation. The eigenmode solver calculates the resonant frequencies and corresponding electric and magnetic field patterns (eigenmodes) of the structure, and was well-suited to this study because the field configurations of each eigenmode were reported after the simulation run, allowing detailed study. Furthermore, the solver can be configured to provide both the external Q-value (Q_{ext}) of the specified ports in the structure as a post-processing step as well as

the instrinsic Q-value (Q_0) of the structure using conductivity values specified in advance. The conductivity of the walls of the structure was set to 2.5×10^9 S/m for calculation of the intrinsic Q-value. It should be noted that the real superconducting structure modeled in this study is only partially superconducting. A portion of the beampipe before the ferrite absorber is actually normal-conducting material. This was not considered for the purposes of this study. The fundamental power couplers are designed for very strong coupling to the fundamental frequency with $Q_{ext} \sim 4 - 5 \times 10^4$. Several options of electrical and magnetic coupling were considered, and a coaxial coupler with a curved tip, conformal with the beampipe radius ("pringle"-shape) was found to be an effective choice [7]. The pringle shape (originally designed for the Cornell ERL injector [26]) maximizes the coupling while minimizing wakefield effects.

For the purposes of these studies, we define the Q_{ext} in the usual manner:

$$Q_{ext} = \frac{\omega U}{P_e} \tag{4.1}$$

where P_e is the power dissipated through a port in the cavity. Here, we shall take the P_e to include any and all ports through which power may leave the structure. Then, in the case of a terminated beampipe, we shall take P_e to be the power that leaves the structure via the beampipe termination. A $Q_{ext\ (beampipe)}$ may be defined such that

$$Q_{ext\ (beampipe)} = \frac{\omega U}{P_{e\ (beampipe)}} \tag{4.2}$$

and similarly, a $Q_{ext\ (FPCs)}$,

$$Q_{ext\ (FPCs)} = \frac{\omega U}{P_{e\ (FPCs)}}. \tag{4.3}$$

For terminations on both the beampipe and the FPCs, we take P_e to be the sum of the power that leaves the structure via the beampipe termination and the termination of FPCs. Then,

$$P_{e\ (beampipe+FPCs)} = P_{beampipe} + P_{FPCs} \tag{4.4}$$

and,

$$Q_{ext\ (beampipe+FPCs)} = \frac{\omega U}{P_{e\ (beampipe+FPCs)}}. \quad 4.5$$

Thus, if the value of the Q_{ext} obtained from the mode with the terminated beampipe and shorted couplers is equal to that obtained from the fully-terminated model, then the power flowing through the FPCs is zero, and the FPCs do not couple to the mode.

The loaded Q-value, Q_L, may be expressed as

$$\frac{1}{Q_L} = \frac{1}{Q_0} + \frac{1}{Q_{ext}}. \quad 4.6$$

The Q_L-value, in effect, takes into account the intrinsic loss mechanisms (wall losses) as well as extrinsic loss mechanisms (losses through ports). This study compares both the Q_{ext} and the Q_L to determine the effect of the FPCs on the cavity modes.

In addition to the calculation of the external and intrinsic Q-values, the model also calculated the shunt impedances (R/Q) for each mode as a post-processing step. All of these values were tabulated for compared for both monopole and dipole modes.

4.3.1. Monopole Modes

The results obtained from each of the models for monopole modes are shown in Figure 4.6 and Figure 4.7. The results are also tabulated in Table 4.2 and Table 4.3. The results show that a significant difference in the Q_{ext} of the modes below 2.25 GHz between the first (beampipe termination and no FPCs) and second (terminated beampipe and FPCs) models. The second model shows a significantly lower Q_{ext} for modes that have counterparts in the first model. This behavior is echoed in the Q_L values. The Q-values clearly suggest that the FPCs couple strongly to these modes and tend to damp them by orders of magnitude. It should be noted that additional monopole modes appear in the second model that do not have a counterpart in the first model, and these modes tend to have peak fields in the beampipe and coupler ports. By 2.25 GHz, the damping effect of the FPCs diminishes, and, above this frequency, no damping due to the FPCs is observed.

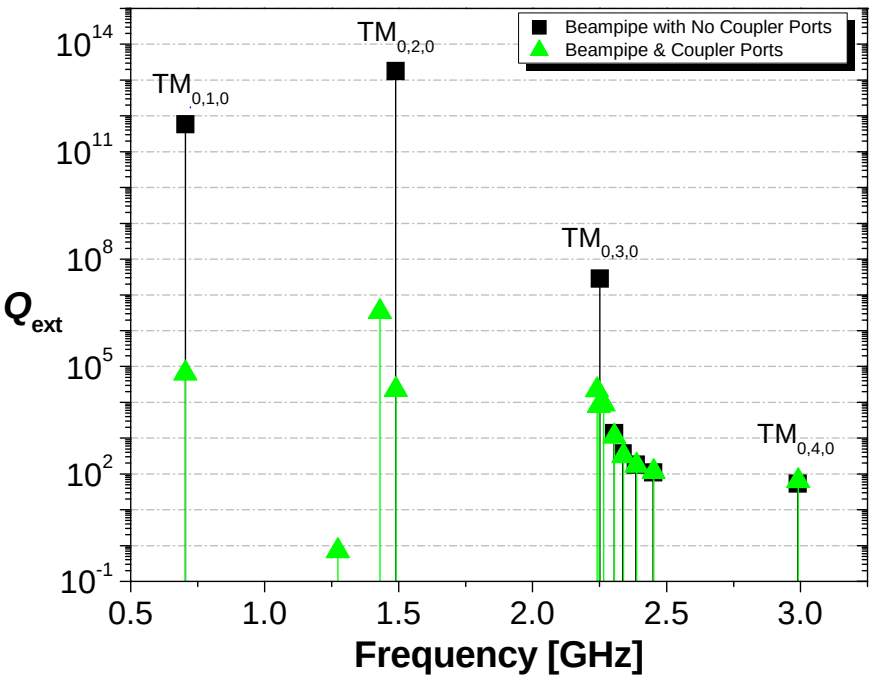

Figure 4.6: Plot of Q_{ext} for monopole modes from models with terminated beampipe only, terminated beampipe and shorted FPCs, and terminated beampipe and FPCs with well-defined cavity modes indicated.

Several factors appear to be at work to cause the observed coupling and the resulting damping effect. First, the cutoff frequency for the TM_{01} mode in the beampipe is 2.26 GHz. Thus, in the first model, the modes below this frequency simply do not propogate effectively through the beampipe. The terminated beampipe does little to mitigate the situation since these modes are highly attenuated at the location of termination due to cutoff. However, when the FPCs are included, energy flows out of the FPC ports and propagates away from the cavity, accounting for the greatly reduced Q_{ext} of these modes.

Above 2.26 GHz energy now propagates along the beampipe, significantly lowering the Q_{ext}. The substantial effect of the beampipe is evident in the observation that the Q_{ext} of the same model for modes below 2.26 GHz. However, when the FPCs are added, the change in Q_{ext}, while substantial for the TM_{030} mode is smaller than that observed in the modes below 2.26 GHz. Much of the energy now flows along the beampipe, and the effect of opening the FPCs for these modes is relatively modest. For modes with frequencies above 2.26 GHz, no damping effect is evident due to the FPCs. At these frequencies, no power flows through the FPC ports.

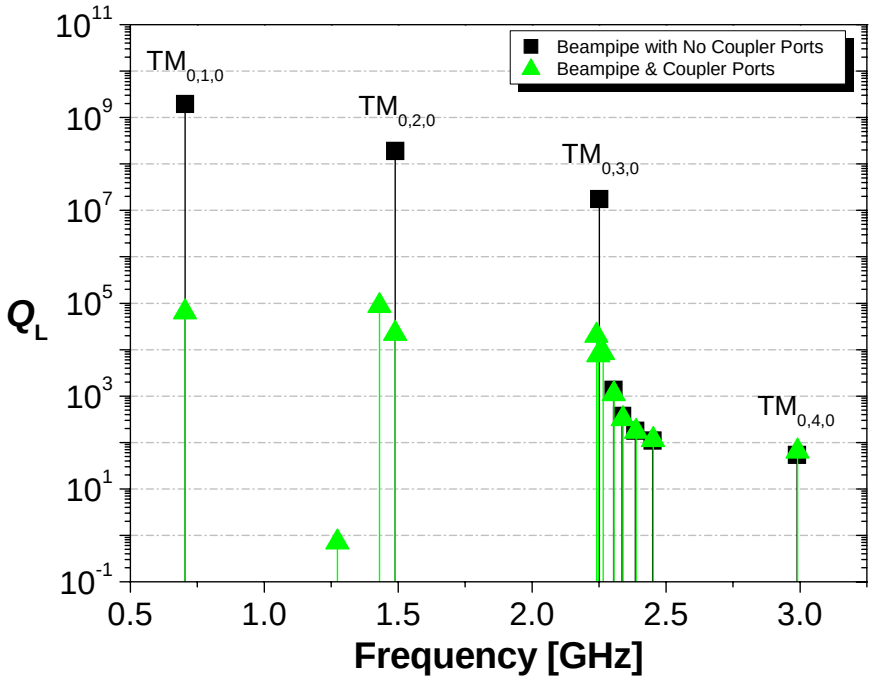

Figure 4.7: Plot of Q_L for monopole modes from models with terminated beampiupe only, terminated beampipe and shorted FPCs, and terminated beampipe and FPCs with well-defined cavity modes indicated.

Table 4.1 - Monopole Results for Model with Terminated Beampipe Only

Frequency [GHz]	Q_{ext}	Q_0	Q_L	R_a/Q_0 [Ω]
0.704098	5.78×10^{11}	1.96×10^{9}	1.95×10^{9}	96.06
1.488837	1.79×10^{13}	1.90×10^{8}	1.90×10^{8}	55.26
2.250506	2.86×10^{7}	4.56×10^{7}	1.76×10^{7}	10.82
2.304611	1.37×10^{3}	1.86×10^{9}	1.37×10^{3}	0.06
2.335711	3.73×10^{2}	8.16×10^{8}	3.73×10^{2}	1.77
2.384878	1.80×10^{2}	5.93×10^{8}	1.80×10^{2}	1.18
2.450401	1.10×10^{2}	4.56×10^{8}	1.10×10^{2}	0.63
2.989171	5.38×10^{1}	2.59×10^{7}	5.38×10^{1}	6.69

Table 4.2 - Monopole Results for Model with Terminated Beampipe and Terminated FPCs

Frequency [GHz]	Q_{ext}	Q_0	Q_L	R_a/Q_0 [Ω]
0.704078	6.46×10^{4}	1.06×10^{8}	6.46×10^{4}	95.05
1.273260	7.09×10^{-1}	9.48×10^{4}	7.09×10^{-1}	3.03
1.430706	3.35×10^{6}	8.98×10^{4}	8.75×10^{4}	1.72
1.489349	2.23×10^{4}	2.02×10^{7}	2.23×10^{4}	55.74
1.854131	1.33×10^{8}	3.06×10^{5}	3.05×10^{5}	0.00
2.240247	2.19×10^{4}	2.55×10^{5}	2.02×10^{4}	3.01
2.247427	8.11×10^{3}	1.55×10^{5}	7.71×10^{3}	1.62
2.265361	8.76×10^{3}	3.32×10^{5}	8.54×10^{3}	7.86
2.305627	1.11×10^{3}	7.67×10^{6}	1.11×10^{3}	0.00
2.339008	3.20×10^{2}	3.10×10^{6}	3.20×10^{2}	1.26
2.388543	1.71×10^{2}	2.12×10^{6}	1.71×10^{2}	0.75
2.452104	1.14×10^{2}	2.18×10^{6}	1.14×10^{2}	0.60
2.976345	2.01×10^{2}	2.46×10^{6}	2.01×10^{2}	0.76
2.991377	6.41×10^{1}	3.28×10^{6}	6.41×10^{1}	7.67

4.3.2. Dipole Modes

The dipole modes show a pattern similar to the monopoles including the marked effect of including the FPCs. Note that, in the case of dipoles, now the orientation or polarization of the dipole must be taken into account. Figure 4.8 makes the orientations clear – the vertical polarization is taken to be the polarization in which the electric fields are rotated to line up with the FPC ports while the horizontal polarization is taken to be the vertical orientation rotated 90 degrees. Now, the centers of the FPCs are lined up with the nodes of the electric fields as shown in the figure. A plot of Q_{ext} and Q_L for the different models are shown in Figure 4.9 and Figure 4.10, and the data are tabulated in Table 4.3 and Table 4.5.

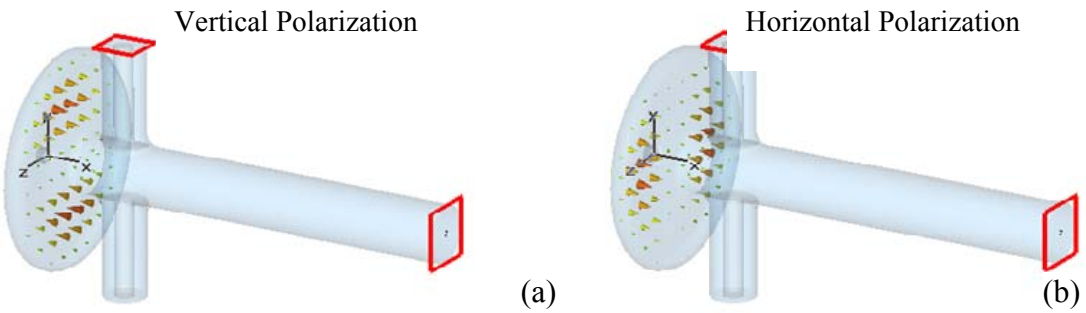

Figure 4.8: Orientation of electric fields for vertical and horizontal polarizations. Picture (a) shows the vertical orientation as defined in the study. Picture (b) shows the horizontal orientation. The red boxes show the locations of the waveguide ports.

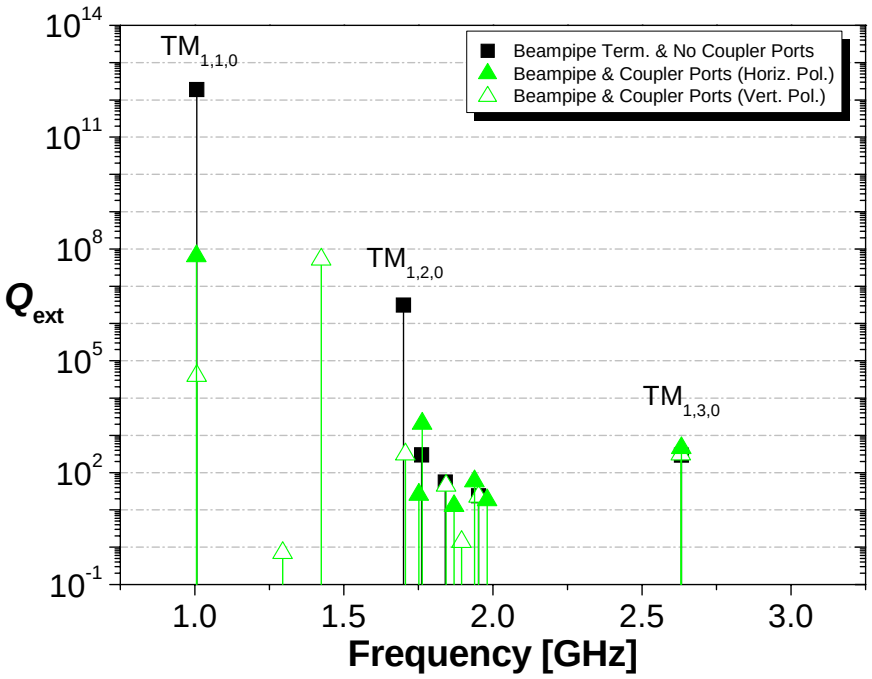

Figure 4.9: Plot of Q_{ext} for dipole modes from models with terminated beampipe only and terminated beampipe and FPCs for horizontally and vertically polarized modes with well-defined cavity modes indicated.

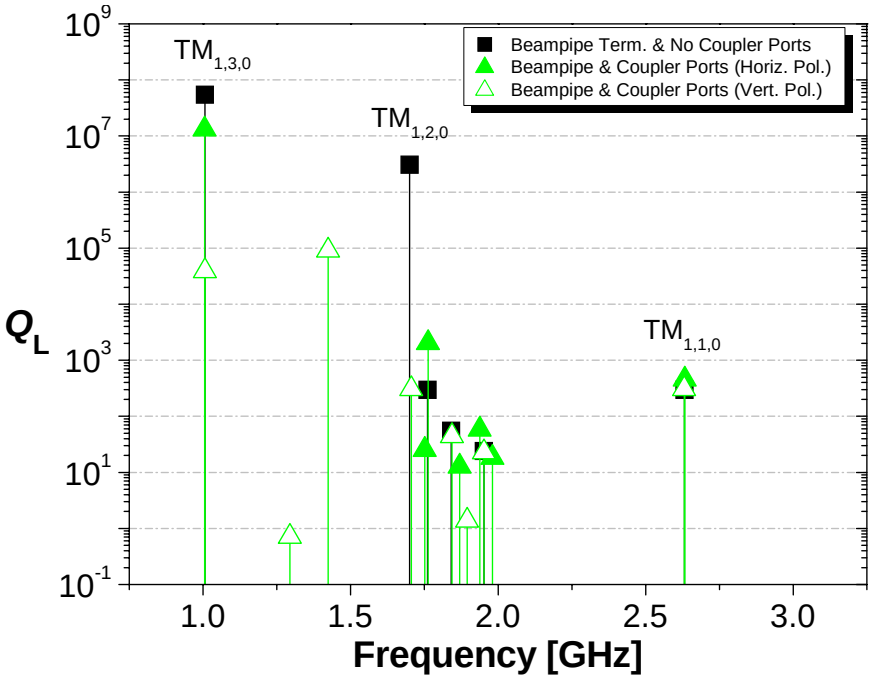

Figure 4.10: Plot of Q_{ext} for dipole modes from models with terminated beampipe only and terminated beampipe and FPCs for horizontally and vertically polarized modes.

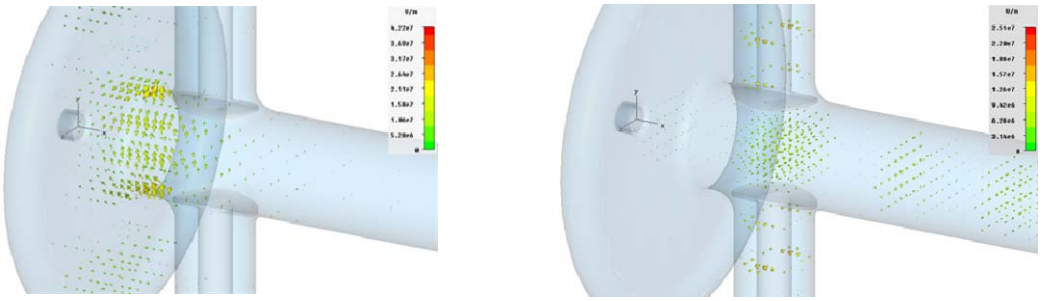

(a) (b)

Figure 4.11: Electric field distribution for dipole eigenmodes at ~1.7 GHz. In the vertical polarization (a), the field is strongly distorted by the presence of the FPCs. The horizontal polarization (b) shows relatively little field in the cavity and high gradient in the couplers and beampipe. These different field distributions likely account for the rather large difference in the two polarizations.

The spectra of these modes tend to be more complicated because modes of varying polarization enter whose peak fields are located in either the couplers or the beampipe or both in addition to the cavity. However, several distinct cavity modes may be identified that serve as markers for the evolution of various mode types. These cavity modes are indicated in the Q-value plots. For the TM_{110} and TM_{120} modes at ~1 and ~1.7 GHz respectively, the effect of the terminated FPCs,

once again, is to lower the Q_{ext} by several orders of magnitude for both the horizontally and vertically polarized dipoles. In the case of dipole modes, the cutoff frequency for the TM_{11} mode is 3.04 GHz while that of the TE_{11} mode is 1.75 GHz. The TM dipole mode does not propagate along the beampipe in the frequency range of the study; however, above 1.75 GHz, the TE dipole mode does propagate. In the case of modes below 1.75 GHz, the damping effect of the terminated FPCs is dramatic; however, the effect on the horizontally polarized dipole is about two orders of magnitude less substantial than on the vertically polarized case. This is to be expected since the couplers are oriented with the nodes of the field in the horizontally polarized dipole and therefore lose some coupling strength. Also note that the frequencies of the TM_{120} modes are different for the vertical and horizontal cases. In a completely azimuthally symmetric structure, the two polarizations would be expected to be completely degenerate. However, the presence of the FPCs lifts the degeneracy and forces the two modes apart by approximately 53 MHz, a substantial separation whose magnitude is not observed in the other two modes. The likely explanation for this split in frequencies is found in closely examining the field configurations of the vertical and horizontal polarizations. The horizontally polarized mode clearly does not interact as strongly with the couplers as the vertically polarized mode, and, as Figure 4.11 shows, the vertically polarized mode has a relatively large field concentration in the FPCs, which are capacitively coupled to the cavity. This field distribution likely lowers the resonant frequency of the mode based on simple resonant circuit considerations, i.e., $f \propto 1/\sqrt{LC}$. As C increases, the resonant frequency falls.

It is interesting to note that the vertical and horizontal polarizations of the TM_{120} mode have quite different Q_{ext}. Again, the likely explanation for this difference is that the FPCs, due to their orientation, impose a strong preference for the vertically polarized dipole.

The same damping effect enjoyed by the modes below 1.75 GHz is not evident above this frequency. Although many of these modes have Q_{ext} values many orders of magnitude less than the TM_{110} mode, the terminated FPCs do not contribute any significant damping to these modes except in several isolated cases including the vertically polarized TM_{130} mode and several others. Much of the power flows along the beampipe. Furthermore, isolated modes appear that have relatively large Q_{ext} and Q_L values, but, in all such cases the R_a/Q_0 value of these modes is very small.

Table 4.3 - Dipole Results for Model with Terminated Beampipe Only

Frequency [GHz]	Q_{ext}	Q_0	Q_L	R_a/Q_0 [Ω]
1.006489	1.88×10^{12}	5.44×10^{7}	5.44×10^{7}	47.19
1.659898	2.91×10^{12}	2.94×10^{11}	2.67×10^{11}	0.48
1.700017	3.14×10^{6}	1.91×10^{8}	3.09×10^{6}	7.48
1.760868	2.98×10^{2}	2.44×10^{12}	2.98×10^{2}	0.11
1.790648	8.74×10^{1}	3.18×10^{9}	8.74×10^{1}	0.77
1.840611	5.54×10^{1}	1.29×10^{8}	5.54×10^{1}	2.14
1.891841	3.90×10^{1}	2.26×10^{7}	3.90×10^{1}	3.41
1.952149	2.39×10^{1}	2.48×10^{7}	2.39×10^{1}	1.23
2.042539	2.58×10^{1}	4.17×10^{7}	2.58×10^{1}	0.35
2.152662	2.96×10^{1}	5.42×10^{7}	2.96×10^{1}	0.16
2.266501	2.02×10^{9}	1.31×10^{13}	2.02×10^{9}	0.01
2.275986	3.33×10^{1}	5.96×10^{7}	3.33×10^{1}	0.07
2.408629	3.69×10^{1}	5.80×10^{7}	3.69×10^{1}	0.03
2.505893	2.80×10^{11}	5.06×10^{10}	4.29×10^{10}	0.70
2.545960	4.21×10^{1}	4.09×10^{7}	4.21×10^{1}	0.03
2.632224	2.96×10^{2}	1.33×10^{7}	2.96×10^{2}	1.20
2.699088	4.86×10^{1}	5.39×10^{9}	4.86×10^{1}	0.21
2.834622	5.40×10^{1}	3.31×10^{9}	5.40×10^{1}	0.14
2.853277	1.81×10^{7}	1.81×10^{12}	1.81×10^{7}	0.00
2.953343	7.34×10^{1}	5.15×10^{7}	7.34×10^{1}	0.25

Table 4.4 - Dipole Results for Model with Terminated Beampipe and Terminated FPCs

Frequency [GHz]	Q_{ext}	Q_0	Q_L	R_a/Q_0 [Ω]	Polarization
1.005626	6.36×10^{7}	1.67×10^{7}	1.32×10^{7}	53.80	Horizontal
1.006379	3.93×10^{4}	4.11×10^{7}	3.93×10^{4}	53.95	Vertical
1.295012	7.08×10^{-1}	9.32×10^{4}	7.08×10^{-1}	6.28	Vertical
1.423896	5.27×10^{7}	9.15×10^{4}	9.14×10^{4}	2.30	Vertical
1.464873	7.14×10^{3}	1.33×10^{5}	6.78×10^{3}	0.50	Horizontal
1.659738	7.59×10^{7}	5.91×10^{10}	7.58×10^{7}	0.00	Vertical
1.659818	2.28×10^{8}	1.66×10^{10}	2.25×10^{8}	0.00	Horizontal
1.706061	3.08×10^{2}	3.56×10^{6}	3.08×10^{2}	11.32	Vertical
1.751874	2.55×10^{1}	1.49×10^{6}	2.55×10^{1}	11.58	Horizontal
1.760565	2.87×10^{2}	3.47×10^{8}	2.87×10^{2}	0.12	Vertical
1.762532	2.05×10^{3}	7.25×10^{6}	2.05×10^{3}	1.45	Horizontal
1.790843	7.73×10^{1}	2.72×10^{7}	7.73×10^{1}	0.69	Vertical
1.798518	2.06×10^{2}	3.51×10^{6}	2.06×10^{2}	0.61	Horizontal
1.842699	5.74×10^{1}	3.87×10^{5}	5.74×10^{1}	0.43	Horizontal
1.843514	4.44×10^{1}	6.91×10^{6}	4.44×10^{1}	1.93	Vertical
1.854652	3.36×10^{6}	3.04×10^{5}	2.78×10^{5}	0.00	Vertical
1.870080	1.28×10^{1}	1.79×10^{6}	1.28×10^{1}	1.67	Horizontal
1.895016	1.39×10^{0}	4.94×10^{6}	1.39×10^{0}	5.52	Vertical
1.938449	5.86×10^{1}	2.50×10^{6}	5.86×10^{1}	5.46	Horizontal
1.951747	2.29×10^{1}	1.17×10^{7}	2.29×10^{1}	2.56	Vertical
1.980521	1.83×10^{1}	7.47×10^{5}	1.83×10^{1}	2.35	Horizontal
2.044851	2.40×10^{1}	4.94×10^{6}	2.40×10^{1}	0.90	Vertical
2.074513	1.92×10^{1}	6.99×10^{5}	1.92×10^{1}	0.06	Horizontal
2.153565	2.78×10^{1}	1.63×10^{6}	2.78×10^{1}	0.38	Vertical
2.170313	1.70×10^{1}	5.28×10^{5}	1.70×10^{1}	0.08	Horizontal
2.246217	3.25×10^{1}	1.69×10^{5}	3.25×10^{1}	0.22	Vertical
2.255531	7.47×10^{9}	8.46×10^{5}	8.46×10^{5}	0.19	Horizontal
2.259919	6.60×10^{4}	2.08×10^{5}	5.01×10^{4}	0.02	Vertical
2.265939	8.79×10^{8}	1.36×10^{2}	8.78×10^{8}	0.00	Vertical
2.266123	2.04×10^{1}	1.15×10^{13}	2.04×10^{1}	0.00	Horizontal
2.295118	7.33×10^{12}	3.43×10^{5}	3.43×10^{5}	0.53	Vertical
2.373689	2.99×10^{1}	1.12×10^{6}	2.99×10^{1}	0.08	Horizontal

Frequency [GHz]	Q_{ext}	Q_0	Q_L	R_a/Q_0 [Ω]	Polarization
2.411559	3.72×10^{1}	3.66×10^{6}	3.72×10^{1}	0.19	Vertical
2.458228	2.13×10^{1}	2.02×10^{5}	2.13×10^{1}	0.24	Horizontal
2.505035	3.18×10^{6}	1.74×10^{9}	3.17×10^{6}	0.00	Vertical
2.505263	5.75×10^{4}	1.34×10^{8}	5.75×10^{4}	0.00	Horizontal
2.515283	3.50×10^{1}	1.22×10^{6}	3.50×10^{1}	0.07	Horizontal
2.546878	4.19×10^{1}	1.02×10^{7}	4.19×10^{1}	0.32	Vertical
2.630933	3.07×10^{2}	5.25×10^{6}	3.07×10^{2}	5.33	Vertical
2.632612	4.55×10^{2}	5.47×10^{6}	4.55×10^{2}	5.70	Horizontal
2.674400	3.96×10^{1}	1.47×10^{6}	3.96×10^{1}	0.60	Horizontal
2.699281	4.97×10^{1}	3.95×10^{6}	4.97×10^{1}	0.74	Vertical
2.798992	4.69×10^{1}	1.38×10^{5}	4.69×10^{1}	0.13	Vertical
2.827902	4.42×10^{1}	3.17×10^{6}	4.42×10^{1}	0.33	Horizontal
2.851014	2.78×10^{7}	4.10×10^{5}	4.04×10^{5}	0.32	Vertical
2.852069	8.92×10^{3}	4.24×10^{8}	8.92×10^{3}	0.00	Vertical
2.852589	9.20×10^{7}	5.60×10^{11}	9.20×10^{7}	0.00	Horizontal
2.876726	3.05×10^{1}	1.90×10^{5}	3.05×10^{1}	0.04	Vertical
2.901044	1.81×10^{2}	3.97×10^{5}	1.81×10^{2}	0.95	Horizontal
2.956000	7.36×10^{1}	5.30×10^{6}	7.36×10^{1}	0.79	Vertical
2.958865	1.43×10^{1}	1.85×10^{5}	1.43×10^{1}	0.18	Horizontal
2.973562	5.61×10^{3}	1.92×10^{7}	5.61×10^{3}	0.00	Horizontal
2.973760	1.07×10^{4}	8.08×10^{7}	1.07×10^{4}	0.00	Vertical

To summarize, the case of dipole modes is similar to that of monopoles in that the termination of the FPCs has a significant damping effect on lower frequency modes. As the mode frequency increases beyond 1.75 GHz, the damping effect of the FPCs diminishes substantially.

4.3.3. Simulation of the FPC Doorknob Transition

For effective HOM damping, the transition from the coaxial FPC to the waveguide that feeds the couplers from the 1 MW klystron must allow the energy from the HOMs to flow through the transition back to a circulator that ultimately shunts the power to the dump. The transition from the coaxial FPC coupler to the waveguide is a "doorknob"-type transition designed by Advanced

Energy Systems. The RF characteristics of the transition must be taken into account in order to understand how the FPCs will perform. Since the actual transition device was not available for this study, the transition was simulated using the frequency solver of Microwave Studio. The model appears in Figure 4.12 and Figure 4.13, and the results are plotted in Figure 4.14.

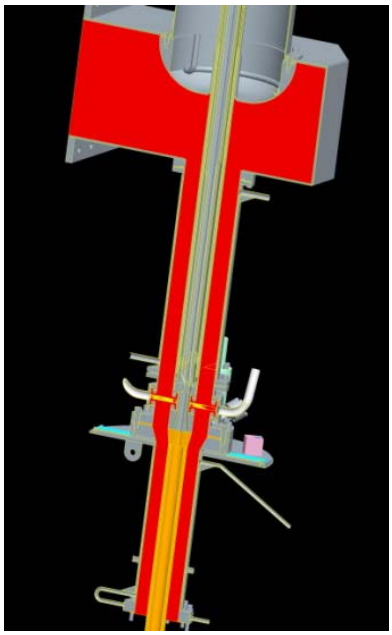

Figure 4.12: Schematic of FPC with "doorknob" transition from coaxial FPC to waveguide feed from klystron. RF space is indicated in red.

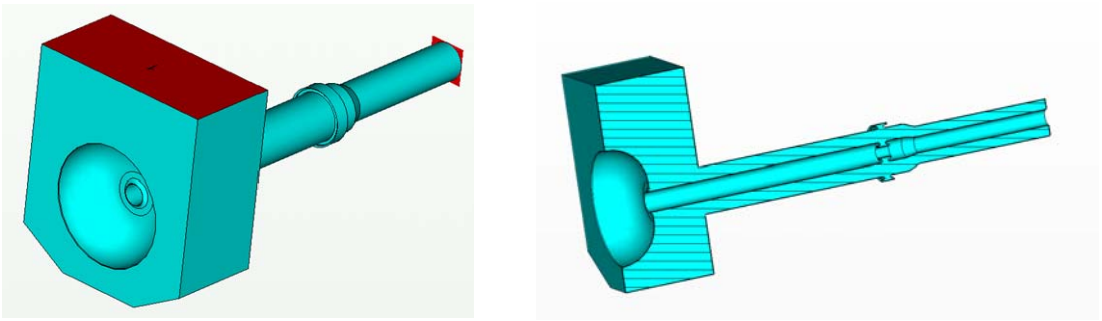

Figure 4.13: Microwave Studio model of doorknob transition. Red rectangles indicate ports (left). Note that port 1 is on the waveguide side of the transition. Right picture shows cutaway view.

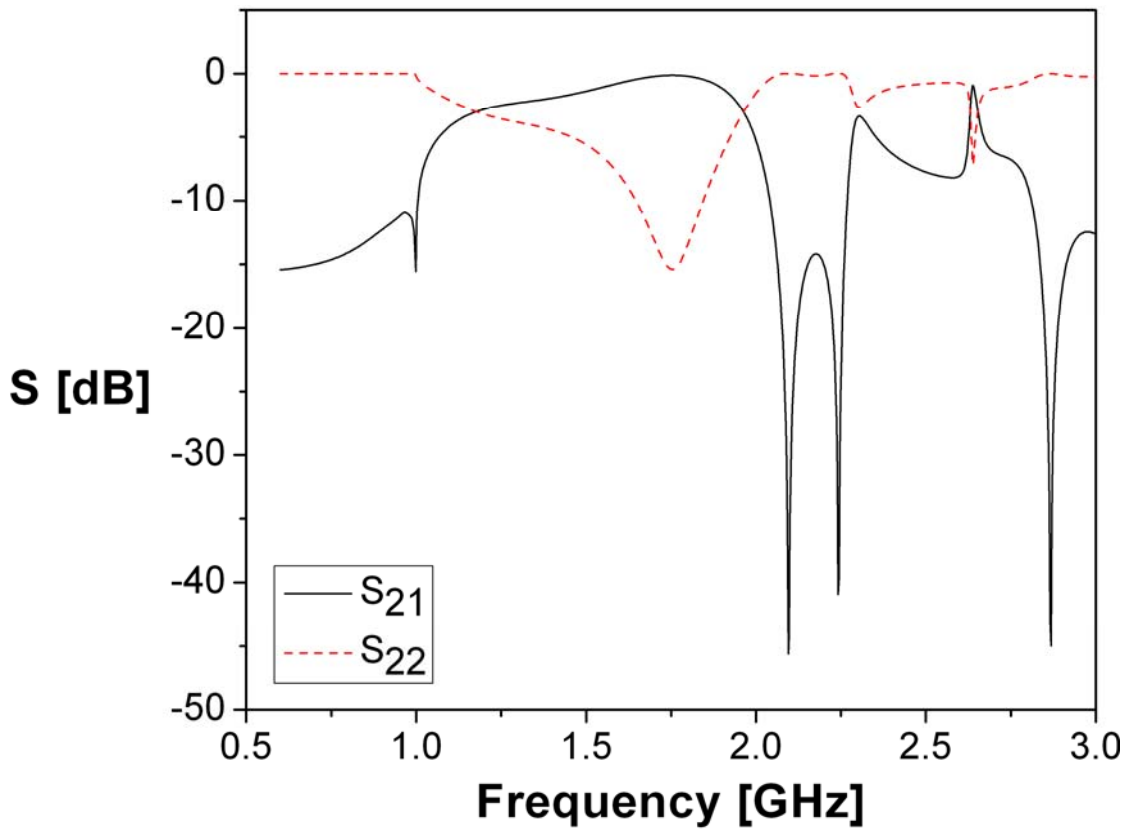

Figure 4.14: S_{21} (black) and S_{22} (red) simulation results for doorknob transition. See Figure 4.13 for labeling of ports.

The results indicate that signal transmission at low frequencies below 1 GHz is rather low (< -10 dB), but increases sharply abve 1 GHz. Transmission falls off again rapidly around 2 GHz. The S_{22} signal shows full reflection up to 1 GHz and then, as expected, reflection decreases above 1 GHz, allowing signal to flow out of the transition. Taken together, this behavior would seem to support the necessary coupling suggested by the HOM simulation data above. *Q*-values indicate that maximum damping of HOMs occurs in a range from 1 GHz up to 2.25 GHz. Thus, some damping for most modes below cutoff frequencies can be expected except for the mono-pole mode at 2.25 GHz. However, it remains to simulate the mode of the cavity joined to the waveguide transition.

4.3.4. Conclusions

The simulations indicate that many of these modes are strongly coupled to the FPCs with reductions in the Q_{ext} and Q_L of the gun cavity of several orders of magnitude. The damping effect of the FPCs diminishes with increasing frequency, and, for the highest frequencies studied, for both monopole and dipole modes, no damping effect of the FPCs was observed in simulation. The study also showed that few if any of these HOMs are likely to be excited by the beam since their frequencies do not coincide with the beam harmonics based on the high-current operating parameters assumed at the outset of the study. Those modes that are in close proximity to the beam harmonics show rather low R/Q values and are unlikely to be significant.

Furthermore, the simulations suggest that the doorknob transition will allow for the damping observed in the FPC simulations. This transmission is particularly effective between 1 GHz and 2 GHz and falls off sharply outside of this range.

4.4. Cavity Measurements

4.4.1. Method

Cavity measurements were carried out on the large-grain niobium cavity using "mock" fundamental power coupler probes that were developed to simulate the physical dimensions and impedance matching of the actual FPCs. These probes were designed from EIA-type couplers (RLA150-NF manufactured by Electronics Research, Inc.) with 50 Ω impedance. The connector itself is shown in Figure 4.15. An aluminum rod was attached to the "bullet" of the connector that had the same diameter as the inner conductor of the actual FPC. This was necessary so that when the mock probe was inserted into the FPC port of the gun cavity, the 50 Ω impedance of the arrangement was preserved. A rounded tip was also attached to the end of the probe similar to that of the actual FPC with the same radial dimensions and curvature. The entire mock probe is shown in Figure 4.16. Two such probes were inserted into the FPC ports of the gun in various arrangements as described below and clamped onto the flanges of the port as shown in Figure 4.17. In addition, a 10-inch length of beampipe with radius 5.08 cm was also attached to the cavity and closed (shorted) at the end.

Figure 4.15: EIA connector used for mock FPC.

Figure 4.16: Mock FPC probe showing coupler with inner conductor and "pringle" tip attached.

Figure 4.17: Mock FPC inserted into gun cavity. In this case, a 50-Ohm termination is attached to the FPC.

4.4.2. External Q Measurement

For measurements, a network analyzer was used to collect S_{21} data from the gun cavity and Q-values were extracted. Three basic configurations were used to collect the data: in the first configuration, the external Q of both FPCs was established and compared to the design value to determine how well the coupling of the mock FPCs corresponds to the design value of the actual couplers. In this measurement, an input coupler was inserted into the cathode port of the cavity and a pickup probe was inserted into the pickup port. The configuration of the ports is shown in Figure 4.18(a). The couplers were very weakly coupled to the cavity, and the intrinsic Q of the cavity was measured with all other ports closed (shorted). Then, the mock FPCs were inserted into the gun's FPC ports, and the loaded Q was measured as shown schematically in Figure 4.18(e). The external Q of the FPC can then be calculated from the following:

$$\frac{1}{Q_L} = \frac{1}{Q_0} + \frac{1}{Q_e} \tag{4.7}$$

then,

$$Q_e = \frac{Q_0 Q_L}{Q_0 - Q_L} \tag{4.8}$$

4.4.3. Damping Measurements

For other measurements, the cavity was excited from the cathode port and a pickup antenna was inserted in the pickup port. This configuration provided baseline measurement data about the cavity as well as a consistent means of stimulating the structure when the FPCs were inserted. The aim in these efforts was to measure the basic effect of the FPCs on the higher-order mode spectrum of the cavity. Most of the higher order modes of the cavity are evident in this configuration, and so it served as the most effective means of determining spectrum data. Another method used to stimulate the structure was to insert a probe into the cathode port and then use one of the FPCs as the pickup probe. By comparing this configuration to the situation in which both mock FPCs are inserted, and one of the FPCs is terminated in 50 Ω without changing the configuration of the stimulation and pickup probes (inserted in the cathode port and using one of the mock FPCs, respectively), the effect of the insertion of a single FPC into the cavity can be gauged while at the same time taking into account the frequency response characteristics

of the mock FPCs themselves. This method also allows changes in the physical geometry to be accounted for due to the insertion of the FPCs, although these changes are believed to be perturbative in nature, particularly at low frequency due to the attenuation of modes below the cutoff frequency of the beampipe. That is, modes at low frequency are localized to the cavity because they are sharply attenuated at the FPC ports at low frequency. The magnitude of this attenuation decreases as frequency increases and as the cutoff frequency of the beampipe is approached. These configurations are summarized schematically in Figure 4.18.

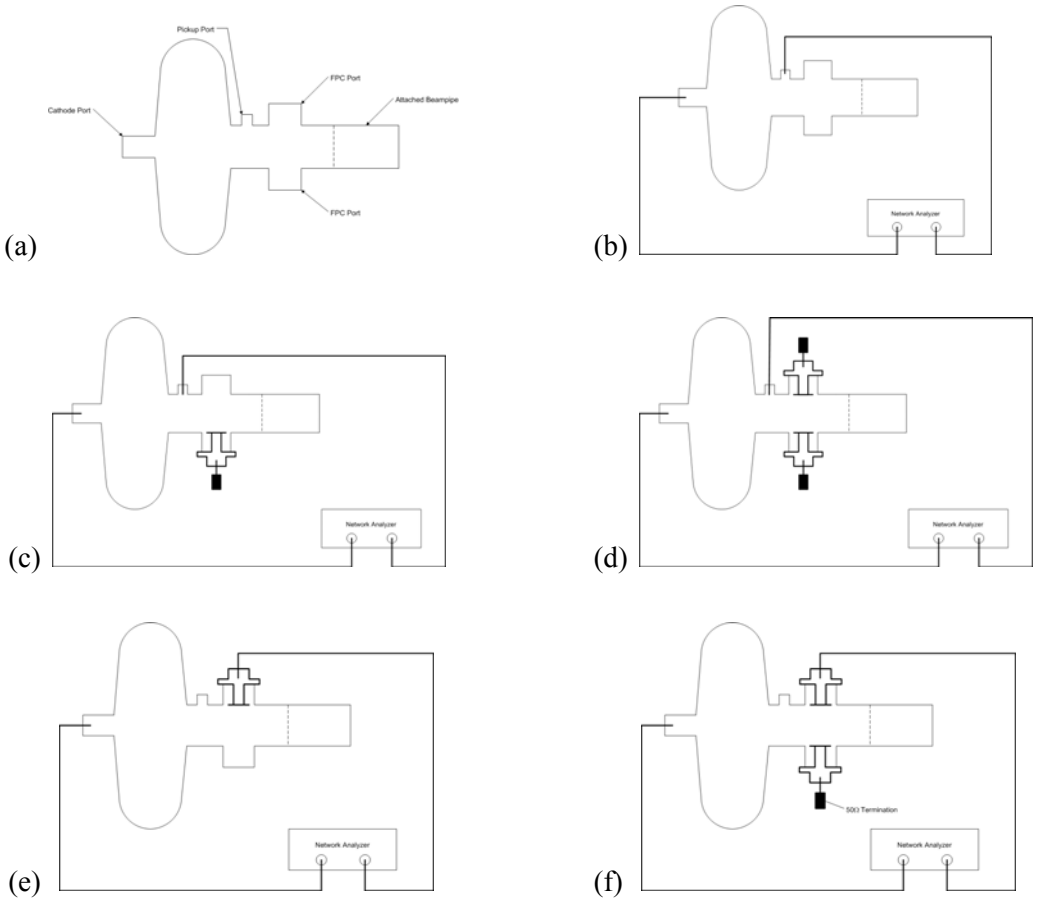

Figure 4.18: Schematic of stimulation configurations. In (a) the cavity ports are identified. In (b) the configuration for S_{21} measurement from cathode port to pickup port is depicted. In (c) measurement is from FPC port to FPC port. In (c) mock FPCs are inserted, and measurement is from FPC to FPC. In (e), a single FPC is inserted, and measurement is from FPC to FPC port. In (f), one of the FPCs is terminated in 50Ω, and measurement is from cathode port to FPC. For (e), a single mock FPC is inserted and stimulation is from cathode to FPC port. This serves as baseline measurement to compare to (e), in which a second mock FPC is inserted and terminated in 50 Ω.

For all of these measurements, the Q-values of the higher-order modes were classified to the extent possible, the Q-values were compared, and the coupling factor for each of these modes was calculated, providing a quantitative measure of the damping. Consider that the baseline Q-value, Q_b is expressed as

$$Q_b = \frac{\omega U}{P_e} \tag{4.9}$$

where ω is the frequency, U is the total energy, and P_e is the power escaping through any open port. Note that this definition does not distinguish between any ports in which energy may escape the structure. Then, we may define a damped Q-value, Q_d, such that

$$Q_d = \frac{\omega U}{P_d} \tag{4.10}$$

where P_d is the power escaping through any open port including the inserted FPCs. Note that for both expressions, it is assumed that the input coupler is weakly coupled to the cavity and thus energy escaping through the input coupler is negligible. Nonetheless, any energy escaping through the input coupler as well as other losses are taken into account by forming the coupling parameter:

$$\beta = \frac{Q_b}{Q_d} = \frac{P_d}{P_e} \tag{4.11}$$

Now, when $\beta < 1$, the FPCs are weakly coupled to a particular mode and the mode is essentially undamped. When $\beta > 1$, the FPCs are more strongly coupled to the mode, depending on the magnitude of β, and the mode is damped.

In a final set of measurements, both mock FPCs were inserted and the cavity was stimulated from the cathode port to the pickup port. S_{21} measurements were then conducted under three different conditions: Both FPCs were unterminated (open), both FPCs were shorted, and both FPCs were terminated in 50 Ω. Next, a method that is normally used to identify trapped and untrapped modes in a cavity can also be used to corroborate the coupling of the FPCs to higher-order modes. This technique involves the computation of the modes with two different boundary conditions at the FPC termination [27]: electric wall or short-circuited transmission line ($\hat{n} \times \vec{E} = 0$)

and magnetic wall or open-circuited transmission line ($\hat{n} \times \vec{E} = 0$). The influence of the boundary conditions on the frequency can be used to infer the coupling of the mode to the FPCs via the following expressions:

$$\kappa = 2\frac{|f_{mag} - f_{elec}|}{f_{mag} + f_{elec}} \tag{4.12}$$

$$\frac{1}{\kappa} \approx \begin{cases} 1 : coupled \\ \infty : uncoupled \end{cases} \tag{4.13}$$

Thus, when $1/\kappa \approx 1$, the FPCs couple to the mode and the mode is damped by the FPCs. When $1/\kappa \approx \infty$, the mode is weakly coupled or uncoupled to the mode, depending on the magnitude of $1/\kappa$, which, in turn, is a reflection of the damping.

4.4.4. Results

4.4.4.1. External *Q* of Mock FPCs

In this measurement, an intrinsic Q value of 5,817 for the fundamental mode was obtained. When both FPCs were inserted into the cavity, the loaded Q was found to be 5,456. Using equation 4.9, an external Q value of 8.79×10^4 was calculated. The design value, as given by Calaga et al [7], is $4 - 5 \times 10^4$, so the coupling of the mock FPCs to the cavity appears to be somewhat weaker than the design value. The likely causes for the weaker coupling include impedance mismatch and geometrical imperfections relative to the actual coupler design on which the design external Q is based. With regard to impedance mismatch, the virtue of the mock FPC design is that it is based on an EIA connector that easily mates with the center conductors whose dimensions are critical to assure impedance matching since this portion is inserted into the FPC port. However, the EIA coupler diameter does not match the diameter of the port exactly and may introduce errors if the coupler is not perfectly centered on the port. Every effort was taken to ensure that the coupler was centered. Furthermore, the connector has a very small grove around its inside surface, as shown in Figure 4.15, and this may contribute to the mismatch although the impact of this detail is believed to be small. The more significant sources of error likely stem from imperfections in the dimensions of the inner conductor and its orientation in the

FPC port. In addition, the orientation of the pringle relative to the beampipe is important and may have a significant impact on the measurement. In setting up the experiment, it was found that twisting the pringle from conformal alignment with the beampipe could result in change in Q of several hundred. Thus, this alignment is important, and misalignment could contribute to changes in coupling.

4.4.4.2. Damping Measurements

For the damping measurement, the attempt, as explained above, was to measure the coupling of the various higher-order modes to the mock FPCs using a variety of configurations. In the first configuration, as described above, the cavity was stimulated using input and pickup couplers, and the Q value in this baseline arrangement was compared to the same arrangement in which both couplers, terminated in 50 Ω, was inserted and the Q value was once again obtained. From the Q-values, the change in power escaping the cavity was calculated by taking the ratio of the Q values as expressed in Eq. 4.11. Table 4.5 shows the results of the measurement and the calculation of the coupling below. The Q-values are also plotted in Figure 4.19. For the table, an attempt was made to identify the mode type (monopole or dipole) where the frequency match based on simulation results is clear. For many of the modes identified by type, neighboring unidentified modes are likely to be of similar type. The spectrum becomes more complicated at higher frequencies, and mode identification becomes more difficult. In addition, the table attempts to correlate resonance peaks that appear to be related on the same row. This correlation was gleaned from careful inspection of the S_{21} data as plotted in Figure 4.19. The spectrum becomes particularly intricate around 1.8 GHz, where it appears that significant frequency shifts occur when the FPCs are inserted. A plot of this data is included in Figure 4.21.

This is consistent with the observation that the coupling of HOMs to the FPCs increases somewhat with increasing frequency. This is to be expected since, as the frequency approaches the cutoff frequency, more field is present at the location of the couplers, and therefore, the interaction with the FPCs is stronger. At frequencies below the cutoff, the coupling appears to be modest but increases steadily up to the cutoff value around 2.5 GHz. So, for frequencies near the fundamental, the effect of the FPCs on HOM mode damping appears to be rather weak, but increases as the mode frequency increases. It is also interesting to note that the majority of fre-

quencies that could be identified in the spectrum are dipole modes and there seems to be significant coupling to at least one of the dipole mode polarizations in many cases and perhaps both in certain cases. It is important to note that the stimulation configuration may obscure the coupling to modes of varying polarization. For this reason, it is also useful to examine the results from the stimulation of the cavity using the FPCs themselves since this provides an alternate configuration that may change the polarization. Also, there are a number of modes that do not have appear to have an obvious corresponding mode in either configuration. These may be mode of the various ports, particularly the FPC ports as they are shorted and opened to allow insertion of the FPCs.

Table 4.5 - Measurement of Q-value and Couping for Baseline and Both FPCs Inserted

Baseline Cathode to Pickup		FPCs Inserted Cathode to Pickup		Mode Type	Coupling
Frequency [GHz]	Q	Frequency [GHz]	Q		
0.70318	5817	0.70317	5467	Monopole	1.06402
1.00821	4659	1.00816	4345	Dipole	1.07227
1.48744	5097	1.48728	4354	Monopole	1.17065
1.76329	6631	1.73114	2300	Dipole	2.88304
1.81000	1620	1.78104	561	--	2.88770
1.83477	1711	1.80645	--	--	--
1.87090	5111	1.84281	--	Dipole	--
--	--	1.87281	--	--	--
1.90679	4540	1.89238	1417	Dipole	3.20395
--	--	1.94410	1315	--	--
2.00779	939	--	--	--	--
2.13058	2844	--	--	--	--
2.15002	2441	2.14969	621	Dipole	3.93076
2.26883	1296	2.24969	3485	Dipole	0.37188
2.32625	--	2.31676	766	--	--
--	--	2.35049	871	--	--
2.40094	--	--	--	--	--
2.41188	802	2.41379	--	Dipole	--
2.41562	--	2.42144	--	Dipole	--
2.42469	--	2.42492	418	--	--
2.53544	1218	2.53343	1047	Dipole	1.16332
2.56996	3926	2.56525	2144	--	1.83116
2.58544	1700	--	--	--	--
2.67551	5979	2.66788	1255	Dipole	4.76414

Baseline Cathode to Pickup		FPCs Inserted Cathode to Pickup		Mode Type	Coupling
Frequency [GHz]	*Q*	Frequency [GHz]	*Q*		
2.73796	1621	2.75673	468	--	3.46368
2.76977	7585	2.76846	3613	--	2.09936
2.79338	1777	--	--	--	--
2.81337	2093	--	--	--	--
2.83865	2394	--	--	Dipole	--
2.86095	9126	2.86078	5232	Dipole	1.74427
2.86931	5487	2.90752	844	--	6.50118
2.92425	2407	--	--	--	--
2.94540	2215	--	--	--	--
2.95567	4237	--	--	Dipole	--
2.96535	2681	2.97081	766	--	3.5
2.98734	2951	--	--	--	--
3.01224	8914	3.01003	1962	--	4.54332
3.05733	4637	3.05824	3104	--	1.49388
3.07474	1901	--	--	--	--

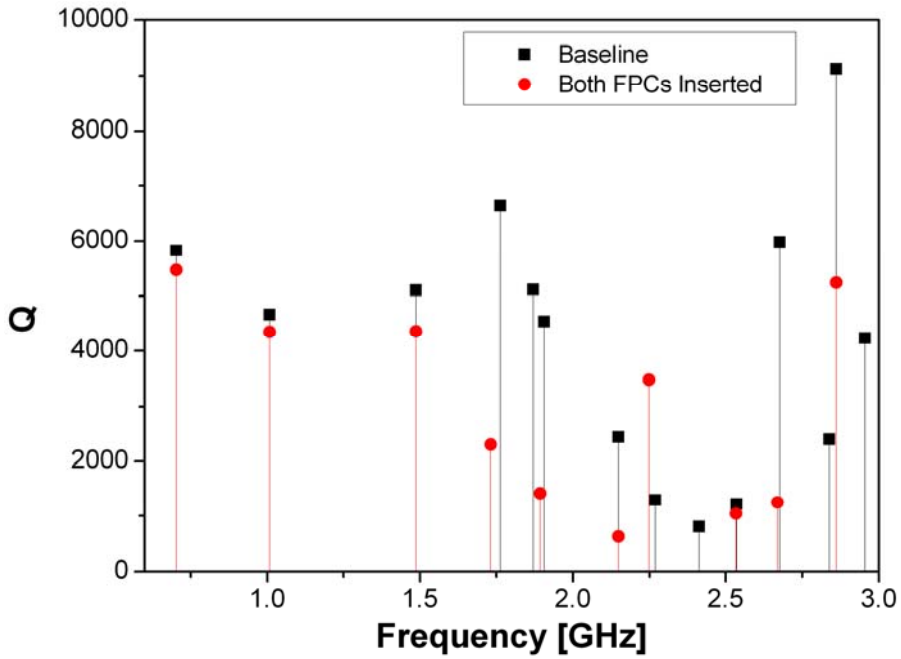

Figure 4.19: Measurement of *Q*-value for baseline with both FPCs inserted for selected monopole and dipole modes.

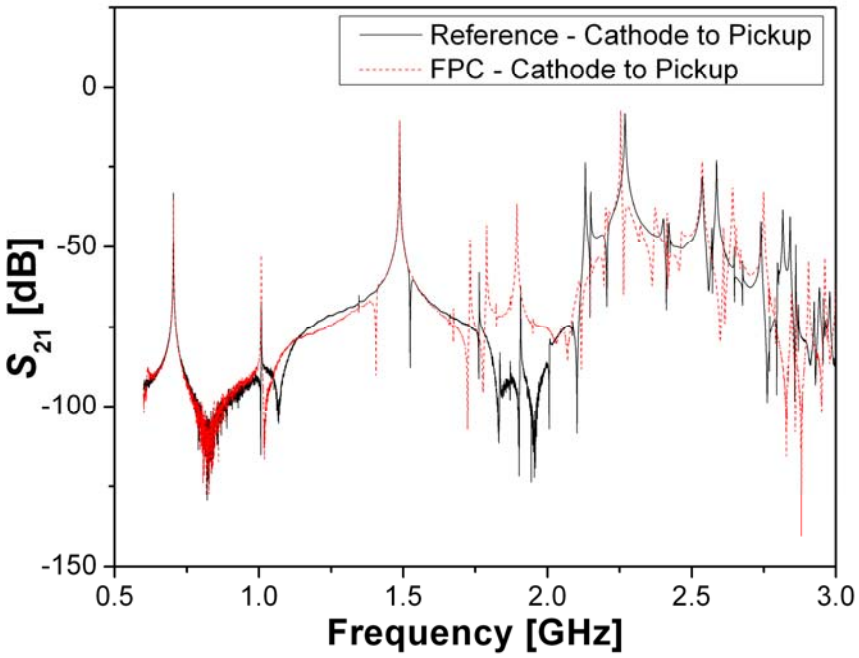

Figure 4.20: S_{21} measurements for baseline (reference) configuration and with both FPCs inserted. Stimulation is from the cathode port to the pickup port of the cavity.

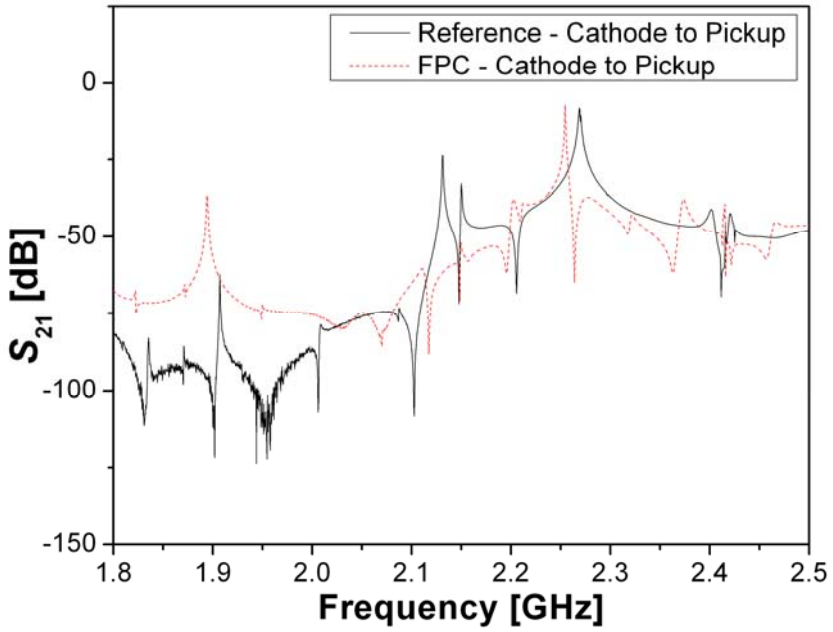

Figure 4.21: Comparison of S_{21} measurements for baseline (reference) configuration and with FPCs inserted between 1.8 GHz and 2.5 GHz. Structure of spectrum shows significant frequency shifts when FPCs are inserted due to strong coupling of FPCs to the fields in this frequency regime.

4.4.4.3. Cathode to FPC Measurements

In these measurements, the cathode port was used to insert the input coupler and a mock FPC was used as the pickup coupler. Now, the geometry and frequency response characteristics of the mock FPC form the baseline configuration. This, in turn, was compared to the situation in which the second mock FPC was inserted into the port, and the loaded Q-value of this arrangement was compared to the baseline arrangement. The results are tabulated in Table 4.6 and plotted as both Q-values in Figure 4.22, and as S_{21} data in Figure 4.23. Here, it appears that for certain modes, when the second FPC is added to the cavity, the change in Q-value between the two configurations is rather modest. For these modes, the coupling appears to be rather weak. For other modes, a significant change in Q-value is evident, indicating strong coupling. The external Q-value for a single FPC for the fundamental mode is 6.58×10^5. When the external Q for both FPCs is calculated for this configuration, the value is 1.46×10^5.

Table 4.6 – Q-values and Coupling for a Single FPC Inserted and for Both FPCs Inserted

Cathode to Single FPC		Cathode to FPC Both FPCs Inserted		Mode Type	Coupling
Frequency [GHz]	Q	Frequency [GHz]	Q		
0.70316	5766	0.70318	5594	Monopole	1.03075
1.00967	5885	1.00968	4838	Dipole	1.21641
1.48739	5764	1.48729	5062	Monopole	1.13868
1.67602	274	1.67719	185	--	1.48108
1.72083	1812	1.73049	3988	--	0.45436
--	--	1.78619	597	--	
1.80291	711	1.80431	599	--	1.18698
1.82276	919	--	--	--	--
1.86002	2079	--	--	--	--
1.87098	678	1.87181	360	Dipole	1.88333
--	--	1.89290	4084	--	--
1.91605	3604	--	--	Dipole	--
--	--	1.94109	667	--	--
2.02368	548	--	--	--	--
--	--	2.08196	137	--	--
--	--	2.14965	4163	--	--
2.21500	--	--	--	--	--

Cathode to Single FPC		Cathode to FPC Both FPCs Inserted		Mode Type	Coupling
Frequency [GHz]	*Q*	Frequency [GHz]	*Q*		
2.25878	395	2.25152	2726	--	0.14490
2.28559	833	--	--	--	--
2.32830	947	2.31867	1296	--	0.73071
--	--	2.35586	833	--	--
2.40480	1705	--	--	--	--
2.41497	2515	2.41447	1498	Dipole	1.67890
--	--	2.42730	791	--	--
--	--	2.43854	458	--	--
2.44234	2102	2.44355	3618	--	0.58098
2.53356	1943	2.53304	1831	Dipole	1.06117
2.53824	2157	--	--	Dipole	--
2.54349	1405	--	--	--	--
2.58576	1749	2.57304	2036	--	0.85904
2.61812	--	2.62023	3752	--	--
2.63999	5155	--	--	--	--
--	--	2.65782	5420	--	--
2.66720	580	--	--	Dipole	--
--	--	2.68257	1593	--	--
2.72660	1233	--	--	--	--
--	--	2.75641	396	--	--
2.77109	1949	--	--	--	--
2.77848	578	--	--	--	--
--	--	2.78856	880	--	--
2.80634	829	--	--	--	--
2.85973	6418	--	--	Dipole	--
2.86093	6234	2.86085	5228	--	--
2.86479	6308	--	--	--	--
2.91573	656	2.90798	686	--	0.95627
2.95785	1211	2.97146	764	Dipole	1.58508
2.97257	961	--	--	--	--
3.00759	688	3.00983	722	--	0.95291
3.01855	273	--	--	--	--
3.05778	3543	3.05920	2233	--	1.58666
3.08639	2700	3.07910	2693	--	1.00260
3.10427	1471	3.10651	1253	--	1.17398

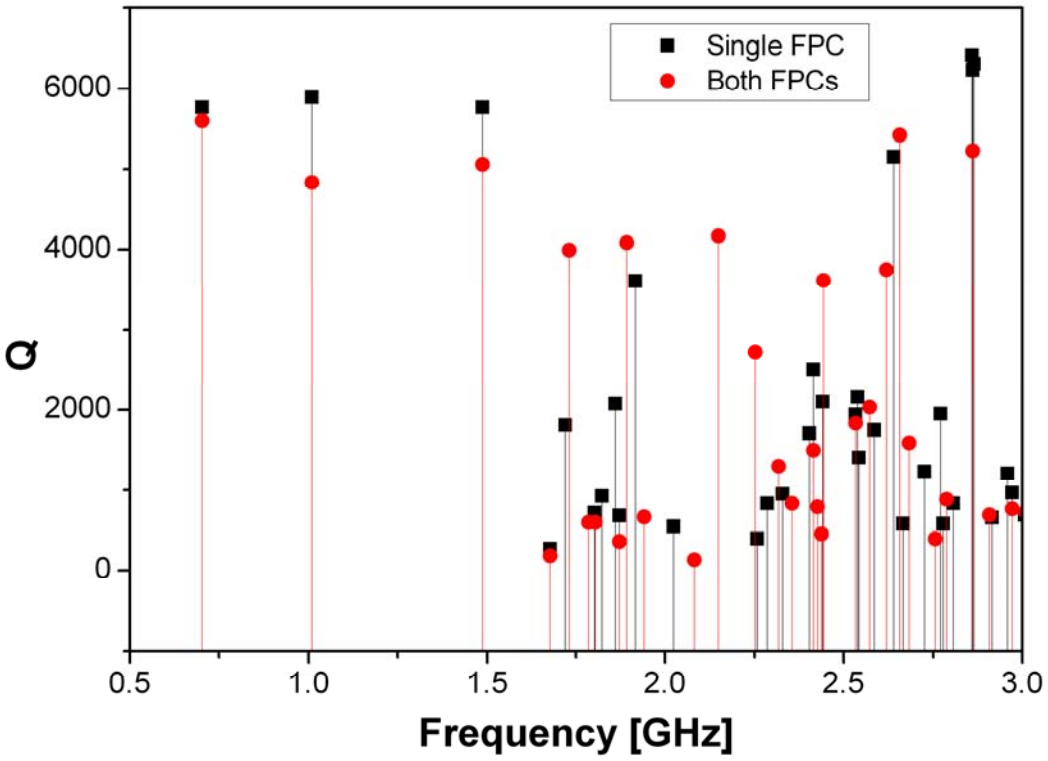

Figure 4.22: Comparison of *Q*-values for case of single FPC inserted and both FPCs inserted.

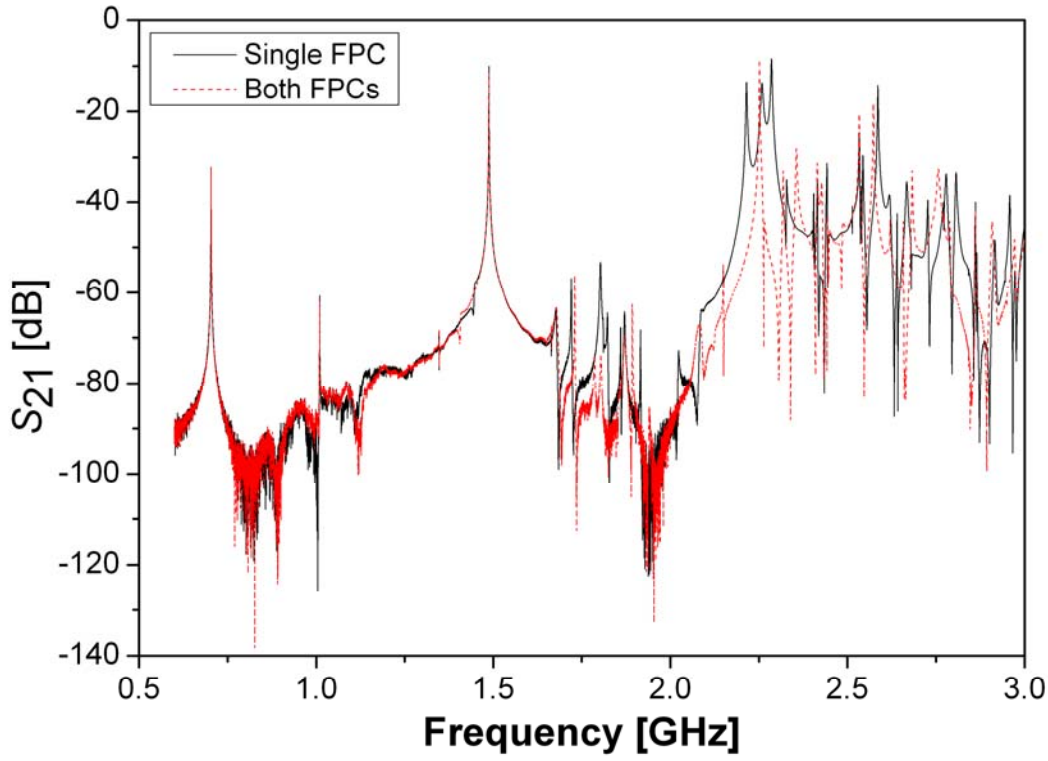

Figure 4.23: S_{21} measurements for configuration with single FPC and both FPCs inserted.

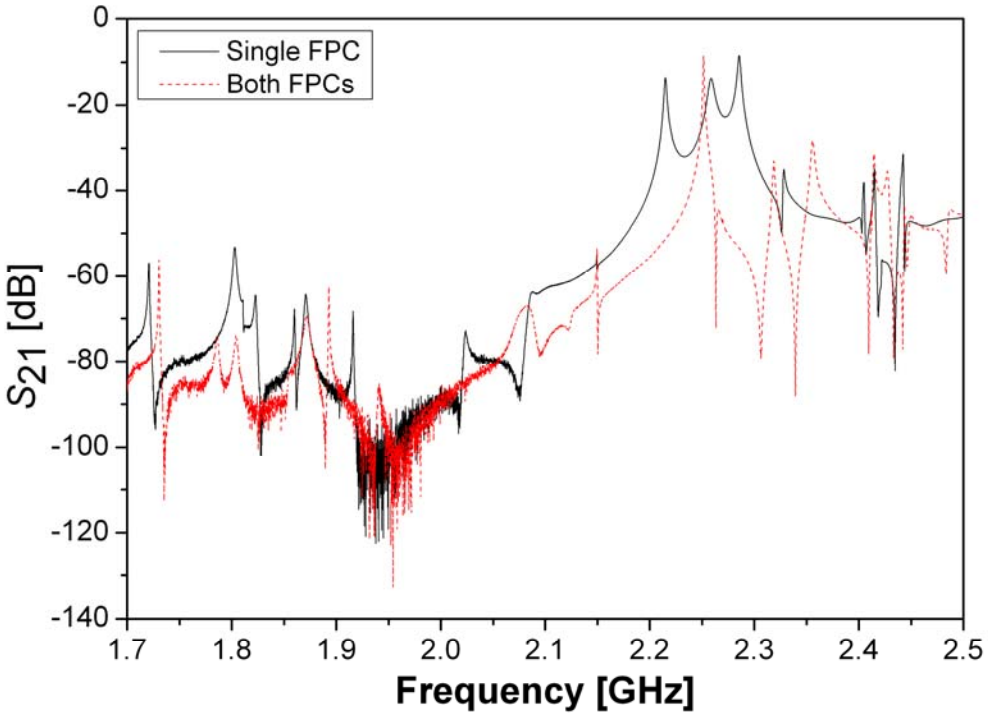

Figure 4.24: S_{21} measurements for single FPC and both FPCs inserted between 1.7 GHz and 2.5 GHz. Certain resonances seem to have higher Q-values when both FPCs are inserted and frequency shifting is evident.

In the second measurement configuration, both FPCs were inserted and the coupling was determined between the shorted and open cases for the FPCs. The results, listed in Table 4.7, here indicate that the coupling is rather weak at low frequencies and increases as frequency increases. However, coupling to low frequency modes below ~2.2 GHz does occur, and, as far as these modes are concerned, some damping is evident. This is particularly apparent when examining the Q-value for these different modes. The results are shown in Figure 4.25. These results show that the level of damping is largest between about 1 and 2 GHz. This is clear in the coupling values shown in Table 4.7, and, to some extent, is corroborated by the value of $1/k$. Thus, it would appear that, overall, the coupling seems rather weak, but, nonetheless, there is coupling at low frequencies, although the coupling increases at higher frequency. Recall that our concern is that the FPCs couple to frequencies below the cutoff frequency of the beampipe. Above this frequency, the damping is presumed to be dependent largely on the ferrite absorber downstream of the cavity.

Table 4.7 - Table of Coupling for Open, Shorted, and Terminated Configuratons of FPCs.

Reference		Shorted		Open		Terminated		Mode Type	1/*k*	Coupling
Frequency [GHz]	*Q*	Frequency [GHz]	*Q*	Frequency [GHz]	*Q*	Frequency [GHz]	*Q*			
0.70318	5817	0.70320	5212	0.70321	5809	0.70320	5456	Monopole	70320.5	1.06616
1.00821	4659	1.00819	4560	1.00820	4610	1.00820	4671	Dipole	100819.5	0.99743
1.48744	5097	1.48733	4830	1.48735	4875	1.48734	4288	Monopole	74367.0	1.18867
1.90679	4540	1.89347	1492	1.89341	1521	1.89359	1455	Dipole	31557.3	3.12028
2.26883	1296	2.25144	2320	2.25159	3181	2.25171	2489	Monpole	15010.1	0.52069
2.32625	--	2.31875	1140	2.31888	1184	2.31888	1091	Monpole	17837.0	--
2.53544	1218	2.53342	1577	2.53320	1612	2.53330	1387	Dipole	11515.0	0.87815
2.67551	5979	2.68273	1747	2.68337	1908	2.68313	1489	Dipole	4192.3	4.01545
2.86095	9126	2.86044	8716	2.86095	8060	2.86093	3451	Dipole	5609.2	2.64445
2.96535	2681	2.97309	2427	2.97120	2882	2.97323	675	Monpole	1572.6	3.97185

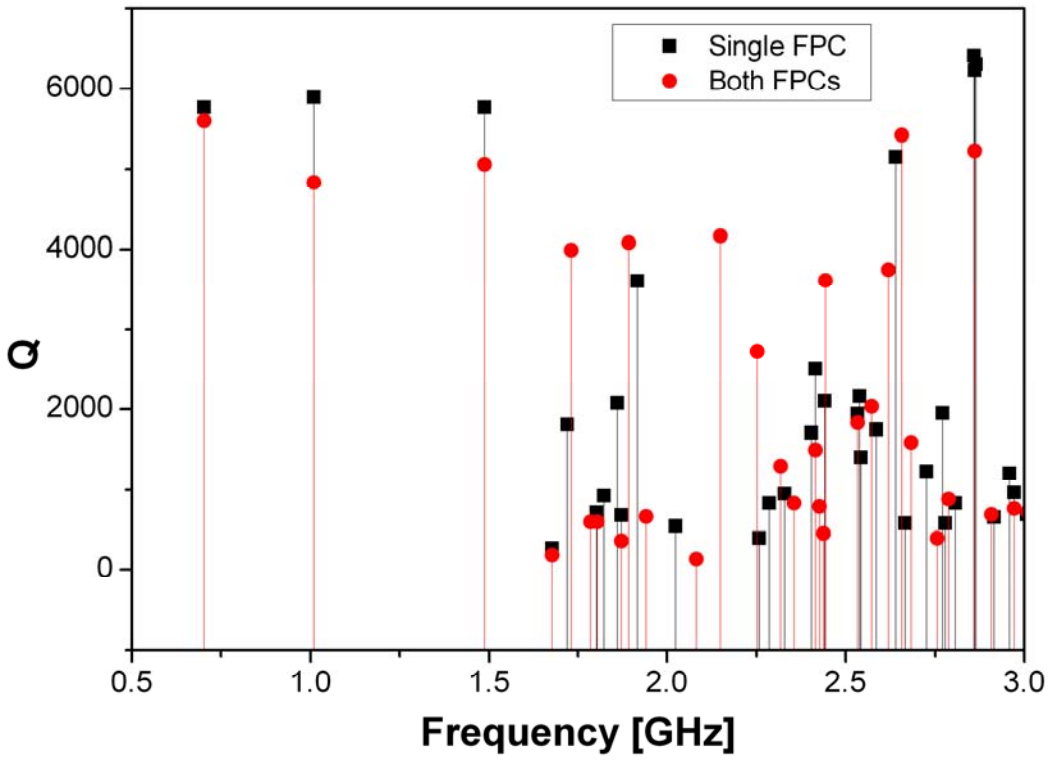

Figure 4.25 - Plot of *Q*-values for various configurations of FPCs.

4.5. Conclusions

The data from both simulation results and measurement show that the FPCs couple to low-frequency monopole and dipole modes between the fundamental frequency at 703 MHz and about 2.2 GHz, the cutoff frequency of the beampipe. The coupling in simulation appears to be somewhat stronger than measurement results, although the calculated Q_{ext} from measurement is of roughly the same order as the design value for the couplers (10^4). In the case of the simulation results, the damping of the Q-value seems to be several orders of magnitude, while in measurement this is not observed. It is important to keep in mind that the simulation results compare the cavity with no coupler ports to that in which both coupler ports and the couplers are present and perfectly terminated. This, of course, is different from the comparison made in the measurements. In the measurements, the effect of the couplers is gauged and compared for various port configurations. Thus, the simulations indicate that a significant effect is likely based on the presence of couplers; however, the measurements indicate the magnitude of the effect. The conclusion then, based on the consideration of both simulation and measurement results, is that there is significant coupling to higher-order modes from the FPCs, and the effect on damping varies with frequency. In general, at low frequency, the coupling of the mock FPCs to higher-order modes appears to be smaller than at higher frequencies, and coupling increases with frequency.

An important consideration in the measurements is the quality of the mock FPCs and their likeness to the actual FPCs that will be used in the cavity. While every effort was made to match the dimensions of the mock FPCs to the actual FPCs, the nature of the termination is crucial, and the results of the Q_{ext} calculation clearly indicate that the match is not perfect. It will be important to verify this measurement with the actual FPCs that will be used in the accelerator. However, given that the Q_{ext} of the mock FPCs is the same order of magnitude as the actual FPCs, it is warranted to conclude that there is significant damping of monopole and dipole modes, particular at between 1 and 2 GHz in agreement with simulation results.

It therefore would appear the FPCs potentially represent an important option for damping modes below the cutoff frequency of the beampipe. Recall that because these modes lie below the cutoff of the beampipe, they do not effectively couple to the ferrite absorber which lies downstream of the cavity. One objective of this study was to determine whether the FPCs might effectively couple to low-frequency higher-order modes as a means of supplementing the damp-

ing of these modes, and these results show that such coupling is possible. However, to determine the full extent to which the FPCs may couple to higher-order modes, it is also necessary to study the transmission from FPC to the circulator and through to the dump.

Chapter 5

Design of the Ferrite HOM Load with a Ceramic Insert

5.1. Basic Design of the HOM Load

The HOM load proposed for the ERL electron gun will be the focus of this chapter. The design features a novel element: the load surrounds a ceramic (alumina) break. A schematic of the design, along with pictures of the actual assembly are shown in Figure 5.1 and Figure 5.2. The inner diameter of the design is 5.08 cm and is uniform throughout the length of the damper. A simplified schematic showing the dimensions of the components of the damper is shown in Figure 5.3.

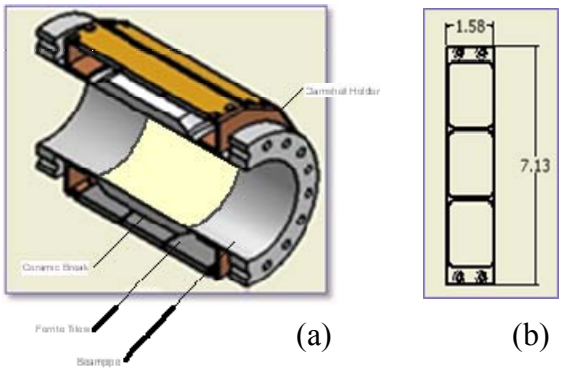

Figure 5.1: Schematic of the ferrite load surround a ceramic break. In (a), a cutaway view of the entire damper shows that a ceramic break is surrounded by plates that have three ferrite tiles attached to them. The plates are attached clamshell brackets that are attached to the beampipe. In (b) a plate is shown with dimensions in inches.

The design of the break is particularly useful because the ceramic can protect superconducting components from the dust or chips that might result from damage to the ferite tiles that serve as the HOM damping material. The ceramic is also an effective thermal transition that may be useful in various applications, and the use of the ceramic break, coupled with the design of the "clamshell" structure that holds the ferrite tiles in place, allows other damping materials to be quickly and easily installed and tested by simply replacing the damping material.

In order to study how such a damper might work, study began with a prototype consisting of a structure lined with ferrite surrounding a borosilicate glass tube. This structure was connected to a copper pillbox cavity and Q-values of the structure were measured as described below.

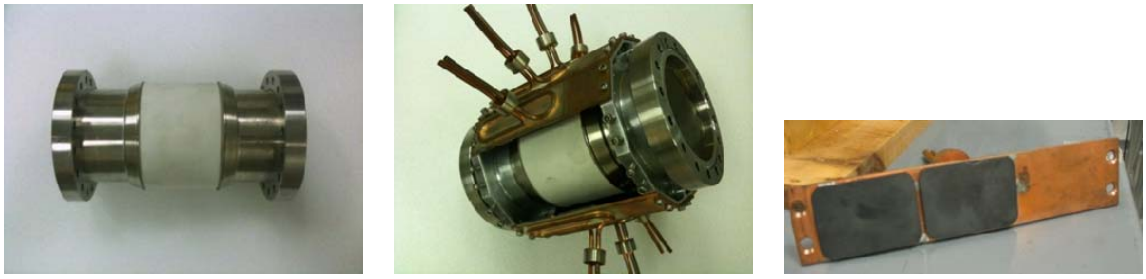

(a) (b) (c)

Figure 5.2: Pictures of the components of the actual ceramic/ferrite damper. (a) The ceramic break, (b) the ceramic break surrounded with copper plates to which ferrite tiles are attached. Several plates are removed to show the ceramic break. (c) Ferrite tiles attached to a copper plate.

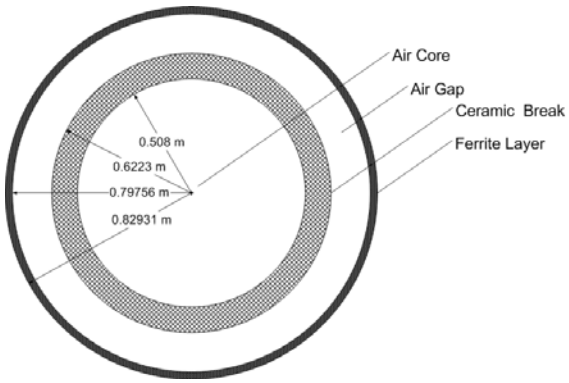

Figure 5.3: Schematic showing radii of various components of ceramic/ferrite damper.

5.2. Study of the Pillbox Cavity with a Glass Prototype

A copper pillbox cavity with beam port openings on either side of the cavity was constructed to simulate the niobium gun cavity. The higher-order modes of the copper pillbox cavity are easily calculated, and a listing of such modes is tabulated below in Table 5.1. A steel beampipe was obtained that slipped over the end of the cavity and was brought into electrical contact with the copper pillbox through copper/beryllium spring fingers attached to the copper beam port. Two basic measurement configurations were then used: For the baseline measurement, the steel tube was slipped over the beam port of the cavity and an aluminum endcap was fitted on the other end of the beampipe to form an electrical shorting plate. The cavity was then stimulated using a network analyzer (Agilent ENA5071C) from the other side of the cavity through a probe inserted into another electrical shorting plate attached to the beam port of the cavity opposite the beam tube. A second probe was attached to a port located on the wall of the pillbox cavity. This asymmetrical arrangement of the probes was useful because it could stimulate both monopole and higher order modes effectively. Q-values for the resonant modes of the cavity were then measured using the 3-dB technique, which the analyzer can provide automatically. These Q-values could then be compared to the same measurement with the prototype damper attached. The experimental setup is shown in Figure 5.4 and Figure 5.5.

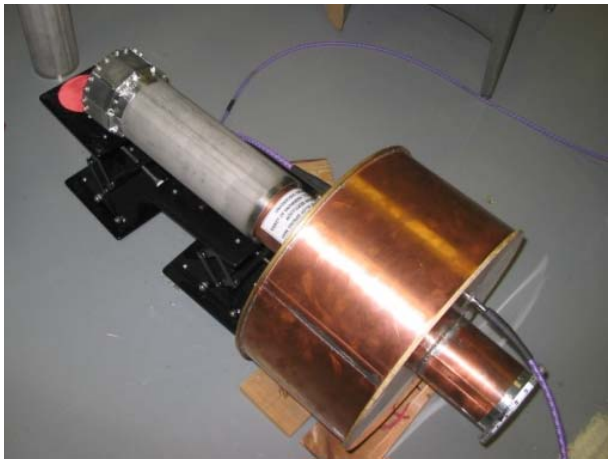

Figure 5.4: Experimental setup for prototype measurements of HOM damper showing beampipe and copper pillbox cavity.

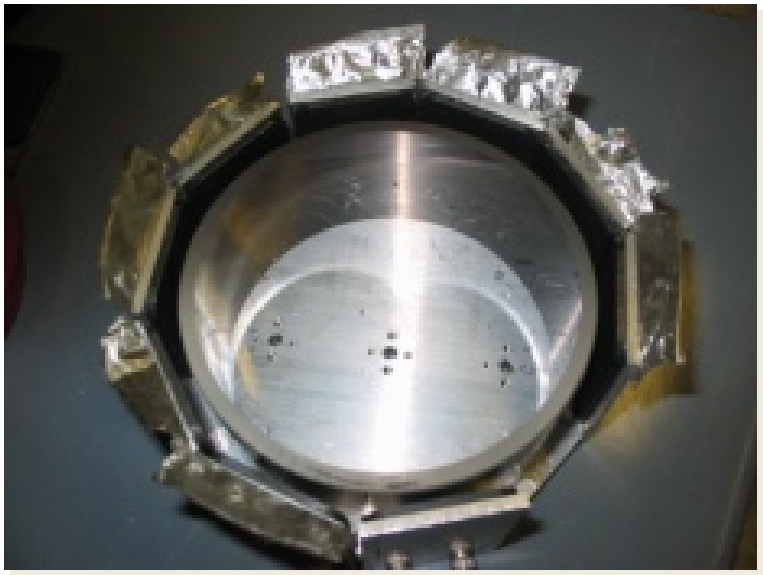

Figure 5.5: Experimental damper arrangement with glass insert.

Table 5.1: Table of TM Monopole and Dipole Modes for a Pillbox

Frequency [GHz]	Mode Class	Mode Type
0.0698	TM 010	Monopole
0.973	TM 011	Monopole
0.977	TM 110	Dipole
1.450	TM 020	Monopole
1.603	TM 012	Monopole
1.645	TM 021	Monopole
1.679	TM 112	Dipole
1.810	TM 120	Dipole
2.070	TM 022	Monopole
2.241	TM 030	Monopole
2.301	TM 122	Dipole
2.406	TM 031	Monopole
2.620	TM 023	Monopole
2.651	TM 130	Dipole
2.653	TM 032	Monopole
2.989	TM 034	Monopole

The prototype damper consisted of an aluminum plate to which a borosilicate glass cylinder ($\varepsilon = 6$) was attached by carefully affixing the glass onto the plate with metal tape at several locations. Around the outside of the plate, ferrite tiles braised onto aluminum plates were attached by screws to the perimeter. Using this arrangement, the ferrites essentially lined the inside of the damper, completely surrounding the glass tube. The entire assembly was, thereby, electrically shorted on one end by the aluminum plate. On the other end, the glass cylinder was attached to the beam tube, which was, in turn, slipped over the beam port of the cavity and electrically connected to the pillbox via the spring fingers. The glass was, once again, attached to the beam pipe using metal tape, taking care to make the connection to the beampipe as secure and electrically continuous as possible. The outside of the damper was then wrapped in aluminum foil in such a manner as to attempt to electrically connect the outside of the damper to the outside of the beampipe in order to mimic the configuration of the actual damper. Finally, the distance from the pillbox wall on the beampipe side to the end of the damper was then adjusted such that this distance was the same as that of the baseline configuration without the ferrite damper. This was necessary so that all modes would experience the same geometrical configuration. The Q-value of this setup was then obtained using the network analyzer.

In another measurement, the glass insert was removed from the damper, leaving only the ferrite tiles. This damper arrangement was also attached to the end of the beampipe in the manner described above except that the outside of the damper was then attached to the beampipe using metal tape in such a manner as to try to assure electrical continuity. The damper and the end of the beampipe were then wrapped in aluminum foil so as to also enhance electrical continuity of the beampipe and the damper. Once more, the Q-values of this setup were obtained, and compared to both the baseline and the results with the glass insert. All of the results were then compared for monopole and dipole modes as shown in Figure 5.6 and Figure 5.7 below.

The data show a clear damping effect in the glass/ferrite damper relative to the baseline measurement, i.e., the Q-value of the glass/ferrite damper arrangement is lower than that of the pillbox and beampipe system alone. Damping is achieved in this prototype system despite the presence of the glass. The situation becomes even more interesting when one compares the damping of the ferrite alone to the glass/ferrite damper. Here it is noted that, in most cases, the Q-value of the glass/ferrite damper system is below that of the damper loaded only with ferrite. This sug-

gests that the glass may somehow enhance the damping effect, at least for certain modes. In the following sections, the origins of this effect will be further investigated along with measurements and calculations of the actual damper to be used in the ERL.

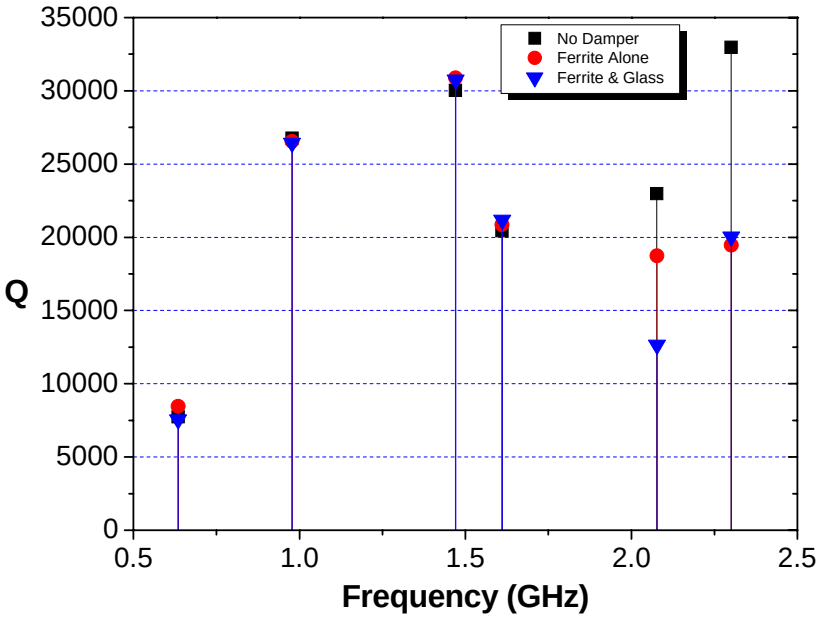

Figure 5.6: Measurement of monopole modes using prototype test structure.

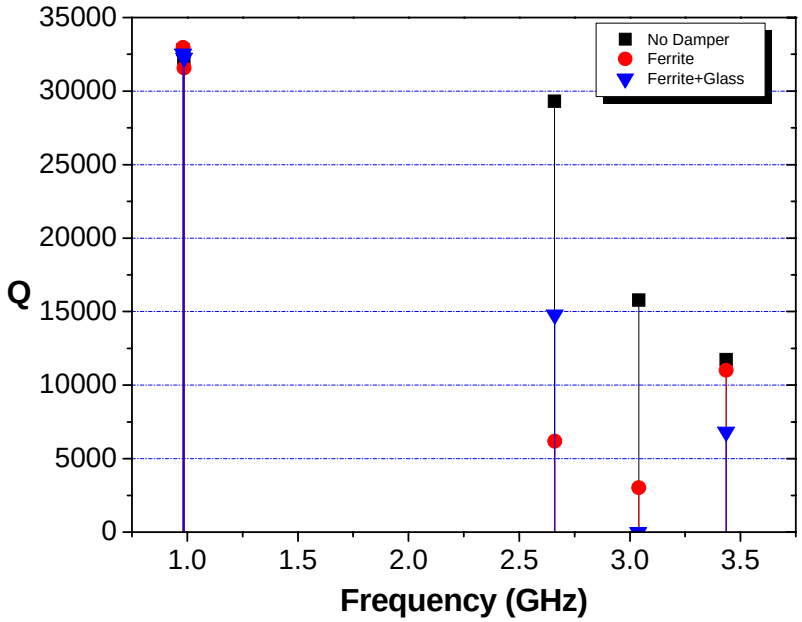

Figure 5.7: Measurement of dipole modes using prototype test structure.

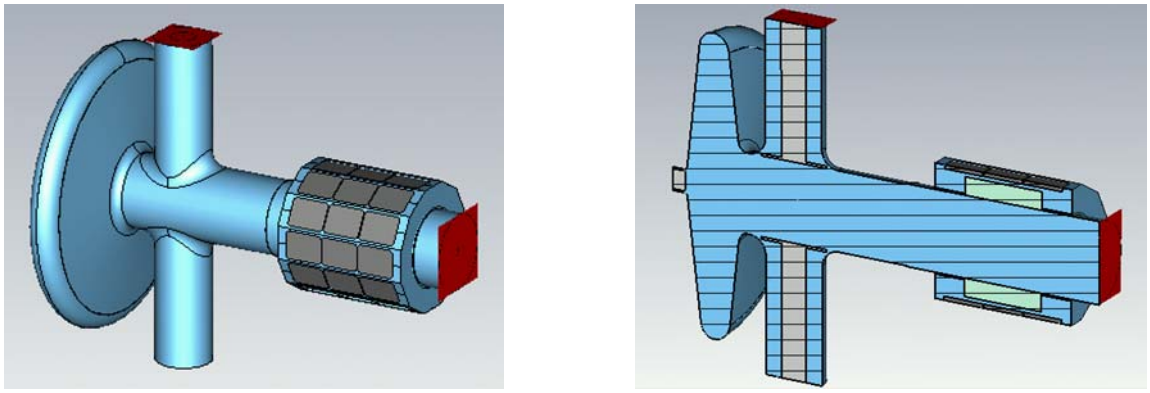

(a) (b)

Figure 5.8: Model of the gun attached to the ceramic/ferrite damper in (a). In (b), a cutaway view of the model is shown, exposing the ceramic layer inside the ceramic/ferrite damper. Red boxes are waveguide ports through which energy can pass into and out of the structure.

5.3. Simulation Studies of the Ceramic/Ferrite Damper

Simulation studies were pursued to determine the expected damping performance for the ceramic/ferrite HOM load attached to the electron gun. For the simulation studies, Microwave Studio was used to perform S_{21} simulations with the frequency solver of a structure consisting of the gun cavity attached directly to the ceramic damper as shown in Figure 5.8. The model for the ferrite-ceramic damper itself is shown in Figure 5.9. For the simulations, the behavior of the gun-and-damper-system with and without the ceramic insert was compared particularly in the region from 2 GHz to 3 GHz. This regime consists of both monopole and dipole modes, and it is expected that the damper should effectively interact with both types. Recall that the radius of the beampipe is 5.08 cm, and the TM_{01} cutoff is at 2.2 GHz, thus the region around 2 GHz is where the damper is expected to interact with modes emanating from the cavity. For the simulation, three configurations were compared: in the first configuration, the model consisted of a gun attached to a straight section of beampipe with the same length as the ferrite-ceramic damper. This model allowed a baseline to be obtained against which the next two configurations could be compared. In the second configuration, the model consisted of the gun attached to a damper which included only the ferrite lining the wall of the damper without the intervening ceramic layer. In the third configuration, the intervening ceramic layer was included. In actual terms, the ceramic forms a break between sections of beampipe. This break, in turn, is surrounded by a ferrite cylinder as shown in Figure 5.9. In all cases, the FPC ports as well as the end of the beam-

pipe were terminated in waveguide ports, thus ensuring perfect impedance matching at these locations. The results of the simulation are plotted in Figure 5.10.

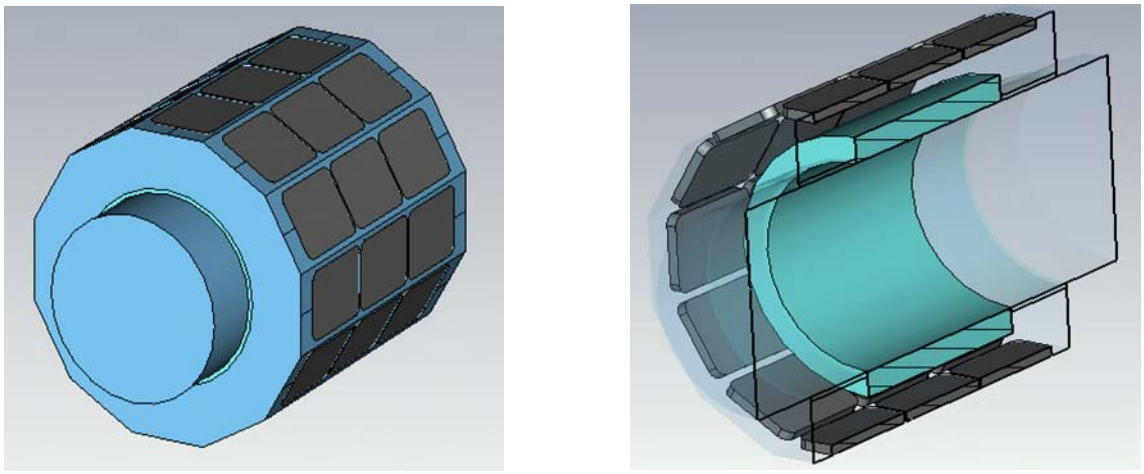

(a) (b)

Figure 5.9: Detail of the model for the ceramic damper.

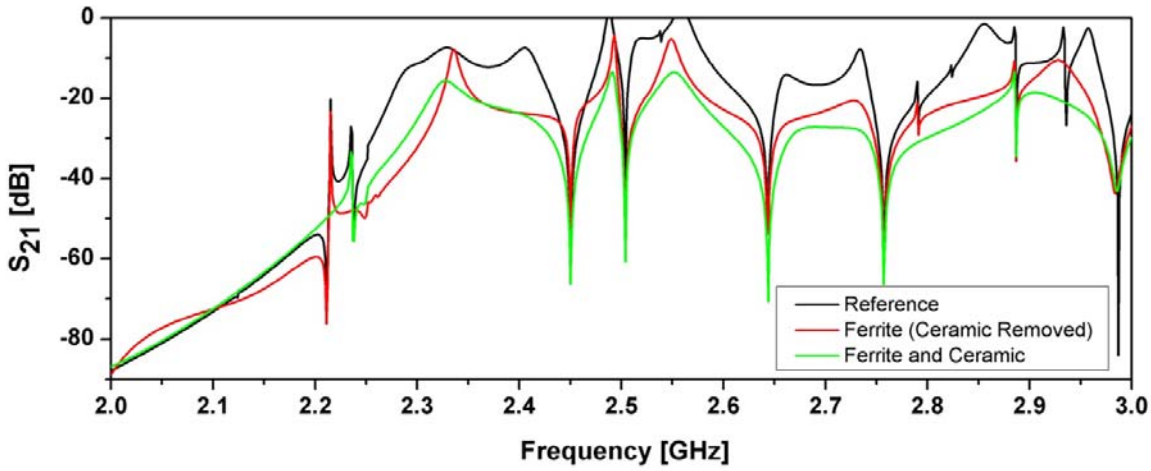

Figure 5.10: Plot of simulated S_{21} obtained from gun-and-damper model for various configurations.

Notice that the damping effect is evident in both the ferrite-alone and ferrite-and-ceramic configurations compared to the baseline case. The damping becomes noticeable above ~2.3 GHz, consistent with the cutoff value of the beamtube radius. It is also clear that the ferrite-and-ceramic configuration shows the greatest damping, consistently measuring 10-15 dB less than the baseline, particularly at the signal resonances, and 5 dB less than the ferrite-alone configura-

tion at signal resonances. These results clearly suggest that the arrangement of ceramic and ferrite is effective in damping higher-order modes, and, indeed, contributes to the damping performance. This contribution shall be explored in subsequent calculations below.

5.4. Study of the Gun Cavity Attached to the Ceramic/Ferrite Damper

After studies of the glass prototype were completed, the actual niobium cavity and ceramic/ferrite damper became available and were used to study the damping effect of the actual device. For the experiments, the damper, configured in several different ways, was attached directly to the gun cavity and stimulated from the cathode port at the rear of the cavity using a network analyzer. A pickup probe was attached to the RF pickup port on the opposite side of the cavity. All other openings including the beampipe and FPC ports on either side of the cavity were covered with shorting plates. S_{21} measurements were conducted in a frequency range from 0.5 GHz up to 3.0 GHz. A picture of the basic experimental setup is shown in Figure 5.11.

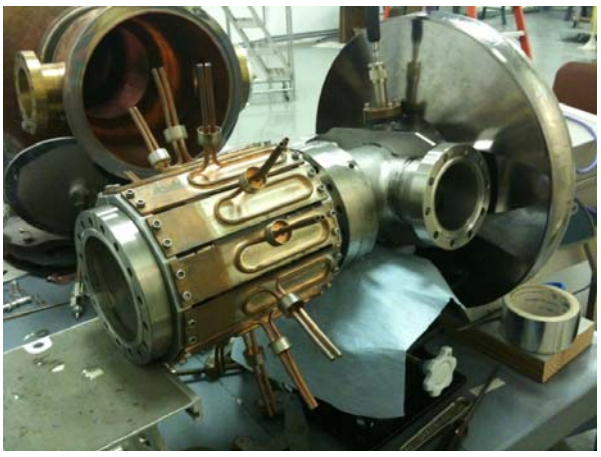

Figure 5.11: Niobium cavity with ceramic/ferrite damper attached. Note the pickup probe, attached to the RF pickup right of center. For measurements, all of the openings including the beampipe and the FPC ports were covered by shorting plates.

In addition to measurement of the full damper with ceramic and ferrite plates attached, measurements were also conducted with the ferrite tiles removed and the ceramic break wrapped

with a metal sheet. These measurements were compared with a straight section of beampipe that served as a reference. The results of the various measurements are tabulated in Table 5.2 and plotted in several different forms in the following figures.

Table 5.2 - Table of *Q*-Value Measurements for Monopole and Dipole Modes of Damper in Various Configurations Attached to Cavity

Frequency [GHz]	Mode Type	*Q*-value				
		Ceramic and Ferrite	Ceramic with Metal Jacket	Ceramic Only	Ferrite Only- No Ceramic	Reference
0.703	mono	5859	5842	5838	*	5845
1.008	dipole	4725	4655	4348	*	4710
1.487	mono	5438	5444	5143	*	5342
1.763	dipole	169	--	--	*	6278
1.835	dipole	--	--	--	*	1969
2.007	dipole	--	--	--	*	927
2.150	dipole	2559	2730	2552	2770	2429
2.536	dipole	--	583	--	652	652
2.841	dipole	--	--	--	--	2516
2.861	dipole	--	5013	--	3593	9257
2.924	dipole	--	622	--	301	885
2.942	dipole	--	--	--	--	889

*Frequencies not measured because they fall below cutoff value of beampipe.

As the table indicates, *Q*-values for the combination of the gun and the ceramic-ferrite damper are the lowest of all of the different damper configurations that were measured for frequencies above 1.75 GHz. Many of the *Q*-values above this frequency are too small to be measured. A comparison of the *Q*-values for the ceramic-ferrite damper and the reference beampipe is shown in the plot of Figure 5.12. The plot also indicates that substantial damping is observed only for frequencies above 1.75 GHz. Since the lowest cutoff frequency for TM modes given the 0.508 cm radius of the beampipe is 2.25 GHz, it is clear that modes below 2.25 GHz simply cannot interact with the damper which is downstream of the cavity. This makes the case of the mode at 1.76 GHz especially interesting because it shows a substantial *Q*-value for the reference

structure and a very low Q-value when the ceramic-ferrite damper is introduced. At this frequency, simulation shows that the mode is essentially one of the beampipe with a relatively small field distribution in the cavity. An example of the simulation result is shown in Figure 5.13.

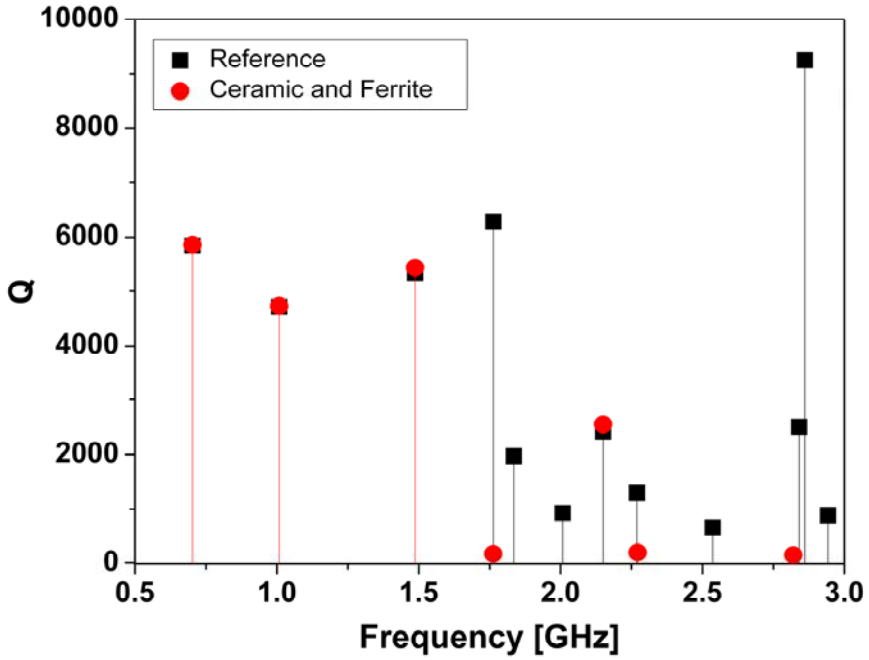

Figure 5.12: Plot of Q-values for monopole and dipole modes for gun attached to ceramic and ferrite damper and gun with reference beampipe.

In comparing the performance of the ceramic-ferrite damper with the ferrite alone, it is important to note that for the case of the ferrite alone, the ferrite sits at the same radius as in the ceramic and ferrite combination. The ceramic was "removed" in the sense that the ferrite tiles were arranged around a set of tubes that allowed the ferrites to be held in place at the same radius as in the ceramic-and-ferrite combination but, where the ceramic would normally be placed, there was only an empty space. Thus, the geometry is essentially the same as that of a ceramic-and-ferrite damper with the ceramic removed. In practice, it would not be possible to simply remove the ceramic from the design. Furthermore, it would be more likely that if the ceramic were removed from the design, the ferrite would be placed such that the inner diameter of the ferrite would be at the same radius as the beampipe.

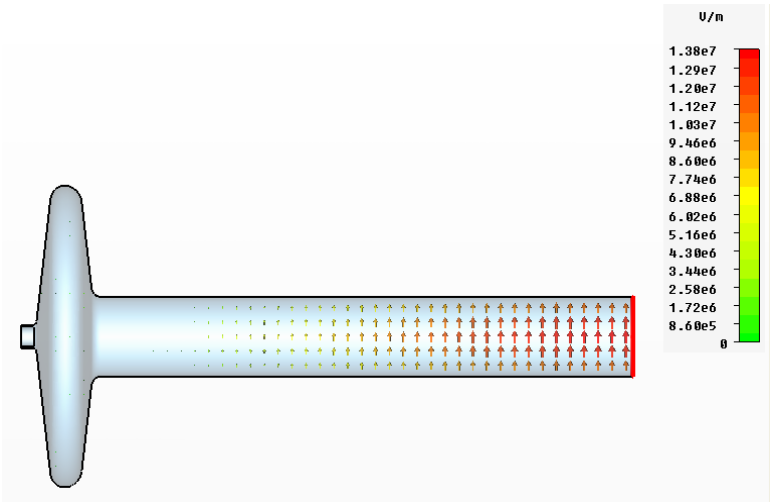

Figure 5.13: An example of the simulation result for the mode at 1.761 GHz. While this mode has a TM dipole mode profile in the cavity, this is essentially a mode of the beampipe and, therefore, couples strongly to the ceramic-ferrite damper as measurements show. The existence of modes of the beampipe is important to recognize in meaurements of damping in both the gun and the five-cell cavity since they can be easily confused with modes of the cavity.

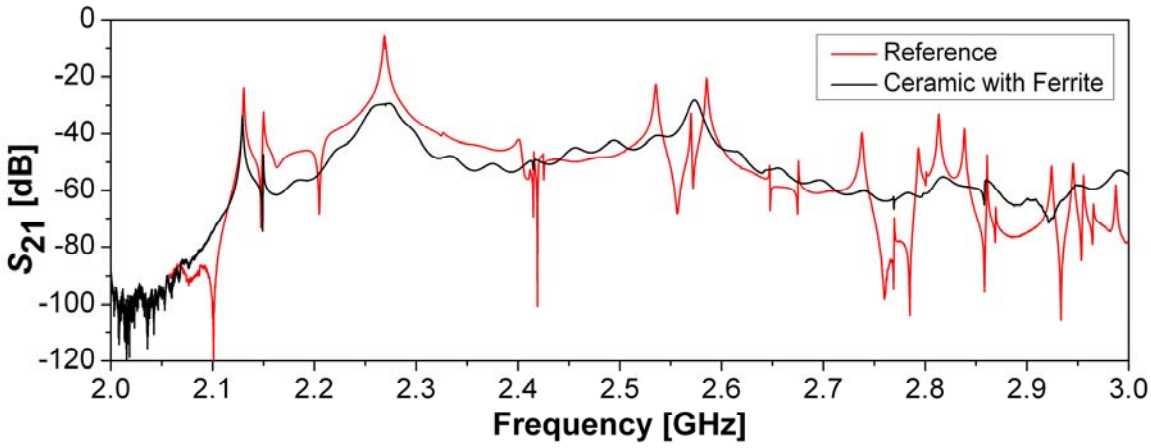

Figure 5.14: Plot of S_{21} data for gun attached to reference beampipe and attached to ceramic-ferrite damper for frequencies between 2 and 3 GHz.

Nonetheless, the key point is that the ferrite seems to offer a level of HOM damping that is comparable to that of the ferrite alone, validating the incorporation of ceramic into the design. Figure 5.14 shows the S_{21} plot of the gun with the reference beampipe and with the ceramic-ferrite damper. The extent of damping is quite evident.

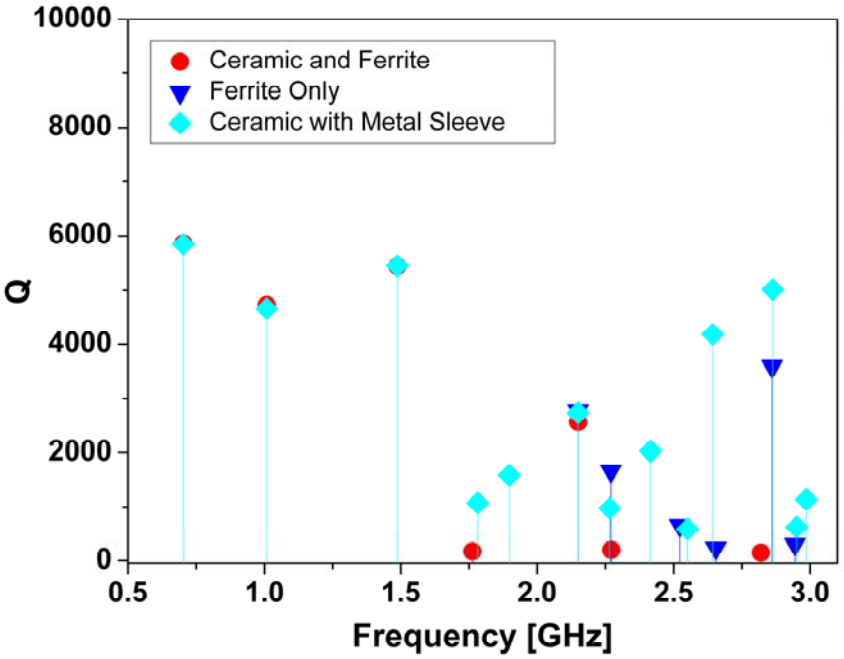

Figure 5.15: Plot of Q-values for configurations of damper including ferrite only (at same radius as in ceramic-and-ferrite damper) and ceramic wrapped with metallic sleeve.

Figure 5.15 shows the Q-values for other measurements of the gun with other damper configurations including the ferrite alone, without the intervening ceramic layer, and with the ceramic alone, wrapped with a metallic sleeve along with the ceramic and ferrite damper for comparison. It is interesting to note that the ceramic alone appears to provide no damping of higher-order modes. This is expected, since the ceramic is practically lossless. Of particular interest is the comparison of the ceramic-and-ferrite combination to that of ferrite alone. Taking into account that if the ferrite alone were to be used in an actual damper, its inner radius would likely be the same as the beampipe in roughly the same manner as it is configured for the five-cell cavity, it is nonetheless interesting to note that when the ceramic layer is present, the damping for certain modes is slightly, or, sometimes, significantly enhanced. To understand this phenomenon and to provide an analytical framework for further optimization, the damper was analyzed as a waveguide, and the attenuation characteristics of the device were calculated as described in the next section.

5.5. Attenuation in the Ceramic/Ferrite Damper

To understand the behavior of the ceramic/ferrite damper more fully and to provide a framework for calculating the properties of the damper, the device was analyzed both as a resonant structure by placing shorting plates on both ends of the structure and then calculation and measuring the *Q*-values of the structure as well as analyzing the damper as a waveguide and then calculating the attenuation of modes in the structure.

5.5.1. *Q*-values of the Ceramic/Ferrite Damper

To begin, the *Q*-values of various devices incorporating a dielectric layer and a ferrite layer with the same geometry and roughly the same dimensions as the actual ceramic/ferrite damper were compared to determine the effect of the dielectric layer on the fields inside the structure. When the structure is closed, the damper is essentially a pillbox cavity whose resonant frequency and Q can be calculated and compared to measurement results. To this end, we consider the damper as a boundary value problem and we seek to match conditions at each of the boundaries of each region (air, ceramic, and ferrite). Each of these regions is characterized by its respective material parameters (ϵ, μ) and the fields within each region are matched at the boundary, yielding a dispersion relation from which the complex propogation constant for each mode may be determined. For the resonant cavity, we shall assume the modes to be TM in nature, owing to manner in which they will be stimulated in experiment, with both probes placed in the center of the shorting plates, although this is of little consequence for calculation since any mode could be calculated, but this shall limit the range of possible solutions.

We shall consider then a cylindrical geometry (r, θ, ϕ) for the damper and assume the outer layer to be perfectly conducting. The longitudinal axis of the damper shall correspond to the *z*-axis, and both the permittivity ϵ_i and the permeability μ_i shall be allowed to be complex as required. Then, the resonant frequency shall be derived from the method of seeking nontrivial solutions for the coeefficients of the field expressions of the equations obtained by enforcing the continuity of the four tangential fields $E_z, H_z, E_\phi,$ and H_ϕ at each interface between the layers and between the innermost layer and the interior of the beampipe. For the TM mode, then $H_z = 0$ and $E_\phi = 0$.

We may express the electromagnetic fields in terms of their wavefunctions [13, 14]. We note that in a homogenous, source-free region, the field potentials must satisfy the Helmholtz equation,

$$\nabla^2\psi + k^2\psi = 0 \tag{5.1}$$

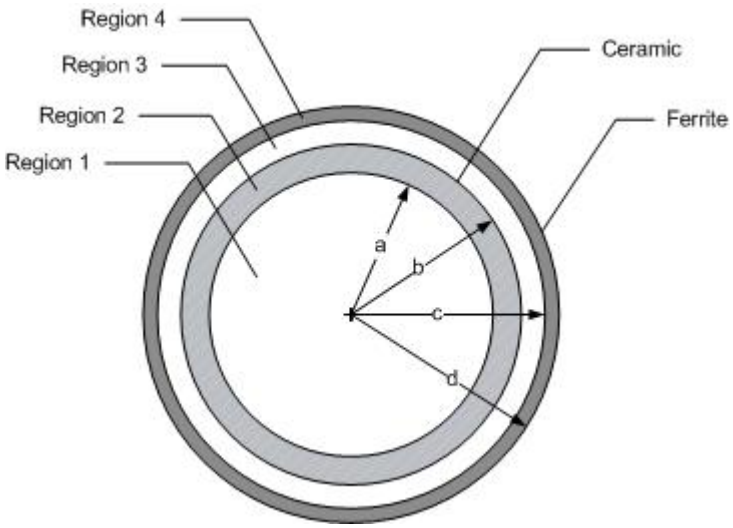

Figure 5.16: Geometry of damper.

Then, the fields TM to z, in cylindrical coordinates are given by:

$$\begin{aligned} E_\rho &= \frac{1}{\hat{y}}\frac{\partial^2\psi}{\partial\rho\,\partial z} & H_\rho &= \frac{1}{\rho}\frac{\partial\psi}{\partial\phi} \\ E_\phi &= \frac{1}{\hat{y}\,\rho}\frac{\partial^2\psi}{\partial\phi\,\partial z} & H_\phi &= -\frac{\partial\psi}{\partial\rho} \\ E_z &= \frac{1}{\hat{y}}\left(\frac{\partial^2}{\partial z^2} + k^2\right)\psi & H_z &= 0 \end{aligned} \tag{5.2}$$

where, $\hat{y} = j\omega\epsilon$ and $\hat{z} = j\omega\mu$. Similarly, the fields TE to z can be expressed as:

$$\begin{aligned} E_\rho &= -\frac{1}{\rho}\frac{\partial\psi}{\partial\phi} & H_\rho &= \frac{1}{\hat{z}}\frac{\partial^2\psi}{\partial\rho\,\partial z} \\ E_\phi &= \frac{\partial\psi}{\partial\rho} & H_\phi &= \frac{1}{\hat{z}}\frac{\partial^2\psi}{\partial\phi\,\partial z} \\ E_z &= 0 & H_z &= \frac{1}{\hat{z}}\left(\frac{\partial^2}{\partial z^2} + k^2\right)\psi \end{aligned} \tag{5.3}$$

These, now, are very compact expressions applicable to any structure. Let us consider the geometry posed by the ceramic-ferrite damper as shown schematically in Figure 5.16. In such a system, the modes are neither TE nor TM to any cylindrical coordinate except for the rotational symmetric modes (n = 0) as shall soon be observed. In general, the solution for each field shall be a combination of the TM and TE field expressions. Let us examine the field expressions at the first interface. Let region 1 be the inner region (air) and region 2 be the dielectric cylinder (ceramic). Then the electric and magnetic wavefunctions are given by

$$\begin{aligned} \psi^{m1} &= AB_n^{m1}\left(k_{\rho 1}\rho\right)\cos n\phi\, e^{-jk_z z} \\ \psi^{e1} &= BB_n^{e1}\left(k_{\rho 1}\rho\right)\sin n\phi\, e^{-jk_z z} \end{aligned} \tag{5.4}$$

in region 1, and

$$\begin{aligned} \psi^{m2} &= CB_n^{m2}\left(k_{\rho 2}\rho\right)\cos n\phi\, e^{-jk_z z} \\ \psi^{e2} &= DB_n^{e2}\left(k_{\rho 2}\rho\right)\sin n\phi\, e^{-jk_z z} \end{aligned} \tag{5.5}$$

in region 2. The ψ^m determine the partial fields according to equation 5.2 and the ψ^e determine the partial fields according to equation 5.3. The total field is the sum of the partial fields in each region. The $B_n\left(k_\rho\rho\right)$ are Bessel functions appropriate to each region that satisfy all the boundary conditions except those at the interface $\rho = a$. In each region, the ψs must satisfy the relationships among the propogation constants:

$$\begin{aligned} k_{\rho 1}^2 + k_z^2 &= k_1^2 = \omega^2\epsilon_1\mu_1 \\ k_{\rho 2}^2 + k_z^2 &= k_2^2 = \omega^2\epsilon_2\mu_2 \end{aligned} \tag{5.6}$$

But, for a cavity, $k_z = 0$. Then, our expressions become:

$$\begin{aligned} k_{\rho 1}^2 &= k_1^2 = \omega^2\epsilon_1\mu_1 \\ k_{\rho 2}^2 &= k_2^2 = \omega^2\epsilon_2\mu_2 \end{aligned} \tag{5.7}$$

The constraint that E_z, H_z, H_ϕ, and E_ϕ be continuous at $\rho = a$ lead to

$$
\begin{aligned}
\epsilon_2 k_{\rho 1}^2 A B_n^{m1}(k_{\rho 1}a) &= \epsilon_1 k_{\rho 2}^2 C B_n^{m2}(k_{\rho 2}a) \\
\mu_2 k_{\rho 1}^2 B B_n^{e1}(k_{\rho 1}a) &= \mu_1 k_{\rho 2}^2 D B_n^{e2}(k_{\rho 2}a) \\
A k_{\rho 1} B_n^{m1\prime}(k_{\rho 1}a) + \frac{B k_z n}{\omega \mu_1 a} B_n^{e1}(k_{\rho 1}a) &= C k_{\rho 2} B_n^{m2\prime}(k_{\rho 2}a) + \frac{D k_z n}{\omega \mu_2 a} B_n^{e2}(k_{\rho 2}a) \\
\frac{A k_z n}{\omega \epsilon_1 a} B_n^{m1}(k_{\rho 1}a) + B k_{\rho 1} B_n^{e1\prime}(k_{\rho 1}a) &= \frac{C k_z n}{\omega \epsilon_2 a} B_n^{m2}(k_{\rho 2}a) + D k_{\rho 2} B_n^{e2\prime}(k_{\rho 2}a)
\end{aligned}
\tag{5.8}
$$

In all of these expressions, the convention of $e^{j(\omega t - k_z z)}$ is understood and supressed. If we assume that there are only two layers, and that the second, outer layer is bounded by a perfect conductor, then it is clear that this set of equations has a nontrivial solution only if the determinant of the coefficients *A*, *B*, *C*, and *D* vanishes. Let

$$
\begin{aligned}
F_1 &= B_n^{m1}(k_{\rho 1}a) \qquad F_2 = B_n^{e1}(k_{\rho 1}a) \\
F_3 &= B_n^{m2}(k_{\rho 2}a) \qquad F_4 = B_n^{e2}(k_{\rho 2}a)
\end{aligned}
\tag{5.9}
$$

Then, the characteristic equation can be written as a determinant:

$$
\begin{vmatrix}
\epsilon_2 k_{\rho 1}^2 F_1 & 0 & -\epsilon_1 k_{\rho 2}^2 F_3 & 0 \\
0 & \mu_2 k_{\rho 1}^2 F_2 & 0 & \mu_1 k_{\rho 2}^2 F_4 \\
k_{\rho 1} F_1{}' & \frac{k_z n}{\omega \mu_1 a} F_2 & -k_{\rho 2} F_3{}' & \frac{k_z n}{\omega \mu_2 a} F_4 \\
\frac{k_z n}{\omega \epsilon_1 a} F_1 & k_{\rho 1} F_2{}' & \frac{k_z n}{\omega \epsilon_2 a} F_3 & k_{\rho 2} F_4{}'
\end{vmatrix} = 0
\tag{5.10}
$$

When $n = 0$ and $k_z = 0$, inspection of the determinant reveals that the fields separate modes TE and TM to *z*.

It will therefore be necessary to solve this determinant for the appropriate ωs that correspond to the resonances of the cavity. It is clear that, because of the complex material parameters of the ferrite, the frequencies must also be complex. From this, it is also possible to show [13] that the *Q* is given by

$$
Q = \frac{Re(\omega)}{Im(\omega)}
\tag{5.11}
$$

Of course, in practice, only the real part of the frequency can be measured. However, both the real and imaginary parts of the frequency contribute to the measured *Q*-value.

The resonant frequency of the TM_{010} was thus calculated using using Wolfram Mathematica [28] and compared to measurements of the various structures using a network analyzer. The results are tabulated below.

Table 5.3 - Calculated and Measured Resonant Frequencies for Various Dielectric Materials in Damper Configuration with Ferrite

Dielectric	ε	Calculated Frequency [GHz]		Calculated Q	Measured Frequency [GHz]	Measured Q
		Re	Im			
Ceramic	9.9	0.80	0.08	9.99	0.80	5.90
Glass	4.6	1.03	0.15	6.86	1.16	4.83
PVC	3.19	1.13	0.38	2.97	1.25	4.46

From the table, the reasonable agreement between measurement and theory can be noted. Also note that as the dielectric constant of the intervening dielectric layer increases, both the calculated and measured Q increase. Since there is no dissipation in the dielectric layers and the loss is confined to the ferrite, the increasing Q-value suggests that the dielectric layer shields the fields from interacting with the ferrite layer. The mechanism for this process can be understood by considering the effect of the dielectric on electric fields in general: such materials tend to concentrate the fields within themselves, distorting the field profile, and, in this, case moving the fields away from the ferrite. While both the dielectric layer and the ferrite layer ($\epsilon = 13$) have relatively high dielectric constants, the change in the Q-value for different dielectric layers suggests that some distortion of the field must be taking place. Furthermore, the larger the dielectric constant of the intervening layer, the larger the shielding effect.

5.5.2. Attenuation in the Ceramic/Ferrite Damper

The attenuation of the damper is important because it corresponds directly to its HOM damping performance. The attenuation constant α of a normal mode in a waveguide is related to the magnetic and electric energies in the dissipative regions of the structure, $|\mathbf{H}|^2$ and $|\mathbf{E}|^2$, by

$$\alpha \propto \int_v [Im|\mu|^2|\mathbf{H}|^2 + Im|\epsilon|^2|\mathbf{E}|^2]dV \quad 5.12$$

where the volume of integration is over the lossy region. Because of the significant distortions of the electric and magnetic fields by the dielectric layers as described above, it is interesting to explore the effect of varying the geometrical parameters of the damper on the attenuation. To this end, the effect of varying thickness of the ceramic layer was calculated to determine how the ceramic affects the damping performance.

Calculations of the attenuation constant were conducted using the theoretical framework described above for both TM monopole (n = 0) and dipole (n = 1) modes as well as TE dipole (n = 1) modes. TE dipole modes were calculated because these modes have the lowest cutoff frequencies in a cylindrical waveguide. For these calculations, the damper was considered as a waveguide, and the longitudinal propagation constant was considered a free parameter that was solved as the root to a transcendental equation, but is related to the wavenumber via the relation in equation 5.6. Then,

$$k_z = j\alpha - \beta \quad 5.13$$

where we recall that the wavefunction includes the term $e^{j(\omega t - k_z z)}$. Thus, we see that the attenuation constant amounts to the real attenuation $e^{-\alpha z}$ along with a phase constant β. Because, the permeability of the ferrite is frequency-dependent, calculations at several different frequencies were conducted, based on the permeability data measured by Mouris and Hutcheon [24], summarized in Figure 5.17.

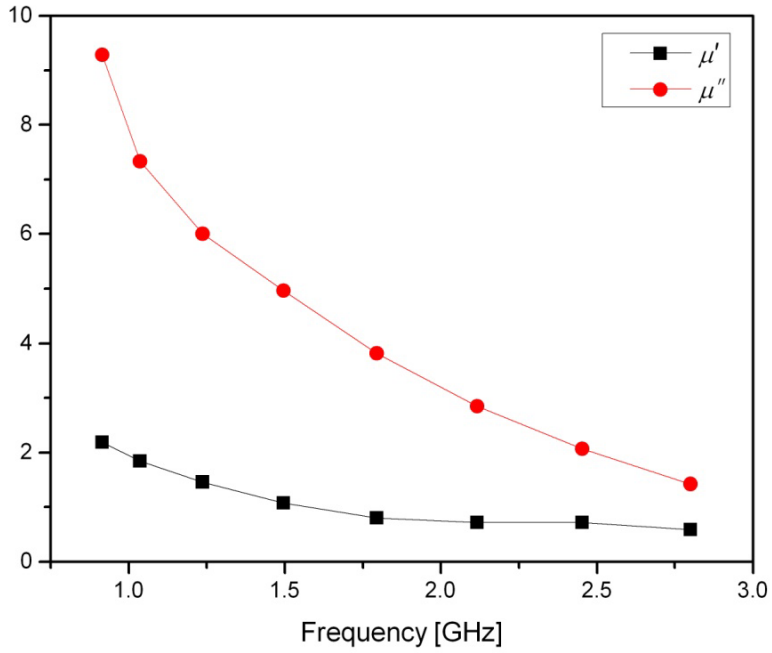

Figure 5.17: Complex permeability data as measured by Mouris and Hutcheon. μ' is the real part and μ'' is the imaginary part of the permeability.

In order to calculate the attenuation values, the propogation constant k_z was calculated in stages starting from the case where both the ceramic and ferrite layers were absent, yielding the value of a cylindrical, perfectly conducting waveguide alone. Then the ferrite layer was gradually thickened until the actual ferrite thickness used in the damper was achieved, recording the value of the attenuation throughout. Next, the ceramic layer was thickened and the value of the attenuation was recorded until the final thickness of the ceramic was achieved. This allowed the root of the determinant to be accurately identified and tracked throughout the procedure and allowed for characterization of the root as either HE or EH since, in the limiting case of vanishing dielectric layers,

$$HE_{nm} \rightarrow TE_{nm} \text{ and } EH_{nm} \rightarrow TM_{nm} \qquad 5.14$$

Note that for $n = 0$, the modes are still separable into TE and TM modes even in the presence of losses. For such modes, we may still speak of TM and TE monopole modes, but for higher-order modes, we speak of HE and EH modes.

The results of these calculations for varying ceramic thickness and the actual ferrite thickness used in the ceramic/ferrite damper are plotted in Figure 5.18, Figure 5.19, and Figure 5.20. These results show that, for all mode types, increasing frequency results in lower total attenuation. This is expected because of the frequency-dependent permeability of the ferrite: with increasing frequency, the imaginary part of the ferrite permeability falls. Note that in the case of the HE modes, the overall attenuation is much less than TM monopole and EH modes. This is likely explained by the relatively low magnetic fields at the wall of a cylindrical structure for TE modes. TE modes have the highest magnetic fields at the center of a cylindrical structure. Attenuation is greatest for EH modes. For TM modes, the highest magnetic fields are found at the wall of the structure. Furthermore, because of the azimuthal symmetry of the modes, these overlap of the magnetic field with the ferrite is large, ensuring maximal attenuation.

It is also very interesting to note the peak in attenuation that occurs at each frequency in the case of both HE and EH (TM) modes. For TM monopole modes, the peak attenuation occurs at different ceramic thicknesses for different frequencies, but, for the frequencies considered, the peak is between about 2.5 and 6 mm depending on frequency. In the case of HE modes, a similar effect is evident but with a strong peak shared by almost all frequencies at ~1.5 mm. For EH modes, such peaks are observed only at the highest frequencies (2.453 and 2.799 GHz).

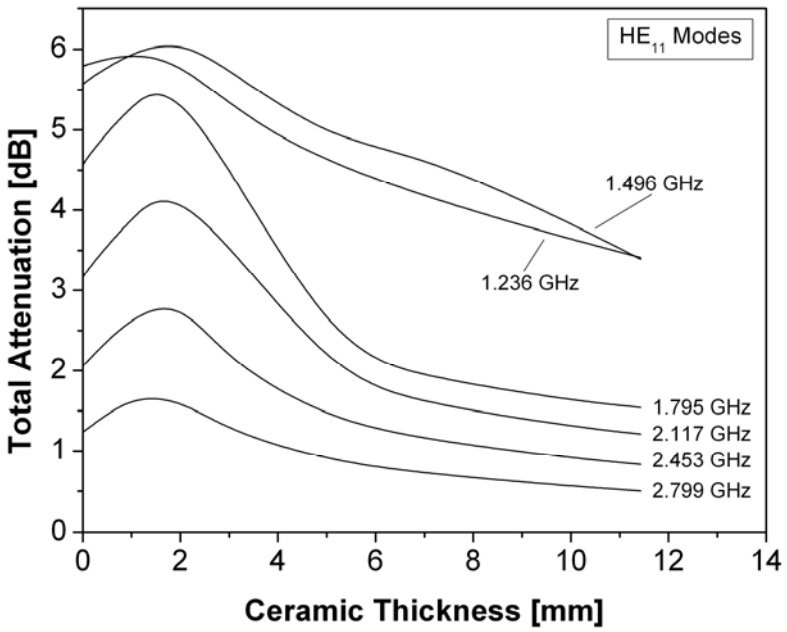

Figure 5.18: Total attenuation of HE_{11} modes in ceramic/ferrite damper for various frequencies.

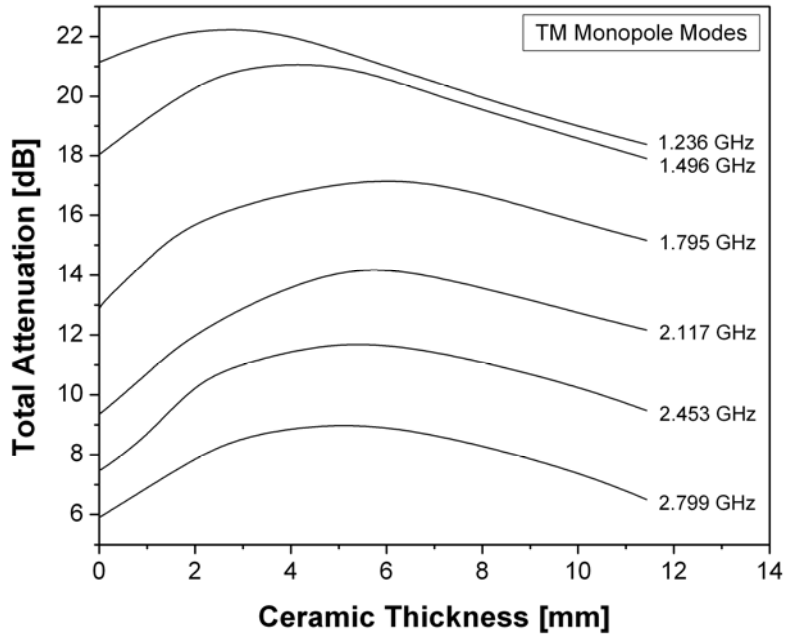

Figure 5.19: Total attenuation of TM_{01} modes in ceramic/ferrite damper for various frequencies.

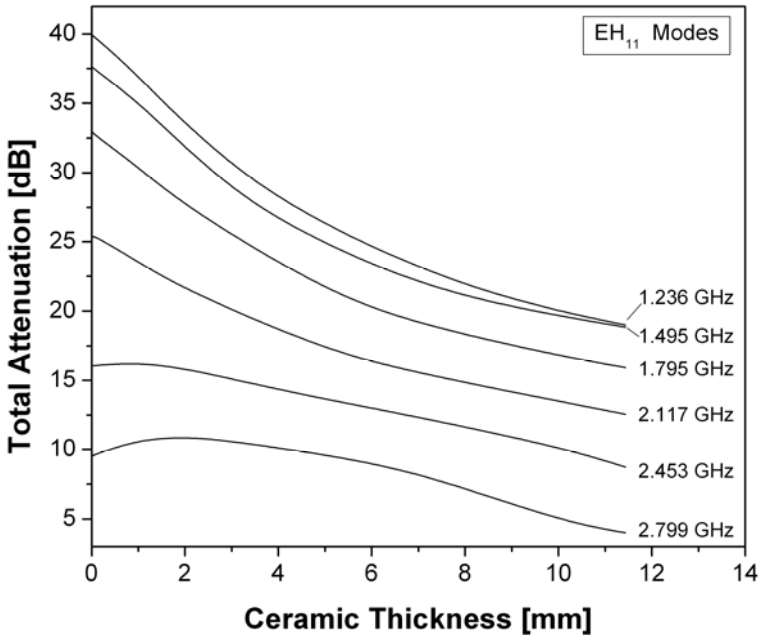

Figure 5.20: Total attenuation of EH_{11} modes of ceramic/ferrite damper for various frequencies.

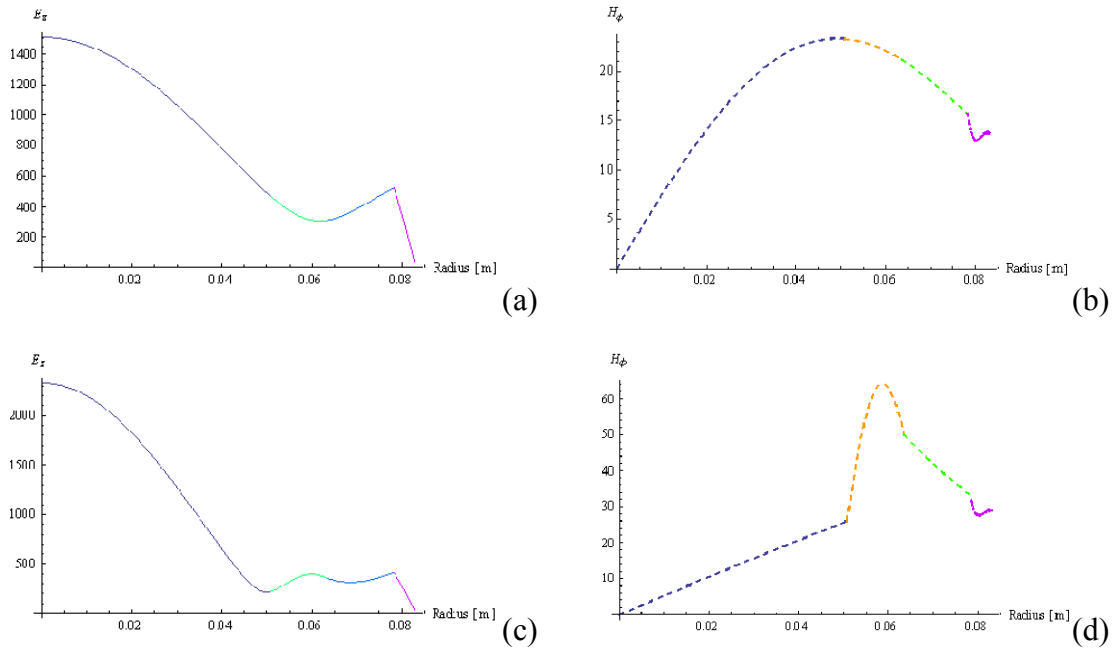

Figure 5.21: Comparison of electric and magnetic fields for ferrite damper with and without ceramic layer. In (a) and (b) the electric and magnetic fields are shown for 2.4 GHz respectively. In (c) and (d) electric and magnetic fields are shown the ceramic layer present. All examples include the outer ferrite ring. Different colors denote different layers: air core, (ceramic), air gap, ferrite.

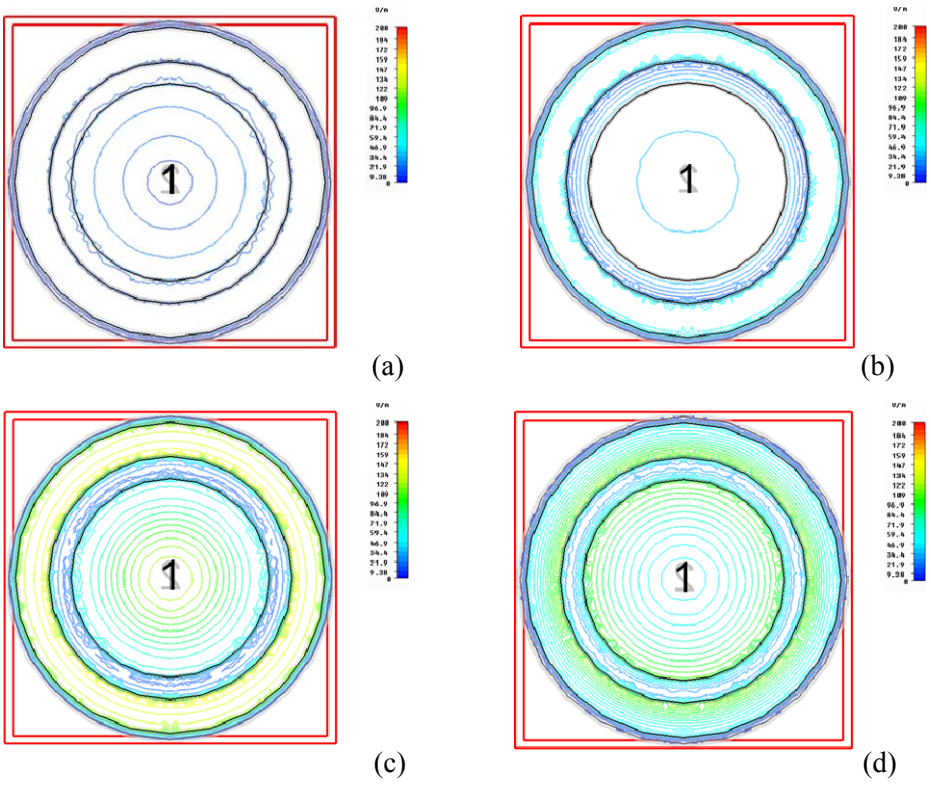

Figure 5.22: Field line plots from simulations of the EH mode of damper model using Microwave Studio at various frequencies: (a) 1.4 GHz, (b) 1.8 GHz, (c) 2.4 GHz, (d) 2.8 GHz. Cutoff for the cylindrical waveguide of same radius as outer radius of ferrite layer (0.08293 m) is 1.38 GHz.

5.6. Conclusions

The damper works because the ceramic is "translucent" to the field: the alumina allows the fields to penetrate the material and interact with the damping layer, but because of the high permittivity of the alumina, the field distribution is altered. Figure 5.21 shows how both electric and magnetic fields are altered. In general, the field density inside the alumina increases with increasing frequency, however enough of the field penetrates the alumina to interact with the ferrite and provide damping over a range of frequencies. As the frequency increases, more of the field penetrates through the alumina and interacts with the ferrite. This accounts for the peaked behavior of the attenuation for various mode types with increasing thickness: up to a certain point the ceramic alters the field sufficiently to cause maximum overlap between the magnetic field and the ferrite. It should also be kept in mind that the ferrite exhibits a high permittivity as well, causing further alteration of the field at the wall. However, as frequency increases, the imaginary part of the permeability of the ferrite decreases, accounting for the fall in attenuation

with increasing frequency overall. Also, as the calculations show, beyond a certain ceramic thickness, the ceramic tends to shield the ferrite from the magnetic field causing lower magnetic fields at the ferrite layer and lower attenuation. The distribution of the fields is illustrated graphically from simulation results for a simplified model in Figure 5.23.

It is also interesting to note the crossing of the 1.236 GHz and 1.496 GHz HE mode attenuation curves. The cause is unclear but may be explained by what appears to be the somewhat competitive effects of changing ceramic thickness and frequency-dependent permeability of the ferrite. As frequency increases, the imaginary permeability of the ferrite decreases, however, as all the data appears to confirm, increasing ceramic thickness, up to a point, increases the overlap of the magnetic field with the ferrite layer, depending on frequency, due to the distortion of the field profile. Increasing frequencies tends to concentrate the field in the areas with high-dielectric constant, namely the ceramic and the ferrite. However, as this concentration occurs, more field also interacts with the ferrite, leading to higher attenuation. A thickness of ~1 cm at low frequencies between 1.2 and 1.5 GHz represents the point at which the distortion of the field, in some sense, overcomes the falling imaginary permeability by distorting the field sufficiently to drive stronger interaction with the ferrite. Beyond 1.5 GHz, increasing ceramic thickness shows the same behavior for HE modes as for other mode types.

Thus, it would appear that the magnitude of the damping depends on several factors. Key among these are the space between the ceramic and ferrite layers, the thickness of the ceramic and ferrite layers, and the inner radius of the ceramic layer. In this series of calculations, the thickness of the ceramic layer was shown to be a key factor in determining the attenuation. The results indicate that ceramic thickness actually used in the damper is suboptimal since in most cases the calculated attenuation falls below the maximal value at each frequency for which measured ferrite permeability data is available. Nonetheless, a pronounced damping effect is still clearly evident at each frequency for the given ceramic thickness and this is confirmed by measurement as discussed above. It would be interesting to work toward optimizing the ceramic thickness for the majority of higher-order modes of interest. Another implication of the calculations is that a tapered length of ceramic might be very effective in broadband coverage of higher-order modes. These are all compelling avenues for further study.

Chapter 6

Summary

This thesis has examined higher-order mode damping in the Energy Recovery LINAC being constructed at Brookhaven National Laboratory. The energy recovery LINAC is a research and development machine meant to test the concepts and technologies that will be incorporated in other programs including coherent electron cooling and the electron-ion collider program called eRHIC. A central feature of the ERL is the use of a superconducting five-cell LINAC as well as a superconducting electron gun. Because of these structures, effective higher-order mode damping is a important feature of the project, and this document has described higher-order mode damper designs for the LINAC, and the electron gun and the key role that ceramic materials and novel approaches have played in the design of these dampers.

6.1. HOM Damping in the Five-Cell LINAC

For the five-cell LINAC, a ferrite, waveguide-type damper was discussed. The ferrite tiles line the beampipe adjacent to the cavity and the design is based on designs that were proven successful at other facilities including CESR and KEK-B. The ERL design was derived from Cornell and was proven to be a viable approach for high-power beams. It was shown that ferrite is an effective damper for the higher-order modes that may be expected from the five-cell cavity. Simulation work along with measurements of a prototype damper and cavity were essential to the efforts both to characterize the behavior of the ferrite and study its effectiveness, and these studies confirmed both the effectiveness of the ferrite as a damping material as well as the some-

what unusual design choice of a step-transition from the beampipe radius to the ferrite damper, made as a space-saving measure.

It is also interesting to note that the work confirmed the effectiveness of the modeling effort in studying the ferrite. Because the ferrite is a lossy material, it is challenging to model the broadband characteristics of the material using many commonly available simulation tools including the tool of choice for this study, Microwave Studio, due to the frequency-dependent nature of the permeability. However, the study was effectively able to derive a set of "portable" ferrite parameters that were able to simplify modeling efforts. It was found that the agreement between measurement and calculation is good over a range of frequencies and mode types, although small difference arose likely due to difference in geometry between the model and the actual measured prototype.

6.2. Damping of HOMs in the Electron Gun Using the Fundamental Power Couplers

Several methods of damping HOMs in the electron gun were studied including the use of the fundamental power couplers. The gun is powered by a dual-coupler design whose coupler tips are curved structures conformal with the beampipe radius and which were also designed at Cornell for the ERL injector. The dual-couplers and the curved tips are meant to maximize coupler power while minimizing wakefield effects with a design Q_{ext} of $4 - 5 \times 10^4$. It was found that the FPCs are strongly coupled to HOMs. However, the damping effect diminishes with frequency and, for the highest frequencies studied, no damping effect due to the FPCs was observed in simulation. It was also found that few if any of the HOMs studies are likely to be excited by the beam since their frequencies do not coincide with the beam harmonics based on the high-current operating parameters assumed at the outset of the study.

Measurements of the damping using "mock" FPCs were also conducted, and these studies also confirmed that the coupling to HOMs is strong although the damping effect was found to be smaller likely due to differences between the simulation and the actual prototype. These studies also appear to show that the coupling of the FPCs at low-frequency is somewhat smaller than at high-frequency. The nature of the termination in the measurements is crucial, and some difficul-

ties in matching were encountered. Nonetheless, the results suggest that there is significant damping of monopole and dipole modes particularly between 1 and 2 GHz, in agreement with simulation results.

An important limit to the effectiveness of the FPCs as dampers is the transition between the coaxial FPCs and the waveguides that feed power to the couplers. The transition is a "doorknob"-type design that shows rather poor transmission below 1 GHz although transmission increases sharply above 1 GHz. However, transmission falls off again rapidly around 2 GHz. Thus, the window of HOMs that could be effectively damped is rather small although it remains to simulate or measure the FPC and the doorknob transition together.

6.3. Design of the Ferrite HOM Load with a Ceramic Insert

A second method that was investigated for damping HOMs in the electron gun was the use of a ferrite load surrounding a ceramic break. The design is novel in its approach and was motivated initially to address potential concerns about the hazards that chipped or otherwise damaged ferrite tiles might pose to the gun cavity. Given the proximity of the ferrite to the gun and the various reports of damage to ferrite tiles from other institutions, it was decided that a design which seeks to minimize the exposure of the vacuum chamber to the ferrite tiles would be desirable. Hence, a structure was conceived in which ferrite tiles are used in a manner similar to that of the five-cell cavity but now, placed outside a ceramic break, thereby maintaining the ferrite outside of the vacuum.

Various simulation studies and measurements were conducted, including studies with various "break" materials including PVC, glass, and alumina, i.e., materials with varying permittivities. These studies and simulations indicate that the damper is effective because the ceramic allows penetration of the fields from the HOMs allowing the HOMs to dissipate energy in the ferrite material. The ceramic alters the fields of the HOMs in a frequency-dependent manner and thereby can enhance the effectiveness of the ferrite for certain frequencies by increasing the overlap between the ferrite layer and the magnetic field over the situation with just the ferrite alone. As

frequency increases, the effect tends to fall off and, beyond a certain frequency, the ceramic tends to shield the ferrite from the magnetic field, causing lower attenuation of the HOMs.

Thus, it was found that damping depends on several factors including the space between the ceramic and ferrite layers, the thickness of the layers, and the inner radius of the ceramic layer. The simplicity of the design makes it an interesting option of damping HOMs, and there remains a variety of interesting studies to perform to optimize the effectiveness of the arrangements for a given set of requirements.

Bibliography

[1] V. Ptitsyn *et al*., in *EPAC 2004 Conference Proceedings,* Lucerne, Switzerland, 2004.

[2] V. N. Litvinenko, and Y. S. Derbenev, Physical Review Letters **102** (2009).

[3] RHIC II Science Working Groups, *Future Science at the Relativistic Heavy Ion Collider - Summary of the 2004 - 2005 RHIC II Science Working Groups*, Brookhaven National Laboratory, Upton, 2006.

[4] RHIC Design Manual, Brookhaven National Laboratory, Upton, NY, 2000.

[5] K. Nakamura *et al*. (Joint Particle Group), J. Phys. G **37** (2009).

[6] V. N. Litvinenko *et al.*, *2007 IEEE Particle Accelerator Conference Proceedings*, Albuquerque, New Mexico (2007).

[7] R. Calaga *et al.*, Physica C - Superconductivity and Its Applications **441** (2006).

[8] M. Tigner, Nuovo Cimento **37** (1965).

[9] L. Merminga, D. Douglas, and G. Krafft, Annual Review of Nuclear and Particle Science 2003 **53** (2003).

[10] I. Ben-Zvi *et al.*, in *ERL 2005 Conference Proceedings,* Newport News, VA, 2005.

[11] H. Padamsee, J. Knobloch, and T. Hays, *RF Superconductivity for Accelerators* (Wiley-VCH Verlag GmbH & Co. KGaA, Weinheim, 2009), 2nd edn.

[12] R. Calaga, Ph.D. thesis, State University of New York at Stony Brook, Stony Brook, 2006.

[13] J. D. Jackson, *Classical Electrodynamics* (John Wiley & Sons, Inc., 1999).

[14] R. Harrington, *Time-Harmonic Electromagnetic Fields* (Wiley-IEEE Press, New York, 2001).

[15] Computer Simulation Technology AG, Boston, MA.

[16] P. J. B. Clarricoats, *Microwave Ferrites*, (John Wiley and Sons Inc., New York, 1961).

[17] Advanced Energy Systems, Medford, NY.

[18] ACCEL Instruments, GmbH, 51429 Bergisch-Gladbach, Germany.

[19] H. Hahn, E. M. Choi, and L. Hammons, Physical Review Special Topics-Accelerators and Beams **12** (2009).

[20] T. Tajima *et al.*, Proceedings of the 1999 Particle Accelerator Conference (Cat. No.99CH36366) (1999).

[21] D. Moffat *et al.*, *Conference Record of the 1991 IEEE Particle Accelerator Conference* (1991).

[22] D. Moffat *et al.*, *Proceedings of the 1993 Particle Accelerator Conference* (1993).

[23] W. Hartung, Ph.D. thesis, Cornell University, 1996.

[24] J. Mouris, and R. Hutcheon, *Measurements of the Complex Microwave Permeability of Un-biased Ferrite C-48 and Ferrite-50, from Room Temperature to 200-degrees C at Frequencies Between 915 MHz and 2800 MHz* (Microwave Properties North, Deep River, Ontario, Canada, 2000).

[25] H. Hahn *et al.*, Physical Review Special Topics - Accelerators and Beams **13** (2010).

[26] V. Shemelin, Belomestnykh, S., Padamsee, H., in *Cornell LEPP Report SRF* (Cornell University, Ithaca NY, 2002).

[27] R. Schuhmann, and T. Weiland, Physical Review Special Topics - Accelerators and Beams **3** (2000).

[28] Wolfram Research, Champaign, IL.